SUPERHYROPHOBICITY AND STRUCTURES OF ADSORBED SILANE COUPLING AGENTS ON SILICA AND DIATOMACEOUS EARTH

By

M. A. HELANKA JAYANI PERERA

Bachelor of Science in Chemistry
University of Kelaniya
Kelaniya, Sri Lanka
2005

Submitted to the Faculty of the
Graduate College of the
Oklahoma State University
in partial fulfillment of
the requirements for
the Degree of
DOCTOR OF PHILOSOPHY
July, 2016

SUPERHYROPHOBICITY AND STRUCTURES OF ADSORBED SILANE COUPLING AGENTS ON SILICA AND DIATOMACEOUS EARTH

Dissertation Approved:

Dr. Frank D. Blum

Dissertation Adviser

Dr. K. Darrell Berlin

Dr. Yolanda Vasquez

Dr. Sadagopan Krishnan

Dr. James E. Smay

ACKNOWLEDGEMENTS

I would like to express the deepest appreciation to my advisor Dr. Frank D. Blum for his support, motivation, cooperation, and for all of the opportunities I was given to conduct my research. Without his guidance and persistent help, this dissertation would not have been possible. Besides my advisor, I would also like to thank my advisory committee members, Dr. K. Darrell Berlin, Dr. Sadagopan Krishnan, Dr. Yolanda Vasquez, and Dr. James E. Smay.

I would like to thank my fellow lab mates, Dr. Bal Khatiwada, Dr. Charmaine Munro, Dr. Tan Zhang, Dr. Madhubhashini Madduma Arachchilage, Dr. Hamid Mortazavian, Bhishma Sedai, and Ugo Arua for all the fun we have had and for their support and valuable suggestions in the last five years.

I also would like to thank all the faculty and staff members of the Department of Chemistry, Oklahoma State University, for being very helpful and friendly. I am thankful to the Dry Surface Coating Guthrie, OK, for the financial support.

Last but not least, I would like to thank my husband, Saminda Perera. I could never have accomplished this dissertation without his support and understanding. My special thanks goes to my parents Neela Perera and Basil Perera, and my mother-in-law Anoma Wijesekera. Without their help it would have been impossible to accomplish this journey. I also wish to thank my sons Thamidu Perera and Evin Perera for giving me countless happiness and endless joy, which gave courage throughout this work.

Name: M. A. HELANKA JAYANI PERERA

Date of Degree: JULY, 2016

Title of Study: SUPERHYROPHOBICITY AND STRUCTURES OF ADSORBED SILANE COUPLING AGENTS ON SILICA AND DIATOMACEOUS EARTH

Major Field: CHEMISTRY

Abstract:

Superhydrophobic coatings were prepared using fluorosilane treated diatomaceous earth (DE) with either polyurethane or epoxy binders and the results were compared. The water contact angles were studied as a function of the amount of fluorosilane on DE and the amount of treated DE particle loadings in the coatings. The contact angles exceeded 150° for coatings with at least 0.02 mass fraction of fluorosilane on the DE and with 0.2 mass fraction particle loadings of fluorosilane-treated DE particles. The water contact angles of the surfaces were dependent on the nature of the binder below 0.2 mass fractions loading of the treated DE particles, while they were independent of the type of the binder after attaining superhydrophobicity.

The wettability of treated DE was studied as a function of the chain lengths and adsorbed amounts of alkyltrimethoxysilanes (C3, C8, C12, C16, and C18) with the help of water contact angle measurements. Temperature modulated differential scanning calorimetry (TMDSC) results showed that silanes on the treated DE became crystalline with increasing chain length ($C \geq 12$) and adsorbed hydrocarbon amounts (adsorbed amount ≥ 2.2 mg/m^2). The formation of a crystalline/ordered structure from low-surface energy material led to the formation of superhydrophobic coatings on treated DE. At similar adsorbed hydrocarbon amounts, as the carbon chain length of coupling agents increased, we observed a concomitant increase in the water contact angle.

The structural assemblies of hexadecyltrimethoxysilane (HDTMS) on silica/DE particles were studied by TMDSC, thermogravimetric analysis, and Fourier transform infrared spectroscopy (FTIR). HDTMS molecules adsorbed at very small adsorbed amounts molecules were directly bound to the silica/DE surface as isolated molecules, and their aggregates were more likely to be amorphous. These molecules were found to have very small enthalpies for both melting and crystallization of HDTMS hydrocarbon chains. These enthalpies were found to increase linearly with adsorbed amounts for the silica surface. With further increased adsorbed amounts of HDTMS, melting and crystallization enthalpies increased exponentially and approached the bulk HDTMS enthalpy for samples with a distance constant of around 1.6 and 2.9 mg/m^2 for silica and DE, respectively.

TABLE OF CONTENTS

ChapterPage

ChapterPage

LIST OF TABLES

TablePage

LIST OF FIGURES

FigurePage

FigurePage

CHAPTER I

INTRODUCTION

Hydrophobicity is an important property for various kinds of solid surfaces for many applications. Contact angles for water droplets on surfaces can be used to estimate hydrophobicity. Hydrophobicity means fear (phobic) of water (hydro). Surfaces with water contact angles greater than 90° are considered hydrophobic, and surfaces with very high water contact angles (particularly larger than 150°) and sliding angle typically less than 5-10° are usually considered superhydrophobic.[1] Many superhydrophobic surfaces are found in nature such as lotus leaves, butterfly wings, rose petals and gecko feet. These surfaces have special interesting properties such as anti-stick, anti-contamination,[2,3] and self-cleaning abilities.[4-8] These properties have made studies of superhydrophobic materials interesting for the research and development field in last decade. A combination of suitable surface roughness and low-surface-energy is responsible for superhydrophobicity. Many of the preparation techniques to achieve superhydrophobicity are difficult, expensive, or need special equipment. With the development of superhydrophobic coatings, different kinds of methods have been used as preparations, such as phase separation,[9] electrochemical deposition,[10] template methods,[11,12] emulsion,[13] plasma,[14] crystallization control,[15] chemical vapor deposition,[16] wet chemical reaction,[17] electrospinning,[18] solution immersion,[19] sol-gel processing,[20,21] and others.[22,23] Even though these surfaces show very high contact angles, the use of expensive materials and complex processes limits their use on lager surface area applications. Recently diatomaceous earth (DE) based superhydrophobic coatings with fluorosilane molecules were shown to be superhydrophobic.[24-26] DE has high thermal stability,[27] high porosity,[28,29] relatively low cost[30,31] and can be useful for creating superhydrophobic coatings.

Diatoms are groups of unicellular photosynthetic eukaryotes terrestrial in most aquatic habitats.[32] They are responsible for 20-25% of the world's net primary food production [32] and play an important role in the global biogeochemical silica cycling.[33] There are more than 200,000 estimated diatom species by their unique frustule shapes.[32] These unique frustules are composed of amorphous silica, with relatively small percentages of other oxides such as Al_2O_3, Fe_2O_3, CaO, and others.[34] These frustules are decorated with unique patterns such as pores, channels, rides, spikes, and spines.[31] Most frustules are composed of two halves. The inner frustule is known as the hypotheca, and the outer one is called the epitheca.[32]

Diatoms are classified in to two major groups based on the valve symmetry. Two groups are, in the class of centrics, diatom frustules that have radial symmetry with the pores extending radially from the center to the circumference (Figure 1.1a). The pennate diatoms frustules are elongated and have bilateral symmetry. They contain parallel pore rows perpendicular to the long axis (Figure 1.1b).[35]

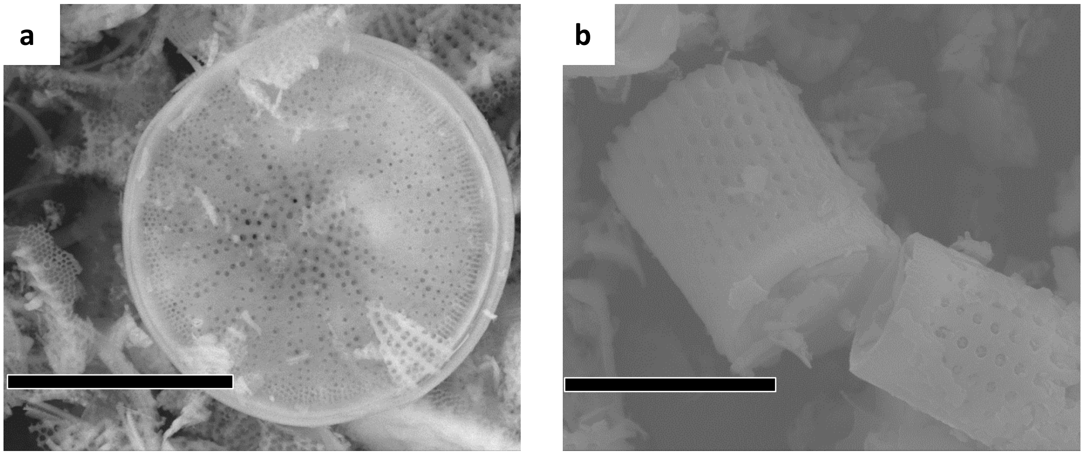

Figure 1.1. Scanning electron micrograph (SEM) of (a) centric (b) pennate diatoms.

In Chapter III, the research reported was focused on understanding some of the basic principles of coatings relevant to production of superhydrophobic coatings with fluorosilane treated DE. Of particular interest was the understanding of the dependence of superhydrophobicity on different mass fractions of fluorosilane, different amounts of fluorosilane-treated DE particle loadings, and with different polymer binders (epoxy and polyurethane). The amounts of fluorosilane coupling agents on the surface and surface area/pore size distributions of treated DE particles were determined from thermogravimetric analysis (TGA) and Brunauer–Emmett–Teller (BET). The surface morphology of treated DE particle coatings were observed using scanning electron microscopy (SEM). Contact angle measurements have been used for understanding the wettability of the surface.

The second study, Chapter IV; deals with the modification of DE with non-fluorosilane coupling agents and understanding the development of superhydrophobicity with silane treatment of different chain lengths. The modification of DE was performed using alkyltrimethoxysilanes of chain lengths (C3, C8, C12, C16, and C18) at similarly adsorbed hydrocarbon amounts. The wettability of functionalized DE containing surfaces was studied using water contact angle measurements. The water contact angles were also studied as a function of the amount of treated DE particle loadings in polyurethane coatings. We also investigated the thermal properties of these alkyltrimethoxysilane-treated DE powders using TGA and differential scanning calorimetry (DSC). The surface properties and porosity of these systems were able studied with Brunauer–Emmett–Teller (BET) specific surface area and pore volume measurements.

In addition to superhydrophobicity, we were interested in understanding the structural associations of organosilanes on different silica surfaces as discussed in Chapters V and VI. In these studies, hexadecyltrimethoxysilane was used as an organosilane coupling agent to treat the different types of silica surfaces. DE and nano silica particles (Cab-O-Sil LM130) were used as solid surfaces to study the behavior of treated organosilane under different grafted densities. These samples were characterized by temperature–modulated differential scanning calorimetry (TMDSC), TGA, and Fourier transform infrared spectroscopy (FTIR). TMDSC has been used to study the melting and crystallization enthalpies and temperatures of bulk and treated surfaces.[36] Thermal transition temperatures and enthalpies of bulk hexadecyltrimethoxysilane has been compared with those of the treated DE and nano silica. Moreover, changes in the enthalpies of melting and crystallization for treated hexadecyltrimethoxysilane samples indicates that the hexadecyltrimethoxysilane molecules underwent significant structural changes, from surface to bulk like-structures with the addition of more coupling agents. The enthalpies of melting and crystallization over a wide range of compositions were measured using TMDSC. These enthalpy values were fitted with a multilayer model, with the contribution of a surface attached “monolayer like” surface, where enthalpy increased linearly with adsorbed amount and multilayers whose enthalpy increased exponentially from the monolayer to near the bulk value of hexadecyltrimethoxysilane.

The last part of this thesis deals with the effect of p-toluenesulfonic acid (PTSA) on the adsorption of silane coupling agents. Silica and DE surfaces were able to be modified with silane coupling agents using of PTSA as a catalyst. Due to the presence of hydrophilic silanol groups on the surface of silica and DE, sulfonate groups of PTSA interacted with the surfaces. These interactions/adsorption led to difficulty in calculating the amount of adsorbed silane coupling agent. In the Chapter VII it was determined how to calculate the amount of adsorbed coupling agent and the PTSA on the surface.

1.1. REFERENCES

(1) Ma, M.; Hill, R. M.; Rutledge, G. C. *J. Adhes. Sci. Technol.* **2008**, *22*, 1799.

(2) Barthlott, W.; Neinhuis, C. *Planta* **1997**, *202*, 1.

(3) Lafuma, A.; Quere, D. *Nat. Mater.* **2003**, *2*, 457.

(4) Otten, A.; Herminghaus, S. *Langmuir* **2004**, *20*, 2405.

(5) Nakajima, A.; Hashimoto, K.; Watanabe, T.; Takai, K.; Yamauchi, G.; Fujishima, A. *Langmuir* **2000**, *16*, 7044.

(6) Miwa, M.; Nakajima, A.; Fujishima, A.; Hashimoto, K.; Watanabe, T. *Langmuir* **2000**, *16*, 5754.

(7) Fürstner, R.; Barthlott, W.; Neinhuis, C.; Walzel, P. *Langmuir* **2005**, *21*, 956.

(8) Blossey, R. *Nat. Mater.* **2003**, *2*, 301.

(9) Han, J. T.; Xu; Cho, K. *Langmuir* **2005**, *21*, 6662.

(10) Shirtcliffe, N. J.; McHale, G.; Newton, M. I.; Chabrol, G.; Perry, C. C. *Adv. Mater.* **2004**, *16*, 1929.

(11) Hwang, H. S.; Lee, S. B.; Park, I. *Mater. Lett.* **2010**, *64*, 2159.

(12) Huang, Y.-H.; Wu, J.-T.; Yang, S.-Y. *Microelectron. Eng.* **2011**, *88*, 849.

(13) Yang, T.; Tian, H.; Chen, Y. *J Sol-Gel Sci Technol* **2009**, *49*, 243.

(14) Kinoshita, H.; Ogasahara, A.; Fukuda, Y.; Ohmae, N. *Carbon* **2010**, *48*, 4403.

(15) Guo, Z.-G.; Fang, J.; Hao, J.-c.; Liang, Y.-m.; Liu, W.-m. *ChemPhysChem* **2006**, *7*, 1674.

(16) Lau, K. K. S.; Bico, J.; Teo, K. B. K.; Chhowalla, M.; Amaratunga, G. A. J.; Milne, W. I.; McKinley, G. H.; Gleason, K. K. *Nano Lett.* **2003**, *3*, 1701.

(17) Mumm, F.; van Helvoort, A. T. J.; Sikorski, P. *ACS Nano* **2009**, *3*, 2647.

(18) Ma, M.; Mao, Y.; Gupta, M.; Gleason, K. K.; Rutledge, G. C. *Macromolecules* **2005**, *38*, 9742.

(19) Zhang, X.; Guo, Y.; Zhang, P.; Wu, Z.; Zhang, Z. *Mater. Lett.* **2010**, *64*, 1200.

(20) Ganbavle, V. V.; Bangi, U. K. H.; Latthe, S. S.; Mahadik, S. A.; Rao, A. V. *Surf. Coat. Technol.* **2011**, *205*, 5338.

(21) Latthe, S. S.; Hirashima, H.; Rao, A. V. *Smart materials and structures* **2009**, *18,* 095017.

(22) Liu, H.; Feng, L.; Zhai, J.; Jiang, L.; Zhu, D. *Langmuir* **2004**, *20*, 5659.

(23) Zhu, L.; Xiu, Y.; Xu, J.; Tamirisa, P. A.; Hess, D. W.; Wong, C.-P. *Langmuir* **2005**, *21*, 11208.

(24) Oliveira, N. M.; Reis, R. L.; Mano, J. F. *ACS Appl. Mater. Interfaces* **2013**, *5*, 4202.

(25) Polizos, G.; Winter, K.; Lance, M. J.; Meyer, H. M.; Armstrong, B. L.; Schaeffer, D. A.; Simpson, J. T.; Hunter, S. R.; Datskos, P. G. *Appl. Surf. Sci.* **2014**, *292*, 563.

(26) Sedai, B. R.; Khatiwada, B. K.; Mortazavian, H.; Blum, F. D. *Appl. Surf. Sci.* **2016**, *386*, 178.

(27) Ivanov, S. É.; Belyakov, A. V. *Glass Ceram* **2008**, *65*, 48.

(28) Polizos, G.; Winter, K.; Lance, M. J.; Meyer, H. M.; Armstrong, B. L.; Schaeffer, D. A.; Simpson, J. T.; Hunter, S. R.; Datskos, P. G. *Appl. Surf. Sci.* **2014**, *292*, 563.

(29) Bariana, M.; Aw, M. S.; Kurkuri, M.; Losic, D. *Int. J. Pharm.* **2013**, *443*, 230.

(30) Lettieri, S.; Setaro, A.; De Stefano, L.; De Stefano, M.; Maddalena, P. *Adv. Funct. Mater.* **2008**, *18*, 1257.

(31) Losic, D.; Mitchell, J. G.; Lal, R.; Voelcker, N. H. *Adv. Funct. Mater.* **2007**, *17*, 2439.

(32) Gordon, R.; Losic, D.; Tiffany, M. A.; Nagy, S. S.; Sterrenburg, F. A. S. *Trends Biotechnol.* **2009**, *27*, 116.

(33) Lopez, P. J.; Descles, J.; Allen, A. E.; Bowler, C. *Curr. Opin. Biotechnol.* **2005**, *16*, 180.

(34) Jing, Y.; Jing, Z.; Ishida, E. H. *Ind. Eng. Chem. Res.* **2013**, *52*, 17865.

(35) Scala, S.; Bowler, C. *CMLS, Cell. Mol. Life Sci.* **2001**, *58*, 1666.

(36) Zhang, T.; Xu, G.; Puckette, J.; Blum, F. D. J. Phys. Chem. C 2012, 116, 11626.

CHAPTER II

BACKGROUND

2.1. DIATOMACEOUS EARTH

Diatomaceous earth is the fossilized remains of unicellular, eukaryotic, photosynthetic aquatic organisms called diatoms.[1,2]

2.1.1. Structure and properties of diatomaceous earth

Diatomaceous earth (DE) is a naturally occurring soft mineral compound. It is mostly composed of pure amorphous silicon dioxide (SiO_2. nH_2O), made up of skeletons (frustules) of diatoms which are unicellular microscopic plants and probably the most widespread group of plants on the earth which participate in photosynthetic production.[2] They are abundant in all aquatic ecosystems and also terrestrial environments. Diatoms have distinct frustules (more than twenty five thousand species of diatoms with unique morphology) with micro-nano pore structure and species characterized pore patterns. (Figure 2.1)

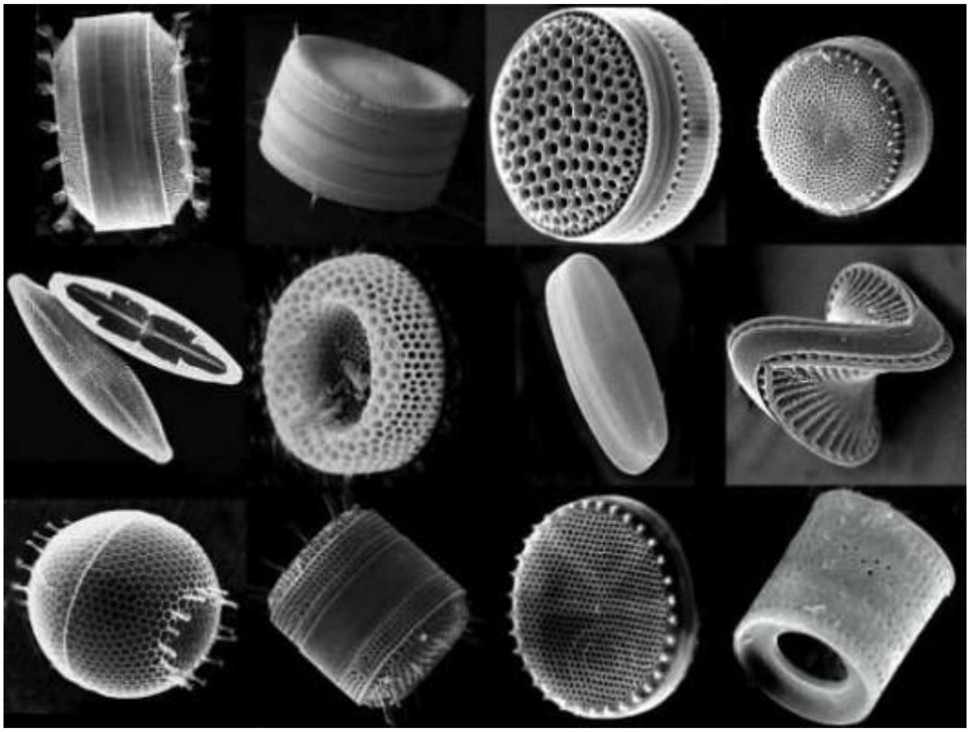

Figure 2.1. Different shapes of diatoms. (Photo from : potiphar.jongarvey.co.uk)

About 20 to 80 million years ago, mostly in the Eocene and Miocene epochs, different species of diatoms extracted silicon from water because of the compressive strength of wall silica and its possible immunity to enzymatic attach.[3] When the diatoms died, the tiny shells sunk, and over the years these shells pressed and formed thick layers. Eventually these deposits were fossilized and compressed into a soft, chalky rock that is now called DE. Deposits of diatoms occur in hundreds of localities. Many of these deposits are extensive and rather free from excessive contamination by impurities. Deposits range in thickness from a few centimeters to several hundred meters. DE contains 75–96% silica, with 1-10% alumina, less than 3% iron oxide, and other oxides.[3-8]

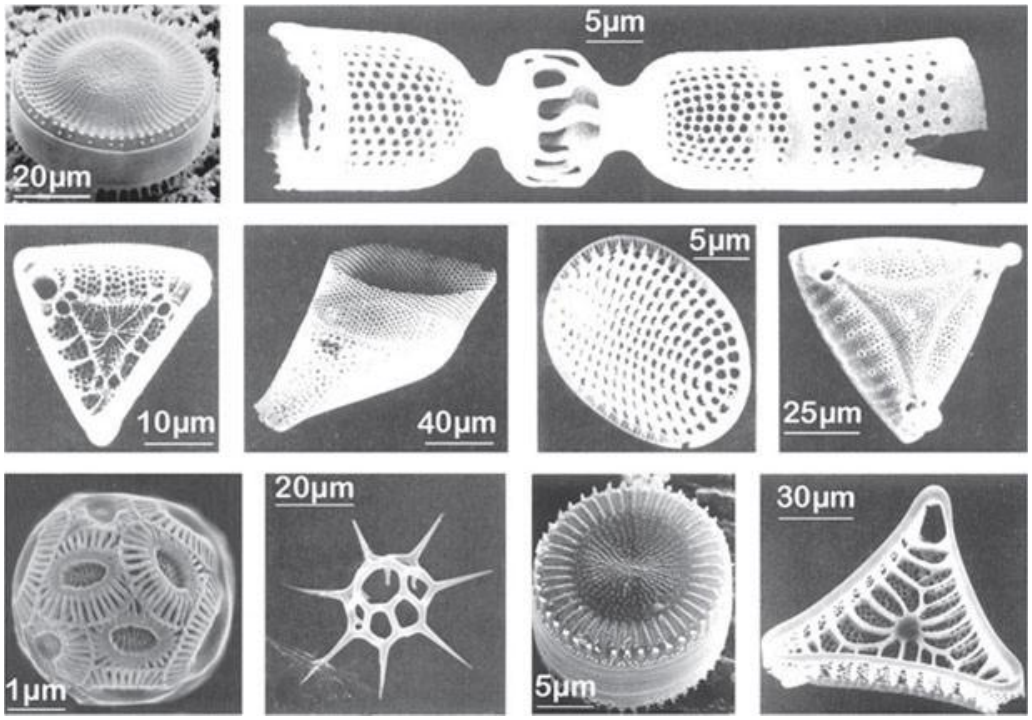

Figure 2.2. Electron microscopy of a selection of ten planktonic diatoms, measuring between 1–40 µm. (Photo from: www.swimuniversity.com)

DE, in its natural state, is composed largely of amorphous silica and there is no evidence that this form of silica is particularly toxic to humans.[9] Crystalline silica can pose a health hazard due to entering in to respiratory system. While the amount of crystalline silica in natural DE is quite small (less than 1%) to pose a health hazard, DE is extremely stable and does not produce toxic chemical residues or react with other substances in the environment. So according to the Environmental Protection Agency (EPA) in the USA, natural DE is described as amorphous silicon dioxide which is classified and generally recognized as a safe (GRAS) food additive.[9]

DE is commonly used for the purification of water, the removal of microorganisms from juice, the filtration of commercial fluids, and the separation of various oils and chemicals due to its high porosity (Figure 2.2 and 2.3).[10] DE can absorb two to three times its own weight in liquids without flowing; this property was used in the preparation of pesticide carriers, and for the safe storage and transportation of hazardous liquids.[3] It is also used in a large number of commercial products such as detergents, deodorizers, filter systems for swimming pools, a drilling–mud additives, anti–caking agents, and animal feed additives.[10]

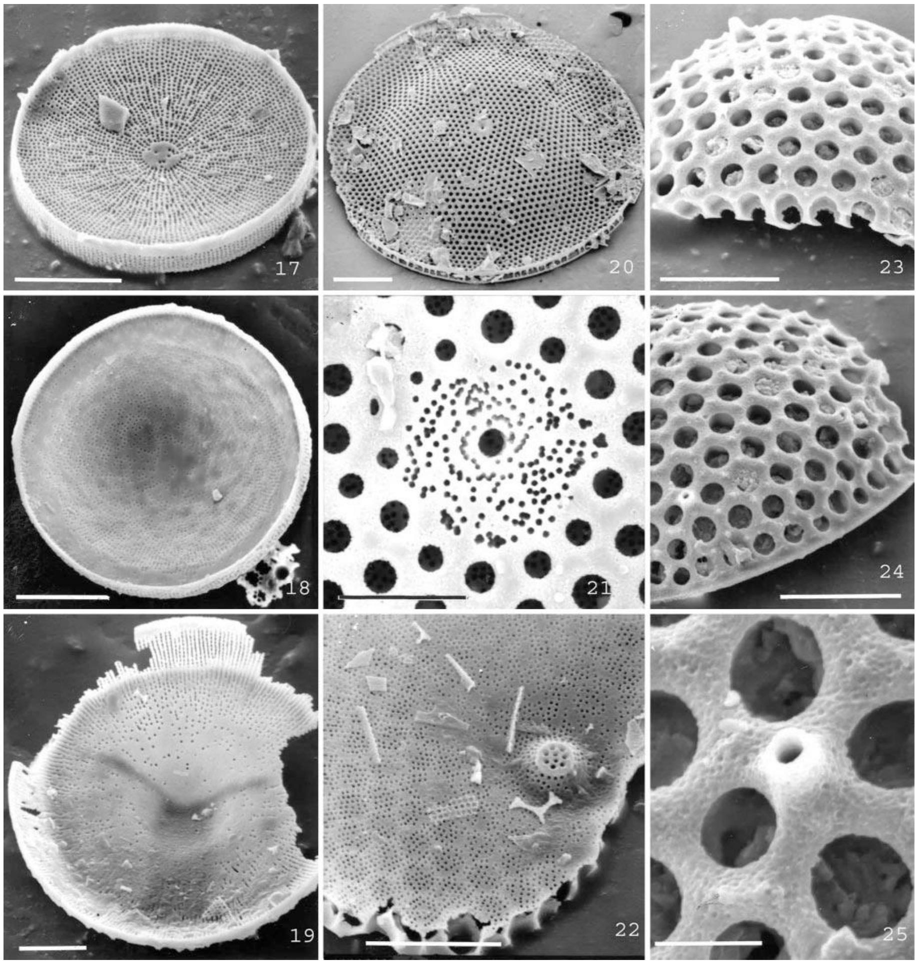

Figure 2.3. Highly developed micro-nano structure of diatomaceous earth is extracted from the Evolution of the diatoms: insights from fossil, biological and molecular data by Patricia A. Sims and co-authors.[10]

DE skeletons have unique nanostructure patterns which include pores, rides, and areoles. These features make up the micro- and nano- structure of DE, which is a very important source for nanotechnology (Figure 2.3).[10] Due to its specific properties such as high porosity, high silica content, low density, low conductivity coefficient, and low price, it can be used in the formation of superhydrophobic coatings when modified with low surface energy material.

2.2. WETTING AND DEWETTING

Wettability of solid surfaces with a liquid (water in particular) is a crucial surface property, which plays an important role in daily life, as well as in many industrial processes. Wetting is the ability of a liquid to maintain contact with a solid surface, resulting from intermolecular when the two are brought together. The degree of spreading (wettability) depends on cohesive forces between liquid molecules and adhesive interactions between liquid and solid molecules. Adhesive interactions cause a liquid drop to spread across the solid surface, and cohesive interactions cause the liquid drop to ball up and avoid contact with the surface. Equilibrium between these two interactions causes the shape of the drop on the solid surface, which is defined by contact angle.

2.2.1. Surface tension

Surface tension of a liquid formed is due to the inter-molecular attractive forces (cohesive forces) present in-between the liquid molecules. As seen in Figure 2.4, at liquid air interface, surfaces do not have the same type of molecules on all the sides. Therefore, cohesive forces are imbalanced and try to pull inwards. Consequently, the water molecules make them acquire the least surface area as possible and form spherical droplets. The net effect is water behaving as a stretched elastic membrane. Liquids with a greater proportion of polar groups (e.g., O-H groups) give rise to the higher surface tension in air and form separate water droplets on the surface rather than wetting the evenly. Surface tension is usually represented by γ and quantified in terms of the, force acting on a unit length or energy per unit area.

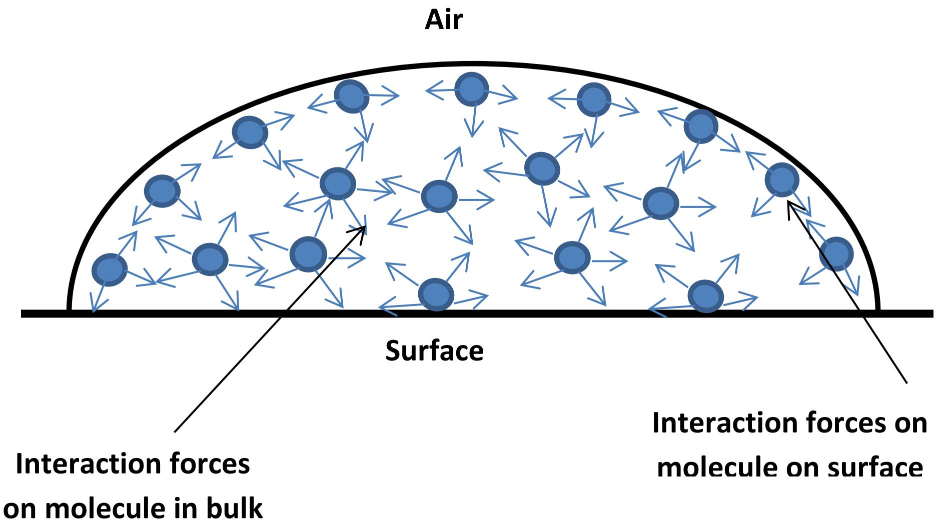

Figure 2.4. Cohesive forces inside a water drop.

2.2.2. Contact angle

The contact angle is measured through the liquid, where a liquid/vapor (gas) interface meets a solid surface. The interface where all three phases (solid, liquid, and vapor) co-exist is referred to as the “three-phase line.” Figure 2.5 shows a sketch of liquid droplet on solid surface forming a contact angle of θ. The contact angle depends on the forces acting on the liquid droplet. $\gamma_{sl,}$ $\gamma_{lv,}$ and γ_{sv} are the surface tensions of solid–liquid, liquid–gas and solid–gas interface, respectively, as Figure 2.5.

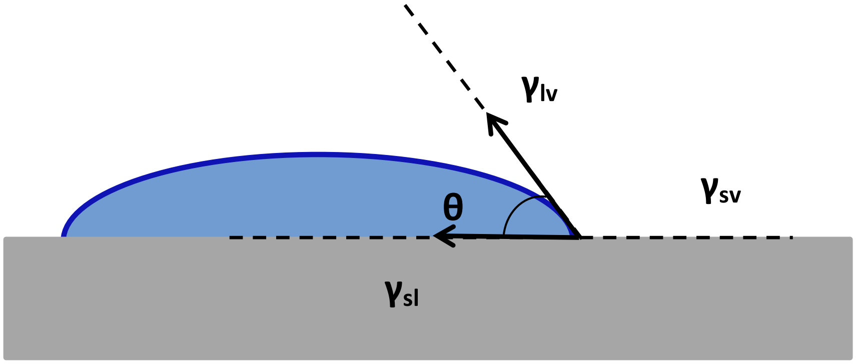

Figure 2.5. Contact angle of liquid on solid surface.

The contact angle or shape of the liquid droplet on the surface is determined by the combination of surface tension and external force (gravity). The water contact angle can be classified into three different regimes: less than 90° (hydrophilic), between 90° and 150° (hydrophobic), and equal or greater than 150° (superhydrophobic). Figure 2.6 graphically illustrates some possible contact angles formed by sessile drops on surfaces.

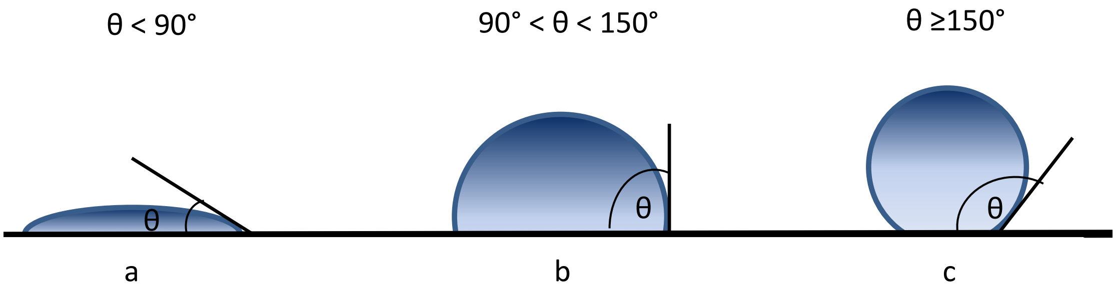

Figure 2.6. Schematic representation of contact angles for a water droplet placed on (a) hydrophilic (b) hydrophobic and (c) superhydrophobic surfaces.

2.3. SUPERHYDROPHOBICITY

Surfaces that exhibit contacts angles greater than 150° and small contact angle hysteresis are defined as superhydrophobic surfaces. Superhydrophobicity occurs due to a combination of two physical properties:

a) surface roughness

b) low surface energy

To form a superhydrophobic coating, a rough surface may be modified with the help of low surface energy material or surface roughness created on a low surface energy material. The need for a low surface energy rough topography on the formation of superhydrophobicity is detailed below.

2.3.1. Smooth surface

A liquid, placed on a homogeneous smooth solid surface with equilibrium contact angle θ, can, in principle, be obtained using Young's equation as in equation 2.1.

$$\cos\theta = \frac{\gamma_{sv}-\gamma_{sl}}{\gamma_{lv}} \tag{2.1}$$

For a given solid surface, liquids with larger surface tensions in a given medium would form a higher contact angles because they have low wettability compared to liquids with lower surface tensions. When the liquid is water, water repelling solids are classified as hydrophobic (> 90 ^{o}) and water loving solid are classified as hydrophilic (< 90 ^{o}). In the case where the liquid phase is water and vapor phase is air, the surface tension of water and air (γ_{lv}) is constant. Therefore, the contact angle can be increased by lowering the surface energy of the surface with air (γ_{sv}). As reported, material with CF_2 and CF_3- functional groups on a smooth surface have the lowest surface energy with water contact angles of about 120°,[11-13] which nearly highest contact angle recorded for fluorocarbon treated surfaces. Hence, superhydrophobicity cannot be achieved with a smooth surface, even when the surface is coated with lowest surface energy material.

2.3.2. Rough surface

If the liquid is on a rough surface, it can either penetrate into the rough surface (Wenzel regime) or suspend above the rough surface (Cassie-Baxter regime) as shown in Figure 2.7.

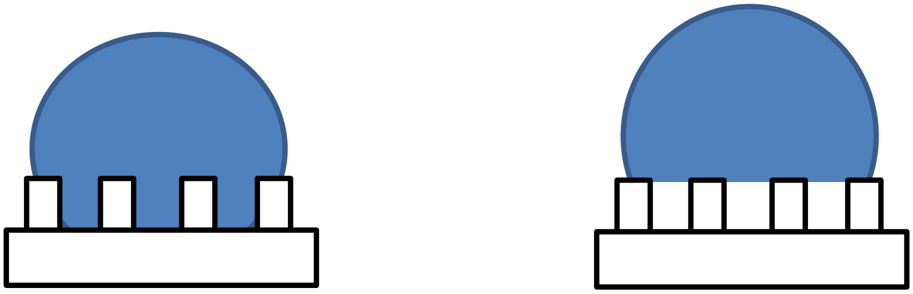

Figure 2.7. A liquid droplet sits on a rough surface. Left: Wenzel regime; right: Cassie-Baxter regime.

The contact angle of surfaces with Wenzel regime is given by Wenzel's equation as equation 2.2:

$$\cos\theta_{rough} = r\cos\theta_{smooth} \tag{2.2}$$

where θ_{rough} is the apparent contact angle on the rough surface, r is the surface roughness factor, or the ratio of the contact surface area divided by the projection area, and θ_{smooth} is the intrinsic contact angle on a smooth surface. In the Wenzel regime if a material has $\theta_{\text{smooth}} > 90^{\circ}$, the surface roughness could make it superhydrophobic; if a material has $\theta_{\text{smooth}} < 90^{\circ}$, roughness make it superhydrophilic.

In the Cassie-Baxter regime, the liquid is suspended on a rough surface and air trapped between the solid materials; in other words, a liquid droplet on a composite surface. In this regime Cassie-Baxter equation 2.3, gives contact angle:

$$\cos\theta_{rough} = \Phi s \cos\theta_{smooth} + \Phi_{V} \cos\theta_{lv} \qquad (2.3)$$

$$\cos\theta_{rough} = \Phi s \;\; 1 + \cos\theta_{smooth} \;\; - 1 \qquad (2.4)$$

In this equation, θ_{rough} is the contact angle on rough surface, Φs and Φv are the fractions of solid and air in contact with liquid (Φs + Φv = 1) and θ_{smooth} is the intrinsic contact angle on a smooth surface. Since, the contact angle of air (θ_{lv}) is 180°, $\cos \theta_{\mathrm{lv}} = -1$. Therefore, the Cassie-Baxter equation can be rewritten as equation 2.4. According to the Cassie-Baxter regime, a water droplet is sitting on top of the rough surface, so superhydrophobicity can be attained even with a slightly hydrophilic material with the proper surface roughness.

2.4. LOW SURFACE ENERGY MATERIALS USED ON SUPERHYDROPHOBICITY

Controlling the surface energy is very important for the formation of the hydrophobic and superhydrophobic coatings. Therefore, a variety of chemicals are used in the formation of superhydrophobic coatings to reduce the surface energy of the surface. Fluorine is a well-known effective low surface energy element because it has a small atomic radius and large electronegativity. As reported in the literature, the free energy of a surface decreases in this order: $-CH_2 > -CH_3 > -CF_2 > -CF_3$.[13] There are two groups of low surface energy materials of interest in this study; silane (fluorosilane and non-fluorosilane with a long hydrocarbon chain) and fluoropolymers. Fluorosilane and non-fluorosilane (with long hydrocarbon tail) are often used in the formation of superhydrophobic coatings. Octadecyltrichlorosilane (OTS),[14,15] hexadecyltrimethoxysilane (HDTMS),[16,17] dodecyltrimethoxysilane(DDTMS),[18,19] perfluorooctyltrichlorosilane (PFOS),[20,21] 3,3,3-trifloropropyltrichlorosilane (TFPS), and heptadecafluorodecyltrimethoxysilane (HFTMS)[22,23] are some of examples which are able to be applied on to the surface to introduce the low surface energy. Other low surface energy materials include fluoropolymers; such as C4F8[24], Teflon[25], poly(vinylidene fluoride)[26] and fluoro-copolymers.[27,28] More details about silane coupling agent structure, functions, and reactions with the surface are explained in 2.4.1 section.

2.4.1. Silane Coupling Agent

A silane coupling agent is a silicon based chemical, which possesses a hydrolytically sensitive center that can react with inorganic/organic substrates (e.g. silica, alumino-silicates, inorganic oxides, quarts, glass) to form stable covalent bonds and transfer an organic group. These hydrolytically sensitive centers change the physical interactions of the modified substrate or promote adhesion between dissimilar materials.

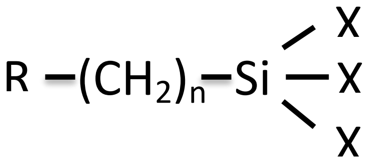

$R-(CH_2)_n-SiX_3$

Figure 2.8. General formula of silane coupling agent, R is the organic substitution which allows modification of the substrate, $(CH_2)_n$ is a linker and, X is hydrolysable groups (e.g. alkoxy, acyloxy, halogen, or amine).

The general formula for silane coupling agents is R’-Si-X_3, where X is hydrolysable groups typically halide- (e.g. Cl), methoxy- ($-OCH_3$), ethoxy- ($-OC_2H_5$) and amine- ($-NH_2$). With the hydrolysis, reactive silane groups condense with the surface hydroxyl groups to form siloxane bonds. The R’ group is a non-hydrolysable organic group, which changes the properties of the silane. In general, the reactivity of these groups decreases in order of Si-NR_2 > Si-Cl > Si-$OCCH_3$ > Si-OCH_3 > Si-OCH_2CH_3.

According to the type of substitution present on the silane coupling agent, there are a wide variety of applications possible for these materials, such as water-repellent coatings, anti-fog coatings, fillers for composites, nanoparticle, and self-assembled monolayers, etc. During some of the applications, silane coupling agents are used to introduce hydrophobicity/hydrophilicity to given surfaces. These silane-coupling agents are non-functionalized and can be classified into two main groups according to their surface energy:

- Low surface energy species (hydrophobic silane coupling agents)
  Methyl, linear long alkyl chain, branched alkyl, fluorinated alkyl silane coupling agents. E.g., trimethylchlorosilane, octadecyltrimethoxysilane, octyldimethylchlorosilane, heptadecafluorodecyltrimethoxysilane, 3-(heptafluoroisopropoxy)- propyltrimethoxysilane
- Higher surface energy species (Hydrophilic silane coupling agents)
  Polar, hydroxylic, and ionic containing silane-coupling agents. E.g., chloropropyltrimethoxysilane, hydroxymethyltriethoxysilane

2.4.1.1. Surface modification with silane coupling agents

Many silane-coupling agents have organic substituient groups and three hydrolysable groups. (Figure 2.8) During the surface treatment, hydrolysable groups hydrolyze to form silanol-containing species. These silanol groups react with the surfaces bearing hydroxyl groups. As a result, substitution reactions take place in between the surface and substrate to form a covalent attachment through an oxygen linkage. However, the presence of large adsorbed amounts of silane coupling agents in solution will lead to condensation between hydrolyzed silane-coupling agents, forming oligomers. Therefore, these oligomers covalently link to the substrate with the concomitant loss of water. During the adsorption process of the silane coupling agent, usually only one hydrolyzed group will react with the surface. The other two hydrolyzed groups are present in either condensed or free form. A schematic representation for the reactions of silane coupling agents with surfaces are shown in Figure 2.9.

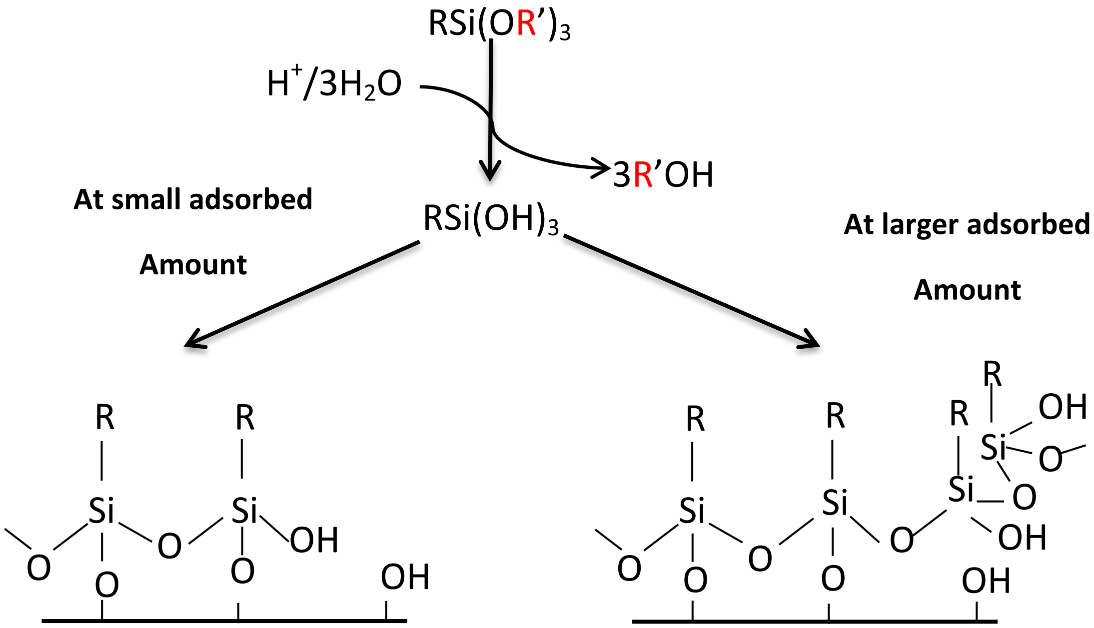

Figure 2.9. A schematic representation of silane coupling agents reactions with silica surface at different adsorbed amounts.

2.5. CHARACTERIZATION TECHNIQUES

This research involves the necessary characterization of structure and morphology of silanes with DE and the resulting surface wettability. The ability to characterize the coating morphology is very important in this research. The characterization techniques used in this research included contact angle measurement, scanning electron microscopy

(SEM), thermogravimetric analysis (TGA), Fourier transform infrared spectroscopy (FTIR), temperature-modulated differential scanning calorimetry (TMDSC), Brunauer, Emmett, and Teller (BET) and pore size analysis.

2.5.1. Contact angle

Contact angle measurement is one of the most common methods used to measure the hydrophobicity of a surface. The contact angle measurement instrument in our laboratory directly measures the tangent angle (contact angle) of the three-phase point using the sessile drop method. Many measuring techniques have been described in the literature such as captive bubble method, tilting plate method, Wilhelmy Balance Method, and Telescope-Goniometer.[29] Only few of these techniques have been found to be generally applicable. The most frequently used method is the sessile drop method using a Telescope-Goniometer.

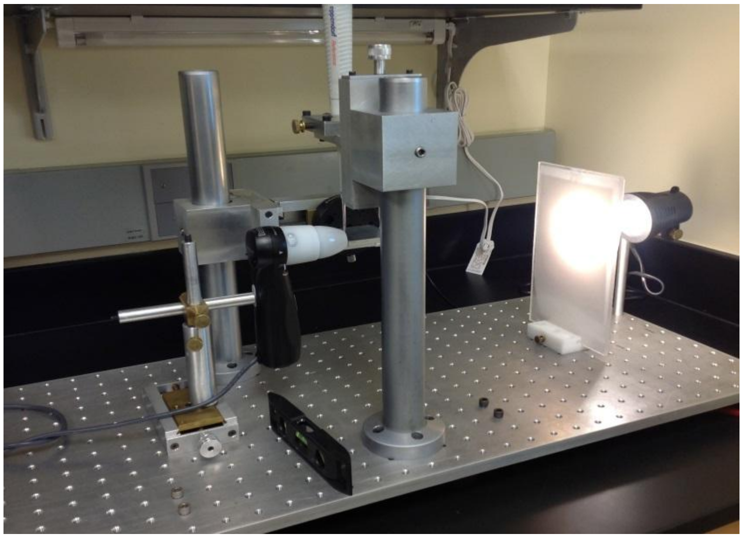

Figure 2.10. Laboratory-made system to measure water contact angle. This instrument was constructed by Dr. Hamid Mortazavian of OSU.

To measure the hydrophobicity of the surfaces, we used the sessile drop method with a laboratory-made contact angle instrument to determine the water contact angle. (Figure 2.10) The equipment consisted of a horizontal stage to mount a solid sample, a micrometer pipette to form a liquid drop, an illumination source used to assist the observation, and a high resolution Proscope camera (capable of recording 15 fps at a 640×480 resolution), which was integrated to take a photograph of the sessile drop on the surface. Water contact measurements were usually done by taking images of 3-5 μL deionized water droplets placed on different spots of the surface. The use of the high resolution camera enables detailed examination of the three-phase contact point of the surface. Then the contact angle was analyzed using a Low-Bond Axisymmetric Drop Analysis Software (LB-ADSA), which is included in the Image J software.[30] Figure 2.11 shows the fitting of the water droplet image using the LB-ADSA approach.

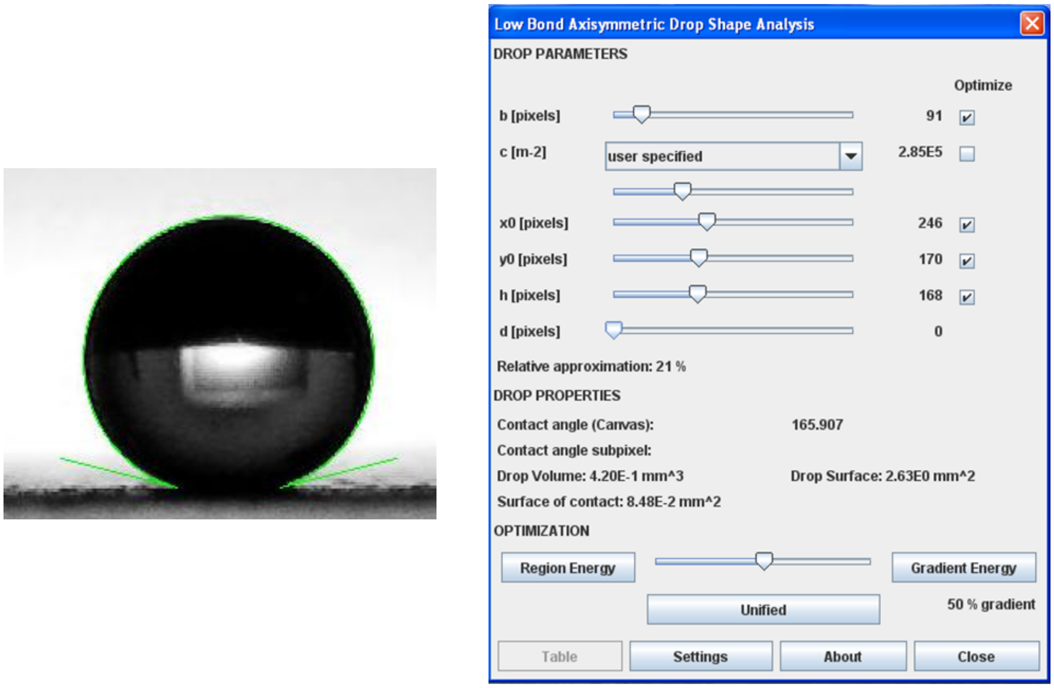

Low Bond Axisymmetric Drop Shape Analysis

DROP PARAMETERS

		Optimize
b [pixels]	91	☑
c [m-2] user specified	2.85E5	☐
x0 [pixels]	246	☑
y0 [pixels]	170	☑
h [pixels]	168	☑
d [pixels]	0	

Relative approximation: 21 %

DROP PROPERTIES

Contact angle (Canvas): 165.907

Contact angle subpixel:

Drop Volume: 4.20E-1 mm^3

Drop Surface: 2.63E0 mm^2

Surface of contact: 8.48E-2 mm^2

OPTIMIZATION

50 % gradient

Figure 2.11. Droplet of water on treated fluorosilane diatomaceous earth on epoxy coating and the LB-ADSA interface with appropriate parameters to fit a circle to the droplet.

This method has several advantages with comparison to other contact angle methods, such as, simplicity and need of only a small amount of liquid and small surface of substrate to detect the contact angle.

2.5.2. Scanning Electron Microscopy

Scanning Electron Microscopy (SEM) is a technique which produces an image of a sample by scanning it with a beam of electrons. This equipment is composed of the electron gun, which produces an electron beam; electromagnetic lenses and apertures, which help the focus the electron beam on the specimen; the vacuum system, which allows the electron beam to pass through the column without interference of air molecules; the specimen stage; and the signal detector and display components. Figure 2.12 shows a schematic diagram of SEM.

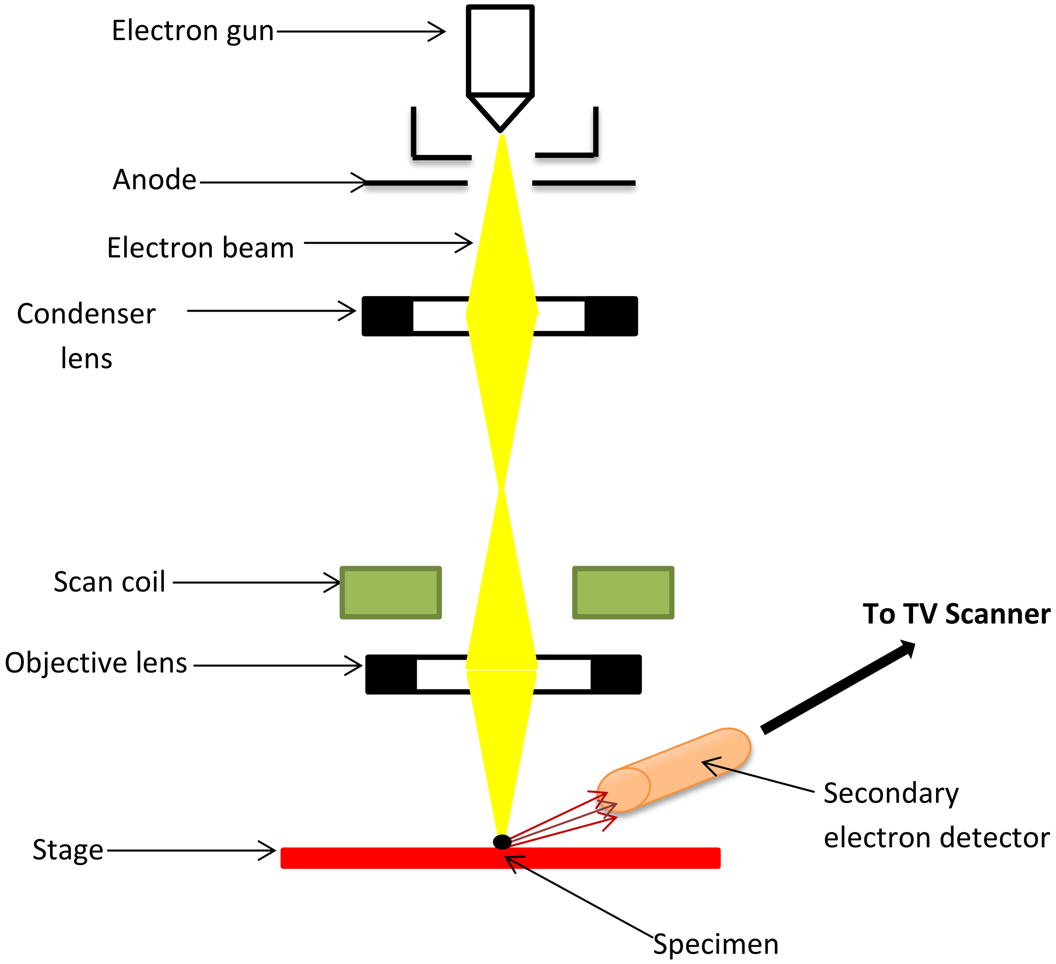

Figure 2.12. Schematic diagram of a SEM system.

SEM has many advantages over traditional microscopy, such as revealing information about the sample including external morphology and topography, chemical composition, crystalline structure, and orientation of materials making up the sample. Additionally, SEM has easy sample preparation methods and allows for large numbers of samples to be analyzed in short times.

2.5.3. Thermogravimetric analysis

The principle of thermogravimetric analysis (TGA) measures the mass change of a sample as a function of temperature. During the measurement, samples are heated under nitrogen or air with a constant heating rate while measuring the mass change with temperature. The TGA technique measures the mass loss or gain due to decomposition, oxidation, or dehydration. The TGA instrument is basically composed of a sample holder, microbalance, furnace with gas flow control, thermostat, and thermocouple (temperature sensor). A schematic diagram of TGA instrument is shown in Figure 2.13

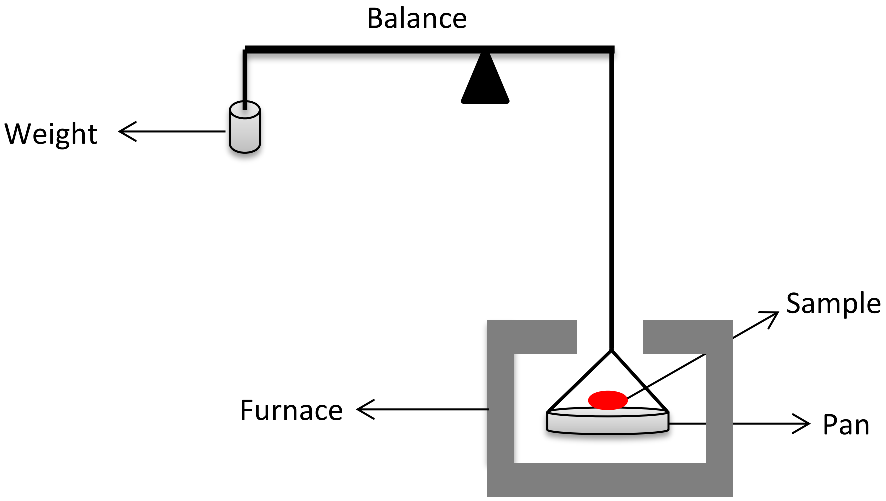

Figure 2.13. Schematic diagram of TGA

2.5.4. Brunauer-Emmett-Teller and pore size analysis

In this study, the surface area measurement we done using the Brunauer-Emmett-Teller (BET) method.[31] The BET equation is used to determine the specific surface area; it uses adsorbing non-corrosive gases like nitrogen, argon, and carbon dioxide. This method is based on the physical adsorption of gases on the external and accessible internal surface of a porous material. The BET method is the most widely used standard method for the determination of the surface area of porous materials; the equation can be expressed as follows (equation 2.5).[32]

$$\frac{1}{v[\ p_0/p\ -1]} = \frac{c-1}{v_m c} \times \frac{p}{p_0} + \frac{1}{v_m c} \qquad (2.5)$$

In equation 2.5, p and p_0 are the equilibrium and saturated pressure of the adsorbate gas at the temperature of adsorption, v is the volume of gas adsorbed at standard temperature and pressure (STP), and v_m is the volume of gas adsorbed at STP to produce a monolayer on the surface of the sample. The constant c is called the BET constant and it is dimensionless, and depends on the type of sample. The enthalpy of the adsorbate on the sample can be calculated using the parameters of a linear regression of the BET plot at the linear region is limited to $0.05 \leq p/\ p_0 \leq 0.3$. From the linear regression, the slope is equal to $(c\text{-}1)/\ v_\mathrm{m}c$, and intercept, is equal to $1/\ v_\mathrm{m}c$. With the help of linear regression, the BET constant, and the monolayer adsorbed gas quantity, v_m can be determined using equation 2.6 and 2.7; the slope, S, and intercept, I, of the of the linear BET fit of $1/v[(p_0/p)\text{-}1]$ as a function of p/p_0:

$$c = 1 + \frac{S}{I} \qquad (2.6)$$

$$v_m = \frac{1}{S+I} \qquad (2.7)$$

The mass of the adsorbed gas, v_m, to form the monolayer was helpful for calculating the total surface area (S_Total), in m^2, and the specific surface area (S_BET), in m^2/g according to equation 2.8 and 2.9.

$$S_{Total} = \frac{v_m N A_x}{V} \qquad (2.8)$$

$$S_{BET} = \frac{S_{Total}}{a} \quad (2.9)$$

where A_x is the cross sectional area of the gas. For krypton at the temperature of liquid nitrogen, A_x is 0.210 nm^2; while for nitrogen molecules it is 0.162 nm^2. N is Avogadro's number, V the molar volume of the adsorbate gas, and a the mass of the solid sample or adsorbent. The specific surface area (S_{BET}) can be calculated by dividing the total surface area by weight of the solid sample.

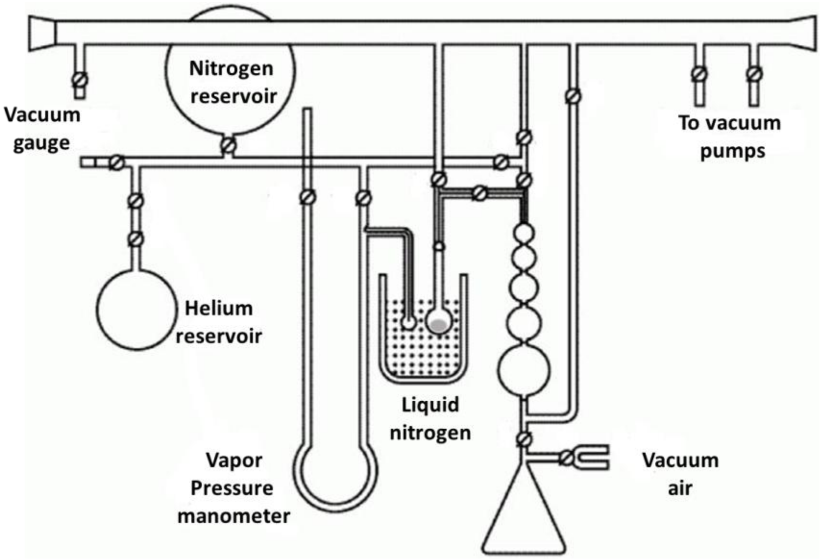

Figure 2.14. A schematic diagram of the BET instrument. Diagram from web site: particle.dk.

Density functional theory (DFT) and computer simulation methods have been developed as powerful techniques for the modelling of the sorption and phase behavior of fluids on porous materials. In contrast to DFT and local density functional theory (LDFT), the non-local density functional theory (NLDFT) and Monte Carlo computer simulation techniques provide a more accurate approach to calculate the pore size and pore volume distributions.[33-36] These methods are widely used to characterize micro- and mesoporous structures of silica, carbon, and zeolites.[34,37-39] NLDFT and Monte Carlo simulation pore size distribution are based on a solution of the generalized adsorption isotherm equation. This equation is based on the intermolecular potentials of the adsorbate/adsorbate and adsorbate/adsorbent interactions. This macroscopic approach is based on the assumption that the total isotherm consists of different numbers of single-individual pores. Then each single-pore isotherm was multiplied by their relative distribution ($f(w)$) as shown in below;

$$N\left(\frac{P}{P_0}\right) = \int_{W_{min}}^{W_{max}} N\left(\frac{P}{P_0}, W\right) f(W)dW \qquad (2.10)$$

where $N(P/P_0)$ is the experimental adsorption isotherm, W is pore width and $N(P/P_0,W)$ is the isotherm of a single pore of width W and $f(W)$ is the pore size distribution function.

2.5.5. Differential Scanning Calorimetry

Differential scanning calorimetry (DSC) is a thermal analytical technique, which is used to measure the temperature and heat flow associated transitions in materials as a function of time and temperature under controlled conditions such as inert atmosphere, temperature, time, and pressure. DSC is used to examine and compare materials with each other with the help of their thermal transitions. There are several thermal transition events such as glass transitions, melting, crystallization, and phase changes (in liquid crystals and organics), which can be measured both quantitatively and qualitatively. DSC is widely used to analyze polymers and organic chemicals, as well as various inorganic materials. Additionally, it is a fairly rapid analyzing technique with easy sample preparation and simple operation.

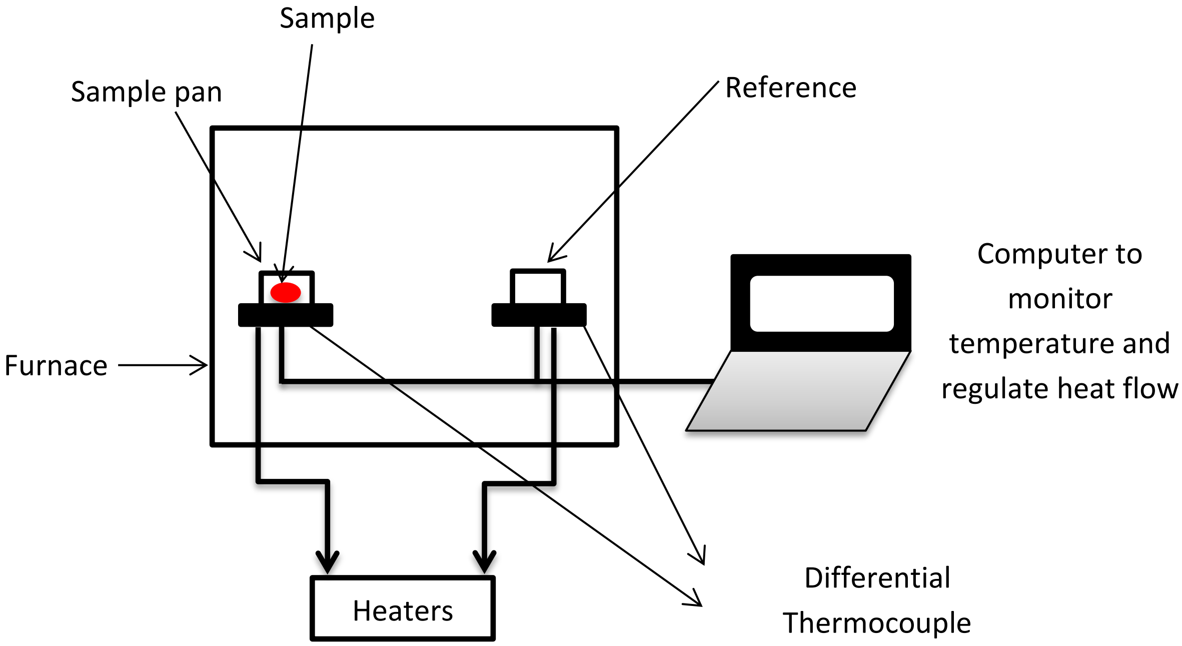

Figure 2.15. Schematic diagram of a heat flux DSC system.

The most common schematic design of the DSC heat flux instrument is shown in Figure 2.15. The sample and the empty reference pans are placed on the top of a heater. When heat is transferred to the pans, differential heat will be adsorbed by the pans to maintain the same temperature. This happens due to the difference in the composition on the each pan. The difference in the heat flow to the sample and to the reference is measured by the thermocouple and recorded on the computer.

Temperature modulated differential scanning calorimetry (TMDSC), was introduced in 1993 by Reading.[40] TMDSC uses the same DSC cell which was used on heat flux DSC, but a sinusoidal temperature oscillation is applied with the conventional linear temperature ramp to yield a non-linear temperature profile. Therefore, TMDSC uses three heating-related variables (heating rate, amplitude of modulation, and frequency of modulation) to obtain more information compared to conventional DSC. The general equation that describes the heat flow for a DSC or a TMDSC experiment is

$$\frac{dQ}{dt} = Cp\frac{dT}{dt} + \ f \ \ T, t \tag{2.11}$$

where dQ/dt is the total heat flow out of a sample (mW/min), dT/dt is the heating rate (J/g), Cp is the heat capacity and f (T,t) is the kinetically-limited heat flow. According to this equation, total heat flow is composed of two differential heat flow components; the heating rate dependent component is Cp(dT/dt) (reversing heat flow), and the absolute temperature dependent components is f(T,t) (non-reversing heat flow). Heat rate dependent transitions are able to be cycled, but absolute temperature dependent transitions, once initiated, cannot be reversed by alternating heating and cooling. Cold crystallization, relaxation, curing, evaporation, and decomposition are some for the thermal events that are observable in the non-reversing heat flow.

TMDSC offers additional unique information that conventional DSC is unable to obtain, including separation of some overlapping transitions into more easily interpreted components, increased sensitivity for detection of weak transitions, increased resolution of transitions without loss of sensitivity, measuring heat capacity and heat flow in a single experiment, and direct determination of thermal conductivity.

2.5.6. Fourier transform infrared spectroscopy

Fourier transform infrared spectroscopy (FTIR), spectroscopy is one of the more widely used methods for study the functional group identification and arrangement of organosilane molecules on the surface. It is a spectroscopic technique based on the rotation and vibration of bonds due to changes in the dipole moment of a molecule. As a result, changing in the dipole moment allows an interaction with the IR radiation. When IR frequency matches with the natural frequency of bond vibration (or rotation); IR radiation can be adsorbed, and amplitude of the vibration will increase and result in IR spectra. These spectra appears as bands at the frequencies of vibration. The position of the IR band depends on the nature of the bonds including bond length, relative mass, and bond strength of the atoms.

2.6. REFERENCES

(1) Gordon, R.; Losic, D.; Tiffany, M. A.; Nagy, S. S.; Sterrenburg, F. A. S. *Trends Biotechnol.* **2009**, *27*, 116.

(2) Lopez, P. J.; Descles, J.; Allen, A. E.; Bowler, C. *Curr. Opin. Biotechnol.* **2005**, *16*, 180.

(3) Calvert, R. *J. Chem. Educ.* **1930**, *7*, 2829.

(4) Mizuhara, Y.; Noguchi, M.; Ishihara, T.; Takita, Y. *J. Am. Ceram. Soc* **1995**, *78*, 109.

(5) Athanassiou, C. G.; Kavallieratos, N. G.; Economou, L. P.; Dimizas, C. B.; Vayias, B. J.; Tomanović, S.; Milutinović, M. *J. Econ. Entomol.* **2005**, *98*, 1404.

(6) Athanassiou, C. G.; Kavallieratos, N. G.; Andris, N. S. *J. Econ. Entomol.* **2004**, *97*, 2160.

(7) Burger, C. A.; Shackelford, C. D. *Can. Geotech. J.* **2001**, *38*, 53.

(8) Vigliani, E. C.; Mottura, G. *Br. J. Ind. Med.* **1948**, *5*, 148.

(9) Korunic, Z. *J. Stored Prod. Res.* **1998**, *34*, 87.

(10) Sims, P. A.; Mann, D. G.; Medlin, L. K. *Phycologia* **2006**, *45*, 361.

(11) Shibuichi, S.; Onda, T.; Satoh, N.; Tsujii, K. *J. Phys. Chem.* **1996**, *100*, 19512.

(12) Shibuichi, S.; Yamamoto, T.; Onda, T.; Tsujii, K. *J. Colloid Interface Sci.* **1998**, *208*, 287.

(13) Nishino, T.; Meguro, M.; Nakamae, K.; Matsushita, M.; Ueda, Y. *Langmuir* **1999**, *15*, 4321.

(14) Ge, L.; Ding, G.; Wang, H.; Yao, J.; Cheng, P.; Wang, Y. *J. Nanomater* **2013**, *2013*, 3.

(15) Ke, Q.; Fu, W.; Wang, S.; Tang, T.; Zhang, J. *ACS Appl. Mater. Interfaces* **2010**, *2*, 2393.

(16) Xu, L.; Zhuang, W.; Xu, B.; Cai, Z. *J. Text. I.* **2011**, *103*, 311.

(17) Xu, L.; Wang, L.; Shen, Y.; Ding, Y.; Cai, Z. *Fibers Polym* **2015**, *16*, 1082.

(18) Xu, B.; Cai, Z.; Wang, W.; Ge, F. *Surf. Coat. Technol.* **2010**, *204*, 1556.

(19) Xu, B.; Cai, Z. *Appl. Surf. Sci.* **2008**, *254*, 5899.

(20) Psarski, M.; Marczak, J.; Celichowski, G.; Sobieraj, G.; Gumowski, K.; Zhou, F.; Liu, W. *Open Phys.* **2012**, *10*, 1197.

(21) Liu, H.; Szunerits, S.; Xu, W.; Boukherroub, R. *ACS Appl. Mater. Interfaces* **2009**, *1*, 1150.

(22) Gu, G.; Dang, H.; Zhang, Z.; Wu, Z. *Appl. Phys. A* **2006**, *83*, 131.

(23) Gu, G.; Tian, Y.; Li, Z.; Lu, D. *Appl. Surf. Sci.* **2011**, *257*, 4586.

(24) Verplanck, N.; Galopin, E.; Camart, J.-C.; Thomy, V.; Coffinier, Y.; Boukherroub, R. *Nano Lett.* **2007**, *7*, 813.

(25) Han, D.; Steckl, A. J. *Langmuir* **2009**, *25*, 9454.

(26) Schutzius, T. M.; Bayer, I. S.; Tiwari, M. K.; Megaridis, C. M. *Ind. Eng. Chem. Res.* **2011**, *50*, 11117.

(27) Wei, Z. J.; Liu, W. L.; Tian, D.; Xiao, C. L.; Wang, X. Q. *Appl. Surf. Sci.* **2010**, *256*, 3972.

(28) Yuan, S.; Pehkonen, S. O.; Liang, B.; Ting, Y. P.; Neoh, K. G.; Kang, E. T. *Corros. Sci.* **2011**, *53*, 2738.

(29) Bracco, G.; Holst, B.; Springer: Berlin; New York, 2013.

(30) Williams, D. L.; Kuhn, A. T.; Amann, M. A.; Hausinger, M. B.; Konarik, M. M.; Nesselrode, E. I. *Galvanotechnik* **2010**, *101*, 2502.

(31) Brunauer, S.; Emmett, P. H.; Teller, E. *J. Am. Chem. Soc.* **1938**, *60*, 309.

(32) Lowell, S.; Shields, J. E. *Powder Surface Area and Porosity*; 2nd ed.; Chapman and Hall: New York, NY, 1984.

(33) Evans, R.; Marconi, U. M. B.; Tarazona, P. *J. Chem. Soc. Faraday Trans.* **1986**, *82*, 1763.

(34) Ravikovitch, P.; Wei, D.; Chueh, W.; Haller, G.; Neimark, A. *J. Phys. Chem. B* **1997**, *101*, 3671.

(35) Ravikovitch, P. I.; Haller, G. L.; Neimark, A. V. *Adv. Colloid Interface Sci.* **1998**, *76*, 203.

(36) Fraissard, J. P. *Physical Adsorption: Experiment, Theory, and Applications*; Springer Science & Business Media, 1997; Vol. 491.

(37) Gelb, L. D.; Gubbins, K. E.; Radhakrishnan, R.; Sliwinska-Bartkowiak, M. *Rep. Prog. Phys.* **1999**, *62*, 1573.

(38) Seaton, N.; Walton, J. *Carbon* **1989**, *27*, 853.

(39) Neimark, A. V.; Ravikovitch, P. I.; Grün, M.; Schüth, F.; Unger, K. K. *J. Colloid Interface Sci.* **1998**, *207*, 159.

(40) Simon, S. L. *Thermochim. Acta* **2001**, *374*, 55.

CHAPTER III

SUPERHYDROPHOBIC SURFACES WITH SILANE-TREATED DIATOMACEOUS EARTH/RESIN SYSTEMS

Note: This chapter was published on *Applied Polymer science*, **2016**, 133 pp 44072. DOI: 10.1001/app.44072, and reprinted with permission from Applied Polymer Science.

3.1. ABSTRACT

Superhydrophobic coatings were prepared using fluorosilane-treated diatomaceous earth (DE) with either polyurethane or epoxy binders. The surface wettability and morphology of the films were analyzed using contact angle measurements and scanning electron microscopy, respectively. The water contact angles were studied as a function of the fluorocarbon fraction on DE and the particle loadings of treated DE in the coating. The contact angles exceeded 150° for coatings with at least 0.02 fluorocarbon fraction (mass of fluorosilane/mass of particle). The water contact angles of the surfaces were dependent on the nature of the binder below 0.2 particle loadings of the superhydrophobic DE particles, but were independent of the binder type after attaining superhydrophobicity.

The results were consistent with the superhydrophobicity resulting from the migration of the superhydrophobic DE moving to and covering the surfaces completely. It was also shown that the treatment with fluorosilanes restricted the pores in DE and reduces the specific surface area of the material. However, these changes had effectively no effect on the superhydrophobicity of the coatings. The results of this work clearly identify some important considerations relative to producing superhydrophobic coatings from inexpensive diatomaceous earth.

3.2. INTRODUCTION

Diatoms are unicellular algae of the class of Bacillariophyceae of Phylum Bacilloriophyta.[1] Diatoms extract silicon from water for the production of their exoskeletons, called frustules or hydrated silica shells.[2,3] When diatoms cells die, their tiny shells sink, and with time, these shells form layers of fossil deposits. These fossilized deposits are known as diatomaceous earth (DE) or kieselgur.[3,4] DE particle sizes can vary between 1 µm and several mm in diameter.[5,6] There are more than 100,000 different species with unique three-dimensional frameworks.[7] Each three-dimensional DE structure contains millions of microscopic, hollow, perforated cylindrical and disk shaped shells. The resulting DE is an inert, highly porous, lightweight, and thermally resistant material.[5,8] Naturally occurring DE is hydrophilic; consequently, it can be used in applications as adsorbents,[4,9] in filtration,[10-14] and in construction materials as a filler.[15] Chemically modified, DE has been used in additional applications, such as materials for superhydrophobic coatings,[6,16-18] metal adsorbents,[4] and drug delivery.[19-22]

Surfaces that form static water contact angles greater than 150° and have sliding angles less than 10° are defined as superhydrophobic surfaces.[23-27] The superhydrophobicity of a solid surface is determined by two factors: its chemical composition and micro-nano hierarchical texture.[23-25,28] Modifying a surface with low energy chemical groups can effectively increase the water contact angle of a solid surface. Surfaces with CF_2 and CF_3 groups generally have low surface energies with contact angles of about 120°on a flat surface.[29,30] Roughening the surface can result in contact angles as high as 160 to 175°, and the surfaces become non-wettable.[31,32] These superhydrophobic coatings are water-repellent, self-cleaning and can be used in many applications, such as anti-icing, anti-oxidation, anti-fogging, non-wetting, buoyancy, and flow enhancement.[33-35]

There are many ways to fabricate superhydrophobic surfaces; they include plasma etching,[36-38] graft-on-graft polymerization,[39] chemical vapor deposition,[40] lithography,[41] sol-gel processing,[42] and self-assembly of low surface energy materials. However, most of the methods used to fabricate superhydrophobic surfaces are complicated, expensive, cannot be used on a large scale, or require special apparatus. Therefore, developing a facile and inexpensive approach for obtaining superhydrophobic surfaces is important. The use of a low-cost material such as diatomaceous earth particles is obviously worth consideration.

Our objective was to produce superhydrophobic coatings using fluorosilane-treated diatomaceous earth particles (DE) with polymer binders that are inexpensive and have low volatile organic contents. DE has already been made into superhydrophobic particles through a variety of novel chemistries.[6,16-18] Puretskiy, et al.[6] showed that a hydrophilic polymer could be *grafted-from* DE to make superhydrophobic anti-iceing materials. Sticking the particles to the top of epoxy coatings provided improved the mechanical properties of the DE layer. However, the multistep process is multi-step complicated. Simpson et al.,[43] Oliveria et al.,[16] and Polizos et al.[17] have shown that fluorosilanes *grafted to* DE could make superhydrophobic DE particles. Coatings with treated DE and polydimethylsiloxane can be improved with the inclusion of graphene oxide.[18] While these studies showed that superhydrophobic coatings could be made using very specific formulations, little has been reported about some of the basic parameters which affect the particles and the behavior and structures of the coatings produced from them.

In order to produce more effective coatings, additional efforts to understand the basic behavior of the coatings systems were undertaken. For example, the effects on the superhydrophobicity of coatings systems on either the amount grafted fluorocarbons on DE or the particle loadings of treated DE in the coatings are not well known. In addition, the roles of different binder systems have not been a focus of reported work. In this study, we report contact angle measurements, scanning electron microscopy, specific surface areas of particles, and pore size measurements to understand the development of superhydrophobicity and to characterize the surface properties of the coatings produced.

3.3. EXPERIMENTAL

Treated diatomaceous earth (FS-DE) samples with different amounts of fluorosilane treatments were obtained from Dry Surface Coatings, (Guthrie, OK). Bisphenol A based epoxy resin (Epon 828) with an epoxy equivalent of 185-192 g was provided by Exel Logistics, (Houston, TX). A cycloaliphatic amine curing agent (Ancamine 2280) with an amine equivalent weight of 110 g was supplied by Air Products and Chemicals (Allentown, PA). An aliphatic polyisocyanate resin based on hexamethylene diisocynate (Desmodur N75) with isocyanate (NCO) content of 16.5 ± 0.3% and an equivalent weight average of 255 was obtained from Bayer MaterialScience, (Baytown, TX). An alkoxylated polyol curing agent (Polyol 3611) with hydroxyl number of 610 ± 25 was supplied by Innovadex, (Overland Park, KS), tetrahydrofuran (THF), and hexane were from Fisher Scientific (Pittsburgh, PA).

Two types of binder solutions were prepared: epoxy binders and polyurethane binders. The epoxy binder solutions were prepared by thoroughly mixing a stoichiometric amount of epoxy resin and curing agent in THF in a ratio of 0.32 g:1 mL. For the polyurethane binder solutions, polyisocyanate and polyol curing agent were prepared in a 1.05 to 1 molar ratio (the excess amount of polyisocyanate ensures complete reaction of the polyol and provides optimal film properties) and mixed with THF in a ratio of 1 g: 1 mL. The binders were mixed in a mechanical shaker for 15 min to make a homogenous solution.

Two different sets of samples were prepared. The first set was a series of coatings made from treated DE samples with different amounts of fluorosilanes. The treated DE particles with different amounts of fluorosilane were then used to prepare epoxy coatings with a fixed 0.25 FS-DE particle loading. The particle loadings are shown as fractions of the mass of the DE (treated or untreated) to the mass of the DE plus polymer resin. In contrast, the fluorocarbon fractions on DE are given as the mass fractions of fluorocarbon (from TGA) to the total mass of treated particles (DE plus fluorocarbon). The second set of samples was a series of epoxy and polyurethane coatings with a single kind of treated DE sample containing a fluorocarbon fraction of 0.036 (FS-DE-1). This fluorocarbon fraction was selected based on having a sufficient amount of fluorosilane for the samples to be superhydrophobic. Different particle loadings of FS-DE-1 were mixed with polymer binders. THF was then added to each vial to make the total volume constant. All the samples were mixed using a mechanical shaker for 30 min.

For contact angle measurements, the FS-DE polymer binder samples were coated on glass slides (7.5 × 2.5 cm^2) cleaned with toluene. Around 0.7 mL from each FS-DE polymer sample was applied onto a glass slide to yield a flat, thin, and uniform layer. The epoxy and polyurethane coated samples were kept on a flat surface to get a uniform thickness. Then air dry and then placed in an oven at 180 °C for 20 min to cure.

Water contact angle measurements were performed using static sessile drop method at room temperature using a homebuilt contact angle measurement instrument with a high-resolution Proscope camera capable of recoding 15 fps at a 640 × 480 resolution. The contact angles were measured using Low Bond Axisymmetric Drop Shape Analysis (LB-ADSA) technique [44-46] by fitting the best profile to an image of 5 µl droplet of deionized water on the surface. The drop shape analysis was done using a drop analysis plugin with ImageJ software. Five readings from different locations on the surface were taken, averaged, and reported as the contact angle for each sample. The reproducibility of the contact angle values on five different places of the sample was less than ± 5° (one standard deviation).

The fluorocarbon fractions in the FS-DE were quantified by thermogravimetric analysis (TGA) using a Q-50 Thermogravimetric Analyzer (TA Instruments, New Castle, DE). The samples were heated from 20 to 950 °C at a heating rate of 20 °C/min under 40 mL/min of continuous air flow.

Nitrogen adsorption–desorption isotherms over a relative pressure range from 0.005 to 0.990 (P/P_0) were done with a NOVA 2200e instrument (Quantachrome Instruments, Boynton Beach, FL) at 77 K to measure the specific surface area and pore size distribution of samples. Samples were outgassed at 50 °C for 3 h under a nitrogen stream prior to the analysis. Surface areas were calculated using at least five relative pressures within the range of linearity of the physical adsorption theory ($0.05 < P/P\mathrm{o} < 0.35$) by applying the Brunauer-Emmet-Teller (BET) [47] equation. The pore size distributions were determined using the density functional theory (DFT) method.[48]

The surface features were characterized with scanning electron microscopy (SEM). For the SEM studies, aluminum pans with an inside diameter of 5 cm were coated with 2 mL of the dispersion. A small portion of the coatings (with the aluminum dish) was cut and attached to the top of an aluminum stub. Samples were then made conductive by sputtering with Au/Pd and imaged using an FEI Quanta 600 SEM (FEI Company, Hillsboro, OR)

3.4. RESULTS

The TGA thermograms for DE and FS-DE samples, shown in Figure 3.1, were used to determine the amount of grafted fluorosilane on the DE. TGA curves show that untreated DE had a mass loss fraction of around 0.026 at 950 °C. The fluorocarbon fraction was calculated using the difference between the mass loss of FS-DE and the mass loss of untreated DE samples at 950 °C. It has been shown for trialkoxysilanes undergoing thermal degradation, that the alcohol groups were removed during hydrolysis and the hydrocarbon chains (fluorocarbon in this case) volatilized. The so called Q-species, with Si bonded to four oxygens, were shown to be the predominant Si species from the coupling agents, left on the particles after the chains degraded.[49] For simplicity, we report only the fluorocarbon fraction of fluorosilane, based only on the mass of fluorocarbon chains. As evident from Figure 3.1, the mass fractions of grafted fluorosilane for different samples were within the range of 0.009-0.085.

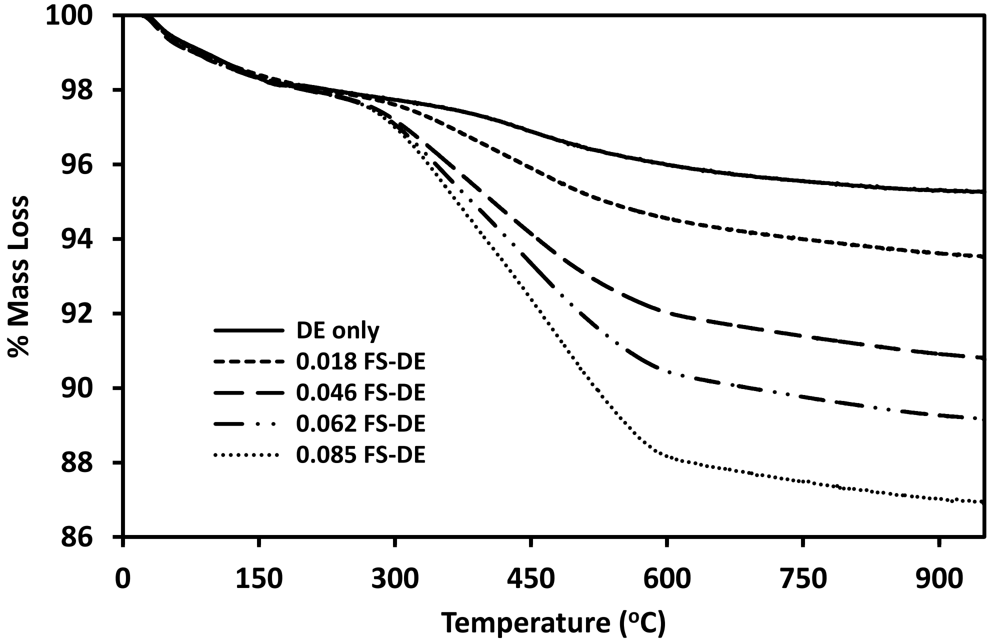

Figure 3.1. The TGA curves of untreated and treated DE (particles without polymer binder) with different fluorocarbon fractions. The labels are based on the fluorocarbon fractions, determined by the difference between the mass loss of each treated DE and the untreated DE sample at 950 °C.

The effect of the amount of the fluorosilane on the water contact angle of treated DE particles was studied. The contact angles for epoxy films with 0.25 particle loading and different fluorocarbon fractions on DE particles are shown in Figure 3.2. Epoxy film with untreated DE had a contact angle of 115°. The hydrophobicity of the epoxy films was enhanced upon the addition of treated DE particles. The contact angle of the coatings increased with increased fluorocarbon fraction on the DE particles. When the fluorocarbon fraction on DE was around 0.02 (0.02 g of fluorosilane in 0.98 g of DE), the maximum hydrophobicity was obtained and the contact angles remained fairly constant with increased fluorocarbon fraction of fluorosilane up to 0.08. In other words, fluorocarbon fractions of 0.02 or more were enough to decrease the surface energy so as to provide superhydrophobicity, i.e., with water contact angles above 160°, in this case.

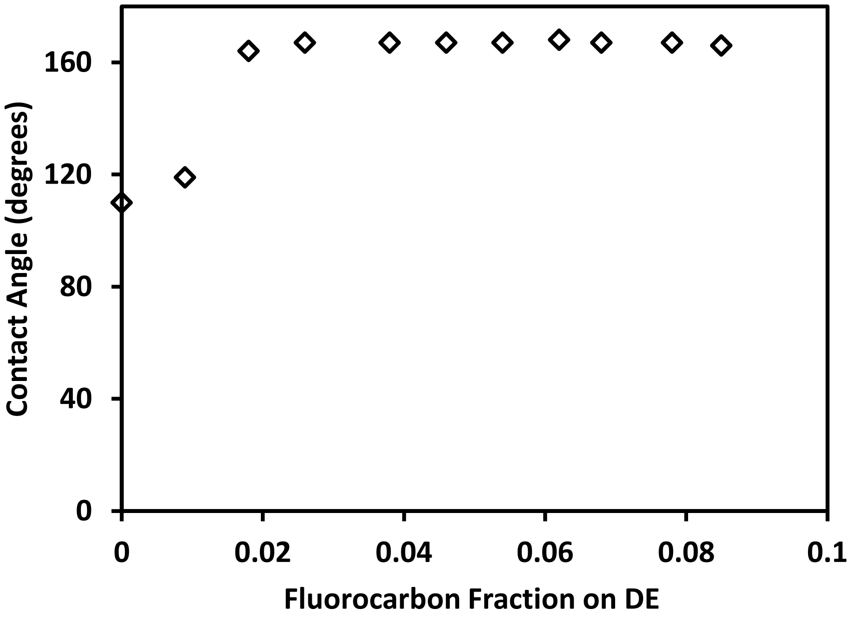

Figure 3.2. Contact angles of epoxy coatings as a function of the fluorocarbon fraction on DE for samples with 25% FS-DE particle loading. The coatings with fluorocarbon fractions above 0.02 were superhydrophobic and the contact angles were independent of the fluorocarbon fraction.

The dependence of the contact angles of epoxy and polyurethane films on the treated DE particle loadings is shown in Figure 3.3. The treated DE particles contained a 0.036 fluorocarbon fraction. Bulk polyurethane and bulk epoxy had contact angles of 72° and 96°, respectively. These contact angle values were consistent with other studies.[50-53] Additional FS-DE particles caused the contact angles to increase, reaching superhydrophobicity with both epoxy and polyurethane after particle loadings of 0.2 of FS-DE. The treated DE particles migrated to the surface easily, likely due to the low viscosity of starting solutions. The ultimate superhydrophobicity after this mass fraction was independent of the starting contact angle of the polymer binder. At mass fractions of the FS-DE larger than 0.2, coatings with both polymer binders behaved similarly, suggesting that the wettability of the coatings might be dominated by the treated DE particles.

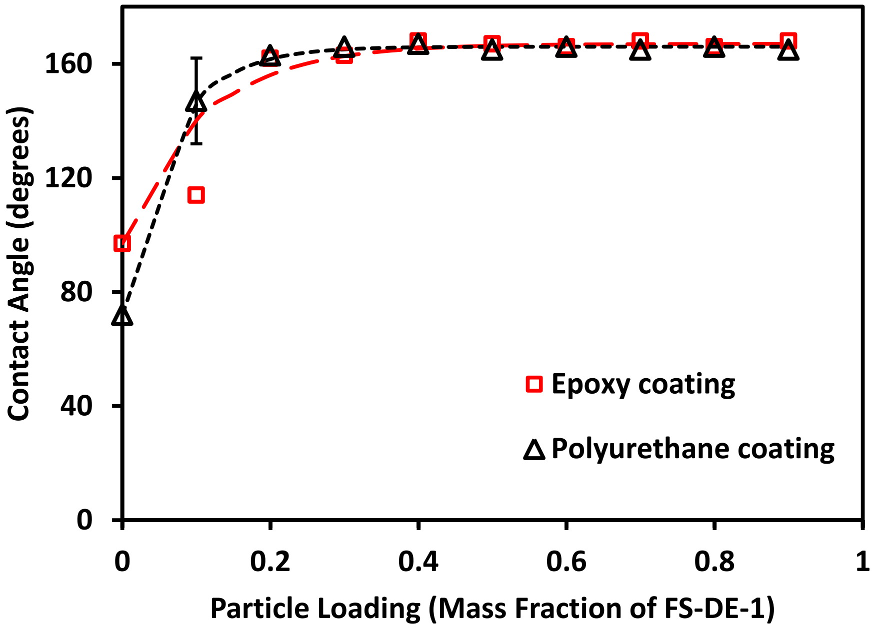

Figure 3.3. The contact angles of epoxy and polyurethane coatings as a function of the FS-DE-1 particle loading. Except for the error bar shown, the standard deviations of the uncertainties in the measurements were less than the size of the symbols for data points. The particles used contained 0.036 fluorocarbon fraction of fluorosilane.

SEM images for untreated DE particles are shown in Figure 3.4. The majority of the particles were disk-shaped and a small fraction of them were cylindrical-shaped. The disk-shaped frustules, as shown in Figure 3.4(a), had typical diameters of 10-20 µm. The particles had highly developed macroporous (larger than 50 nm) structures with the pore diameter of around 250 to 300 nm, which are seen in Figure 3.4(b) and 3.4(c). As shown in Figure 3.4(c), each one of the macropores (about 200 nm) was included mesoporous (2–50 nm) structures with pore diameters in the range of 12-25 nm (Figure 3.4(d)). The specific surface area of untreated DE was measured by us to be 24.1 ± 0.8 m^2/g, as was also found in previous studies.[4,54] Treated DE, with 0.046 and 0.085 fluorocarbon fractions of fluorosilane, were found to have specific surface areas of 17.0 ± 0.2 and 14.9 ± 0.6 m^2/g, respectively. These measurements show that the treatment of DE particles with fluorosilane reduces the specific surface area significantly.[4]

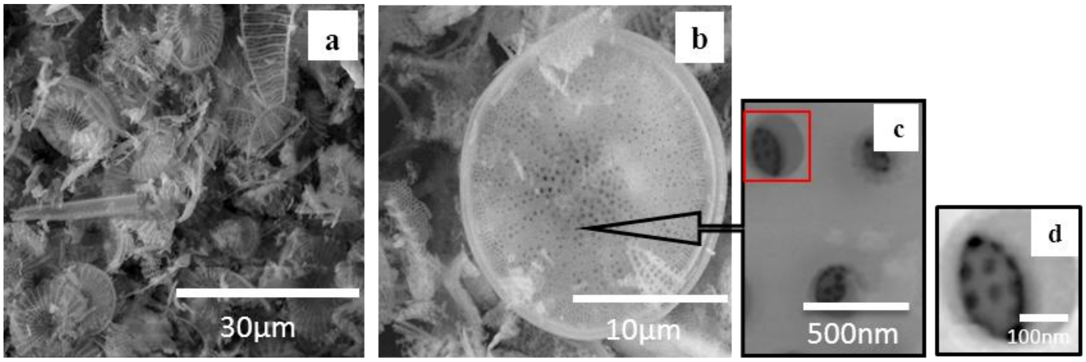

Figure 3.4. SEM images of untreated DE a) scale bar 30 µm, b) typical structure of a single disk-shaped untreated DE with scale bar of 10 µm, c) macroporous (about 200 nm) and mesoporous (dark spots inside the holes, about 25 nm) structures of disk-shaped DE; scale bar 500 nm, and d) enlarged macropore with scale bar of 100 nm. The SEM images show nano- and microscale roughness of DE particles.

The presence of micro roughness was obvious from the SEM images. However, to further confirm the presence of nano size structure on DE particles, we studied the pore size distribution of these particles using the adsorption/desorption isotherms of nitrogen gas. The pore size distribution curves of treated and untreated DE are shown in Figure 3.5 and confirm that DE has primarily mesoporous structures with a pore diameter range of 2-35 nm with majority of them around 14 and 24 nm. The peaks maximum at 14 and 24 nm were likely due to the small pores shown in Figure 3.4(c), which shows pores in the range of 12-25 nm in the SEM. Upon the addition of 0.046 and 0.085 fluorocarbon fraction, the area under the pore size distribution decreased by 40% and 58%, respectively, relative to that of the untreated DE.

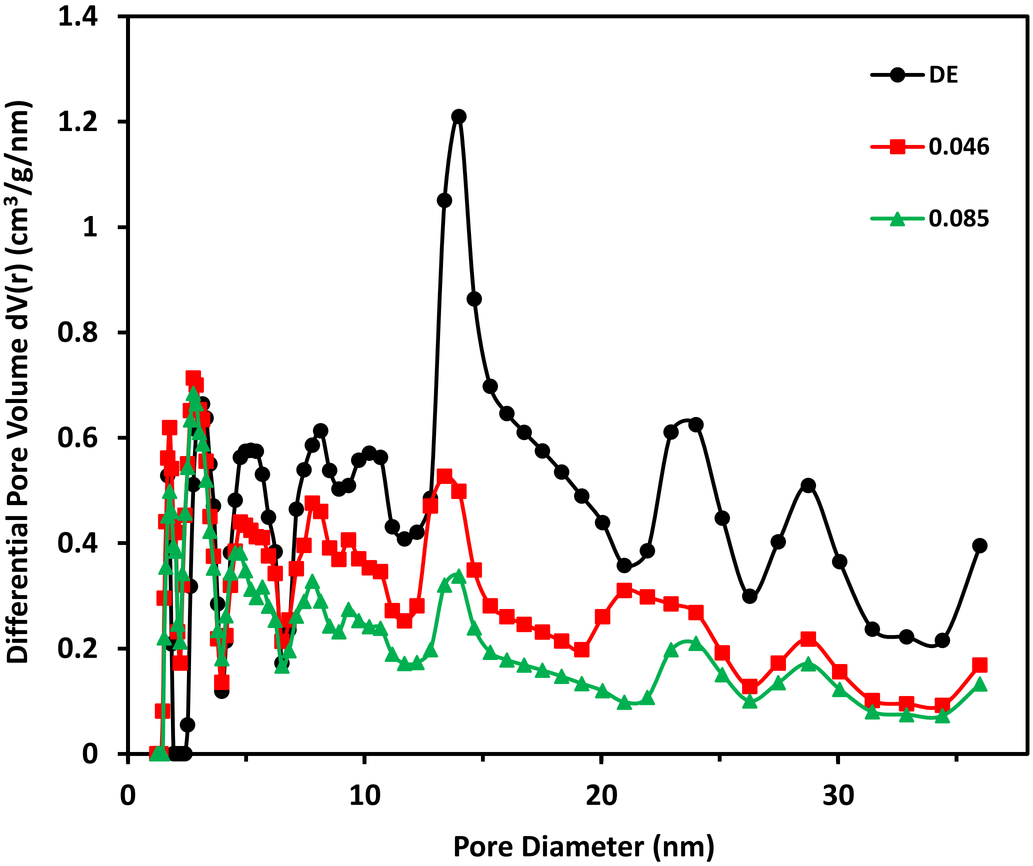

Figure 3.5. Pore size distribution of untreated DE and treated DE with fluorocarbon fractions of 0.046 and 0.085. Grafting with fluorosilane filled up some of the mesoporous

structures of the DE. With increased grafted amounts of fluorosilane, more pores were filled.

SEM images were taken from the coating-air interface of the films. Shown in Figure 3.6(a), the SEM images of the epoxy coating with no FS-DE show a relatively smooth film with no distinct features. With the addition of FS-DE, a rough topography was apparent on the smooth epoxy surface, which can be seen in Figures 3.6(b) to (f). At a particle loading of 0.12 FS-DE, as shown in Figure 3.6(b), the surface shows some parts of FS-DE particles that were coated with the epoxy binder, as well as areas with just epoxy binder on the surface (darker smooth areas). When the particle loading of FS-DE was increased to 0.28, shown in Figure 3.6(c), the particles of DE became clearer with only small polymer regions. Both FS-DE partially covered and fully exposed particles occurred at the surface. At a particle loading of 0.34 FS-DE, Figure 3.6(d), the surface looked similar to that of the fraction of 0.28 with partially polymer binder covered particles of FS-DE on the surface. The SEM micrographs for the samples with additional FS-DE are shown in Figures 3.6(e)-(f). There were no noticeable changes in the micrographs of these FS-DE coatings. They all consisted of large amounts of FS-DE particles on top of the coatings with no significant amount of polymer binder apparent.

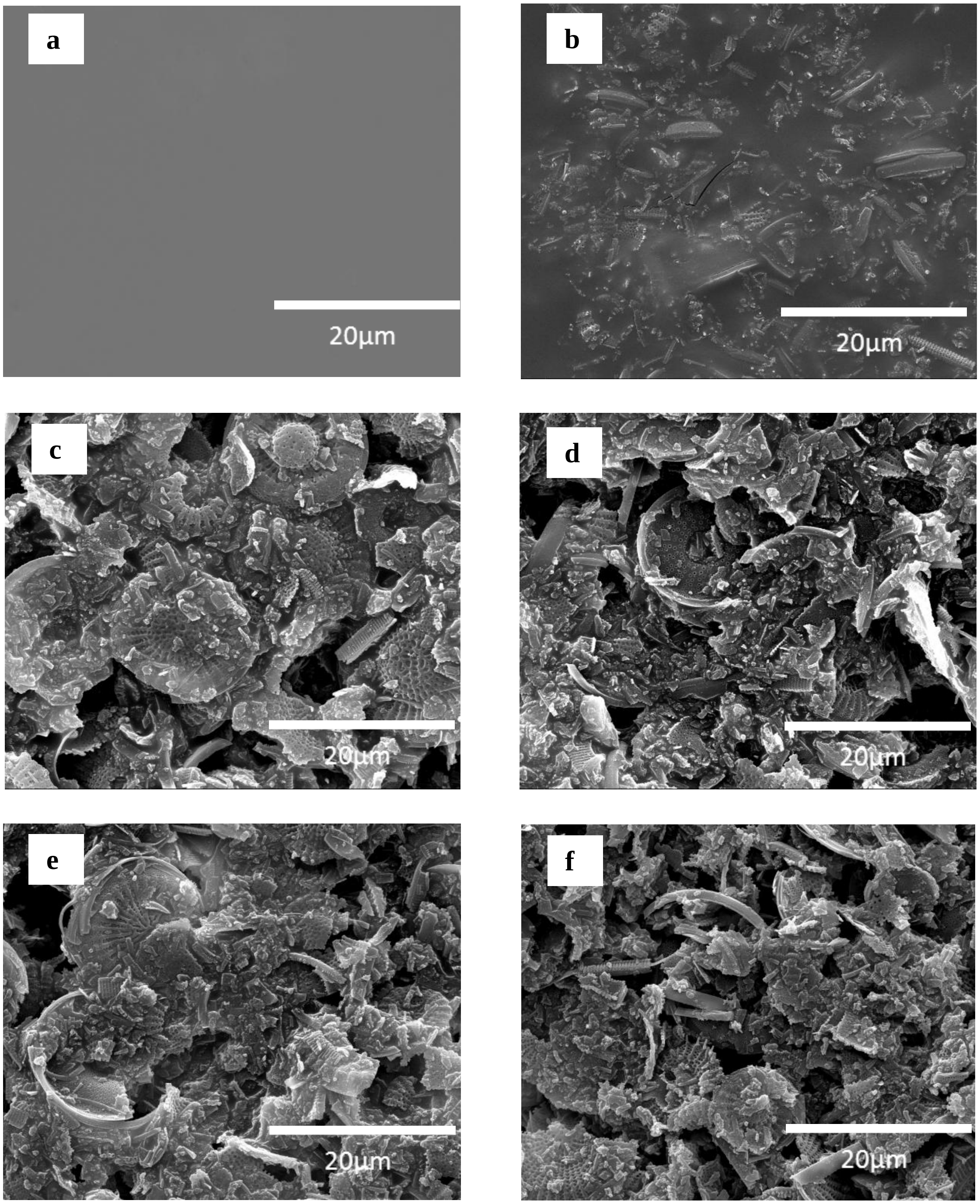

Figure 3.6. SEM images of epoxy coatings with different particle loadings of FS-DE a) epoxy binder, b) 0.12, c) 0.28, d) 0.34 e) 0.40, and f) 0.54 particle loadings of FS-DE. There was no significant change in the surface morphology of the samples with particle loadings of FS-DE greater than 0.28. The scale bar is 20 µm for each micrograph.

The SEM images of the polyurethane coatings with different particle loading amounts of FS-DE are shown in Figure 3.7(a)-(f).

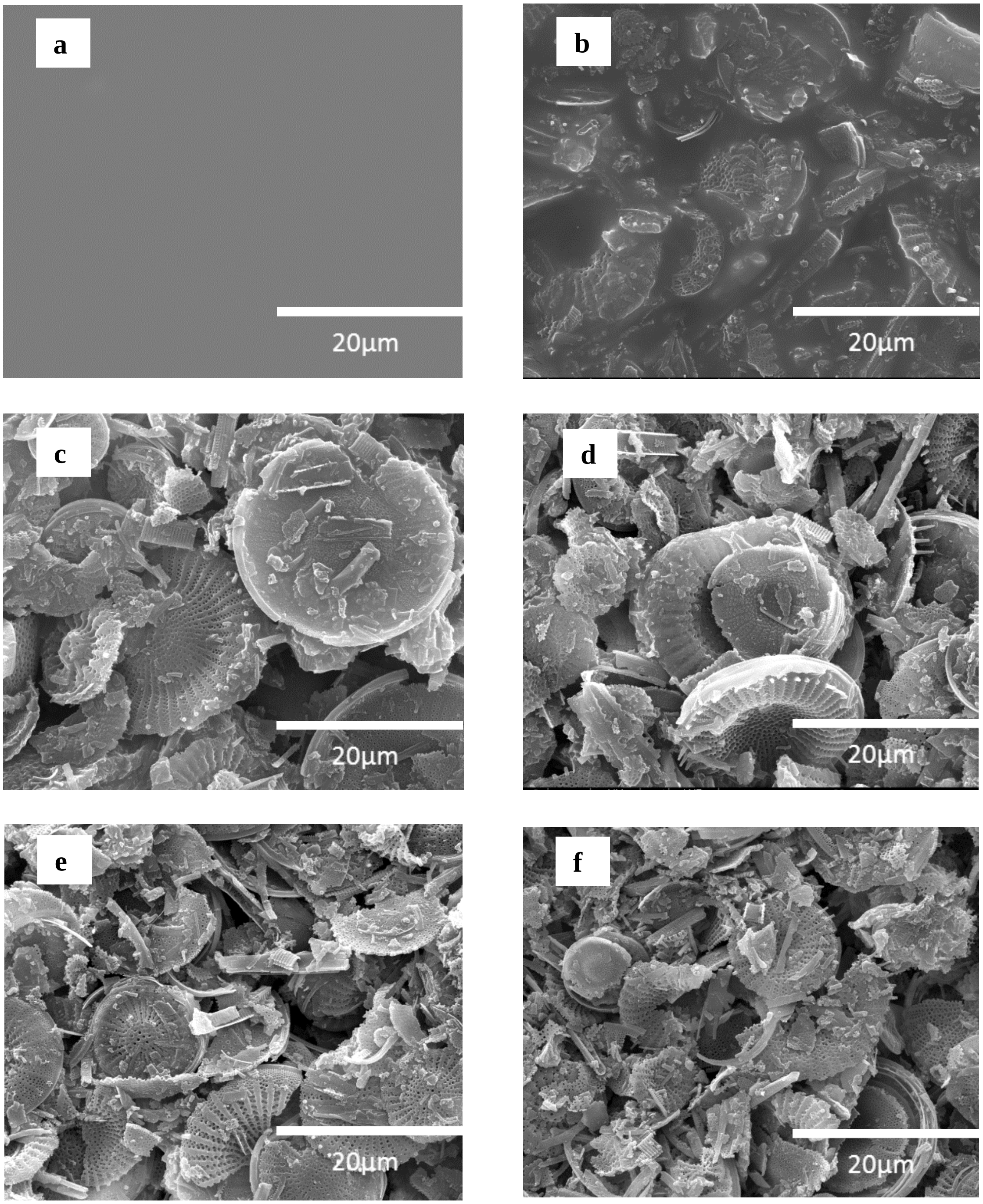

Figure 3.7. SEM images of polyurethane coatings with different particle loadings of FS-DE a) Polyurethane binder, b) 0.11, c) 0.27, d) 0.33, e) 0.38, and f) 0.53 (mass fraction particle loadings of FS-DE). The scale bar is 20 µm for each micrograph.

As can be seen in Figure 3.7(a), the surface of the polyurethane binder coating was smooth and featureless, similar to the epoxy binder without FS-DE. SEM images of the polyurethane coatings with different mass fractions of FS-DE particles were mostly consistent with those of the epoxy coatings. At a mass fraction of 0.11, the surface in Figure 3.7(b), most of the FS-DE particles that appeared on the surface were polyurethane resin coated. There were also areas with just polymer on the surface. As the mass fraction of FS-DE was increased, the surfaces seemed fully coated with FS-DE particles. Although the particles came to the surface, particles were still bound to the surface through the polymer binder in both the polyurethane and epoxy coatings. Particles were not dislodged from the surface by touch and the contact angles remained unchanged after 50 abrading cycles. The surface structure remained constant after about 0.20 mass fraction of FS-DE as shown in Figures 3.7(c)-(f). Only at a fraction of FS-DE particle loadings less than 0.2, did the surface show a noticeable amount of the polyurethane binder.

3.5. DISCUSSION

Treated and untreated DE in the TGA thermograms showed two mass loss steps. The first decomposition step took place around 0-250 °C, attributed to the removal of physically adsorbed water from the surface of the treated and untreated DE particles.[55,56] The second mass loss occurred around 250-950 °C, and corresponded to the dehydroxylation of silanol groups of DE for of untreated DE.[55,56] In treated DE samples, this second mass loss was a combination of both dehydroxylation of silanol groups and degradation of fluorocarbon chains.[57,58] The main difference between the treated and untreated DE was the mass of grafted fluorocarbon. As Figure 3.1 shows, the degradation of fluorocarbon chains had a significant broad mass loss, likely due to the amorphous nature of the grafted fluorocarbon.[59]

Previous studies have shown the absence or presence of the fluorosilanes on the surface through the use of x-ray photoelectron spectroscopy (XPS).[16,17] The F_{1S} region of the XPS spectrum was also indicative of the presence of several different CF species and in conjunction with other atomic species, namely Si, C and O, was used for a surface elemental analysis. In addition, the use of energy dispersive X-ray (EDX) showed that the distribution of F on the particles was uniform. Similar to this report, the presence of the fluorosilane on the DE was responsible for the superhydrophobicity of the particles, and in our case, the coatings.

The surface energies of materials have direct effect on the water contact angle on the surfaces. The results of contact angle measurements as a function of the fluorocarbon fraction, shown in Figure 3.2, indicate that FS-DE was much more hydrophobic than DE. As is known, DE consists primarily, but not exclusively, of hydrated amorphous silica ($SiO_2 \cdot nH_2O$).[5,17] Therefore, the DE surface is rich in hydrophilic silanol groups and can be considered hydrophilic.[19] Treating the surface of DE with fluorosilane decreases the number of free silanol groups and at the same time, the surface is treated with a low surface-energy material.[17,60] As a result, the contact angle of an FS-DE treated surface was larger than that of an untreated DE surface. With an increasing fraction of grafted fluorosilane, more of the surface was covered with low surface energy superhydrophobic material. The presence of the treated DE at the surface resulted in larger contact angles for the coating surfaces. The minimum fluorocarbon fraction grafted to DE (at least for 0.25 particle loading), to achieve a superhydrophobic surface with a contact angle above 160° was 0.02. Larger amounts of fluorosilane grafted to the particles did not change the hydrophobicity of the surface.

Epoxy and polyurethane binders behaved similarly with different treated DE particle loadings when the surface was superhydrophobic and covered with treated particles. The bulk polyurethane showed a smaller water contact angle than bulk epoxy, as shown in Figure 3.3. This difference was due to the differences in the structures of the two bulk polymers. Polyurethane is more polar and more hydrophilic than epoxy resin. However, either of these polymers can be used as binders to make hydrophobic or superhydrophobic materials through the addition of treated DE particles. At particle loadings of 0.2 or greater, the similarity in the superhydrophobic range was because the surface became covered with treated particles. Apparently, the addition of more particles to the surface covers gaps between the particles and reduces the overall air trapped beneath the particles.[61,62]

When FS-DE was mixed with either polymer binder at sufficient particle loading, DE migrated to the surface and produced surface roughness,[16] with the fluorosilane providing the low energy surface. The combination of these two properties (surface roughness and low surface energy material) caused contact angles to increase.[63] With additional loadings of treated DE particles, the contact angles reached superhydrophobic levels with as little as 0.2 FS-DE particle loading. With the addition of more than 0.2 FS-DE particle loading in the coatings, the contact angles reached a plateau and remained around 160° without any significant changes.

It is clear that for our treated DE coatings to be superhydrophobic, the superhydrophobic DE particles need to cover the surface. The fluorination of the particles with silanes makes them somewhat incompatible with the solvent/monomer systems, so that some of the particles move to the air interface. The transport to the surface should depend on the local concentration of particles and the viscosity of the medium. The production of the epoxy and polyurethane coatings used here are based on low molecular mass monomers, so that the initial viscosities are lower than what would be expected for other systems, such as a preformed high molecular mass polymer. This low viscosity is the likely reason why the particle loadings were as small as 0.2 (w/w) for superhydrophobicity. For systems with larger viscosities, it takes larger particle loadings to achieve superhydrophobicity.

The porous nature of DE particles played an important role in the formation of specific surface area and roughness of the particles used. The DE skeletons from different sources have unique shapes, such as disk, triangular, funneled, and spiny. From Figure 3.4, SEM micrographs of untreated DE showed that the DE samples used by us were mostly composed of disk shaped particles with diameters of 10-20 µm. A small portion of the particles in the sample were cylindrically shaped with diameters less than 2 µm. The SEM results indicated that the DE particles have both nano- and micro-scale roughness, which are necessary for superhydrophobic surfaces,[64,65] resulting in macro- and mesopores. We estimate that the contribution of mesopores to the surface area of untreated DE was four times larger than that from the macropores, which is in a good agreement with previous studies.[13,66] The pore size distribution results suggested that the majority of mesopores of DE were in the range of 12 to 30 nm, in agreement with the SEM results. The pore size distribution intensities decreased 40% for treated DE with 0.046 fluorocarbon fraction. This effect also seems to have resulted in a 30% reduction in specific surface area of the treated sample. Increasing the amount of fluorosilane to 0.085 fluorocarbon fraction of DE, reduced both porosity and specific surface area of treated samples further. The area under the pore size distribution and the specific surface area decreased 58% and 38%, respectively, compared to those of untreated DE. This result suggested that the fluorosilane either clogged or constricted the mesopores of the DE particles. Nevertheless, the macro- and mesoporosity sufficient for superhydrophobicity was retained.

The wettability of the coatings prepared with the treated DE particles depended on the amount of treated DE that migrated to the surface of the coatings. The epoxy and polyurethane coatings surfaces with small particle loadings had a mixture of the polymer binder and a small amount of FS-DE particles. In these samples, the surfaces did not have the suitable roughness and low surface energy necessary to be superhydrophobic. The correlation of the contact angle measurements and SEM micrographs was very strong. With particle loadings greater than 0.20 of FS-DE, sufficient numbers of particles were able to come to the surface providing the necessary surface roughness to be superhydrophobic.

3.6. CONCLUSIONS

A simple process has been developed to produce superhydrophobic coatings based on fluorocarbon-treated DE. This material holds promise for producing superhydrophobic coatings with water contact angles around 160°. The measurements made allow insight into the formation of superhydrophobic coatings, including a simple pathway, and the requirements (minimum fluorocarbon content, minimum particle loading, and transport of the particles to the surface) to produce superhydrophobic coatings with relatively inexpensive ingredients.

The amount of fluorocarbon (fluorocarbon fraction) required on the surface of the particles for superhydrophobicity with either polyurethane or epoxy coatings was 0.02 (mass of fluorocarbon/mass of particle). A minimum particle loading of treated-DE was determined to be about 0.2 for superhydrophobic coatings. At compositions greater than these two critical amounts, the nature of the resin system, polyurethane vs. epoxy, did not affect the water contact angles of the coatings. The reason for the resin independence of the coatings in the superhydrophobic range, was that the some of the fluorosilane-treated superhydrophobic particles escaped the low-viscosity resin mixture to reside at the air interface where they remained in the cured coating. For superhydrophobicity, the surfaces of the coatings were particle covered, as shown by SEM, with little or no exposed polymer. The fluorosilane treatments reduced the specific surface area of the particles and reduced their pore volumes, but these effects did not affect the superhydrophobicity. The surface roughness from the DE particles remained sufficient for superhydrophobicity.

3.7. ACKNOWLEDGMENTS

The authors thank Dry Surface Coatings, Guthrie, OK for supplying the raw materials for this work and helpful discussions about the particles used.

3.8. REFERENCES

(1) Vrieling, E. G.; Beelen, T. P. M.; van Santen, R. A.; Gieskes, W. W. C. *J. Biotechnol.* **1999**, *70*, 39.

(2) Gültürk, E. A.; Güden, M.; Taşdemirci, A. *Composites Part B* **2013**, *44*, 491.

(3) Korunic, Z. *J. Stored Prod. Res.* **1998**, *34*, 87.

(4) Yuan, P.; Liu, D.; Tan, D.-Y.; Liu, K.-K.; Yu, H.-G.; Zhong, Y.-H.; Yuan, A.-H.; Yu, W.-B.; He, H.-P. *Microporous Mesoporous Mater.* **2013**, *170*, 9.

(5) Fowler, C. E.; Buchber, C.; Lebeau, B.; Patarin, J.; Delacôte, C.; Walcarius, A. *Appl. Surf. Sci.* **2007**, *253*, 5485.

(6) Puretskiy, N.; Chanda, J.; Stoychev, G.; Synytska, A.; Ionov, L. *Adv. Mater. Interfaces* **2015**, *2*.

(7) Round, F. E.; Crawford, R. M.; Mann, D. G. *Diatoms: Biology and Morphology of the Genera*; Cambridge University Press: New York, 2007.

(8) Jing, Y.; Jing, Z.; Ishida, E. H. *Ind. Eng. Chem. Res.* **2013**, *52*, 17865.

(9) Aivalioti, M.; Papoulias, P.; Kousaiti, A.; Gidarakos, E. *J. Hazard. Mater.* **2012**, *207–208*, 117.

(10) Rottman, J.; Platt, L. C.; Sierra-Alvarez, R.; Shadman, F. *Chem. Eng. J.* **2013**, *217*, 212.

(11) van Garderen, N.; Clemens, F. J.; Kaufmann, J.; Urbanek, M.; Binkowski, M.; Graule, T.; Aneziris, C. G. *Microporous Mesoporous Mater.* **2012**, *151*, 255.

(12) Ediz, N.; Bentli, İ.; Tatar, İ. *Int. J. Miner. Process.* **2010**, *94*, 129.

(13) Losic, D.; Rosengarten, G.; Mitchell, J. G.; Voelcker, N. H. *J. Nanosci. Nanotechnol.* **2006**, *6*, 982.

(14) Losic, D.; Triani, G.; Evans, P. J.; Atanacio, A.; Mitchell, J. G.; Voelcker, N. H. *J. Mater. Chem.* **2006**, *16*, 4029.

(15) Posi, P.; Lertnimoolchai, S.; Sata, V.; Chindaprasirt, P. *Constr. Build. Mater.* **2013**, *47*, 896.

(16) Oliveira, N. M.; Reis, R. L.; Mano, J. F. *ACS Appl. Mater. Interfaces* **2013**, *5*, 4202.

(17) Polizos, G.; Winter, K.; Lance, M. J.; Meyer, H. M.; Armstrong, B. L.; Schaeffer, D. A.; Simpson, J. T.; Hunter, S. R.; Datskos, P. G. *Appl. Surf. Sci.* **2014**, *292*, 563.

(18) Nine, M. J.; Cole, M. A.; Johnson, L.; Tran, D. N. H.; Losic, D. *ACS Appl. Mater. Interfaces* **2015**, *7*, 28482.

(19) Bariana, M.; Aw, M. S.; Kurkuri, M.; Losic, D. *Int. J. Pharm.* **2013**, *443*, 230.

(20) Vasani, R.; Losic, D.; Cavallaro, A.; Voelcker, N. *J. Mater. Chem. B* **2015**, *3*, 4325.

(21) Milović, M.; Simović, S.; Lošić, D.; Dashevskiy, A.; Ibrić, S. *Eur. J. Pharm. Sci.* **2014**, *63*, 226.

(22) Losic, D.; Yu, Y.; Aw, M. S.; Simovic, S.; Thierry, B.; Addai-Mensah, J. *Chem. Commun.* **2010**, *46*, 6323.

(23) Crick, C. R.; Parkin, I. P. *Chem. Eur. J* **2010**, *16*, 3568.

(24) Erbil, H. Y.; Cansoy, C. E. *Langmuir* **2009**, *25*, 14135.

(25) Yao, X.; Chen, Q.; Xu, L.; Li, Q.; Song, Y.; Gao, X.; Quéré, D.; Jiang, L. *Adv. Funct. Mater.* **2010**, *20*, 656.

(26) Tourkine, P.; Le Merrer, M.; Quéré, D. *Langmuir* **2009**, *25*, 7214.

(27) Furuta, T.; Sakai, M.; Isobe, T.; Nakajima, A. *Langmuir* **2010**, *26*, 13305.

(28) Sakai, M.; Kono, H.; Nakajima, A.; Sakai, H.; Abe, M.; Fujishima, A. *Langmuir* **2009**, *26*, 1493.

(29) Shibuichi, S.; Yamamoto, T.; Onda, T.; Tsujii, K. *J. Colloid Interface Sci.* **1998**, *208*, 287.

(30) Tsujii, K.; Yamamoto, T.; Onda, T.; Shibuichi, S. *Angew. Chem. Int. Ed. Engl.* **1997**, *36*, 1011.

(31) Onda, T.; Shibuichi, S.; Satoh, N.; Tsujii, K. *Langmuir* **1996**, *12*, 2125.

(32) Shibuichi, S.; Onda, T.; Satoh, N.; Tsujii, K. *J. Phys. Chem.* **1996**, *100*, 19512.

(33) Cao, L.; Jones, A. K.; Sikka, V. K.; Wu, J.; Gao, D. *Langmuir* **2009**, *25*, 12444.

(34) Lai, Y.; Tang, Y.; Gong, J.; Gong, D.; Chi, L.; Lin, C.; Chen, Z. *J. Mater. Chem.* **2012**, *22*, 7420.

(35) Shirtcliffe, N. J.; McHale, G.; Newton, M. I.; Zhang, Y. *ACS Appl. Mater. Interfaces* **2009**, *1*, 1316.

(36) Li, L.; Roethel, S.; Breedveld, V.; Hess, D. *Cellulose* **2013**, *20*, 3219.

(37) Balu, B.; Breedveld, V.; Hess, D. W. *Langmuir* **2008**, *24*, 4785.

(38) Teshima, K.; Sugimura, H.; Inoue, Y.; Takai, O.; Takano, A. *Appl. Surf. Sci.* **2005**, *244*, 619.

(39) Nystrom, D.; Lindqvist, J.; Ostmark, E.; Hult, A.; Malmstrom, E. *Chem. Commun.* **2006**, 3594.

(40) Chen, W.; Fadeev, A. Y.; Hsieh, M. C.; Öner, D.; Youngblood, J.; McCarthy, T. J. *Langmuir* **1999**, *15*, 3395.

(41) Callies, M.; Chen, Y.; Marty, F.; Pépin, A.; Quéré, D. *Microelectron. Eng.* **2005**, *78–79*, 100.

(42) Shirtcliffe, N. J.; McHale, G.; Newton, M. I.; Perry, C. C.; Roach, P. *Chem. Commun.* **2005**, 3135.

(43) Simpson, J. T.; D'urso, B. R.; Google Patents: 2012.

(44) Stalder, A. F.; Melchior, T.; Müller, M.; Sage, D.; Blu, T.; Unser, M. *Colloids Surf., A* **2010**, *364*, 72.

(45) Rotenberg, Y.; Boruvka, L.; Neumann, A. W. *J. Colloid Interface Sci.* **1983**, *93*, 169.

(46) Williams, D. L.; Kuhn, A. T.; Amann, M. A.; Hausinger, M. B.; Konarik, M. M.; Nesselrode, E. I. *Galvanotechnik* **2010**, *101*, 2502.

(47) Lowell, S.; Shields, J. E. *Powder Surface Area and Porosity*; Springer Netherlands, 1991.

(48) Seaton, N. A.; Walton, J. P. R. B.; quirke, N. *Carbon* **1989**, *27*, 853.

(49) Jo, H.; Blum, F. D. *Langmuir* **1999**, *15*, 2444.

(50) Karmouch, R.; Ross, G. G. *Appl. Surf. Sci.* **2010**, *257*, 665.

(51) Syakur, A.; Berahim, H. *Electrical and Electronic Engineering* **2012**, *2*, 284.

(52) Patel, A.; Patel, C.; Patel, M.; Patel, M.; Dighe, A. *Prog. Org. Coat.* **2010**, *67*, 255.

(53) Makal, U.; Uslu, N.; Wynne, K. J. *Langmuir* **2007**, *23*, 209.

(54) Al-Ghouti, M.; Khraisheh, M.; Allen, S.; Ahmad, M. *J. Environ. Manage* **2003**, *69*, 229.

(55) Pimraksa, K.; Chindaprasirt, P. *Ceram. Int.* **2009**, *35*, 471.

(56) Yuan, P.; Yang, D.; Lin, Z.; He, H.; Wen, X.; Wang, L.; Deng, F. *J. Non-Cryst. Solids* **2006**, *352*, 3762.

(57) Choi, M.-C.; Sung, G.; Nagappan, S.; Han, M.-J.; Ha, C.-S. *J. Nanosci. Nanotechnol.* **2012**, *12*, 5788.

(58) Pazokifard, S.; Mirabedini, S.; Esfandeh, M.; Farrokhpay, S. *Adv. Powder Technol.* **2012**, *23*, 428.

(59) Dhôtel, A.; Li, H.; Fernandez-Ballester, L.; Delbreilh, L.; Youssef, B.; Zeng, X. C.; Tan, L. *The Journal of Physical Chemistry C* **2011**, *115*, 10351.

(60) Lee, H.; Owens, J. *J Mater Sci* **2010**, *45*, 3247.

(61) Lin, Y.; Ehlert, G. J.; Bukowsky, C.; Sodano, H. A. *ACS Appl. Mater. Interfaces* **2011**, *3*, 2200.

(62) Li, Y.; Huang, X. J.; Heo, S. H.; Li, C. C.; Choi, Y. K.; Cai, W. P.; Cho, S. O. *Langmuir* **2007**, *23*, 2169.

(63) Shi, X.; Nguyen, T. A.; Suo, Z.; Wu, J.; Gong, J.; Avci, R. *Surf. Coat. Technol.* **2012**, *206*, 3700.

(64) Nine, M. J.; Cole, M. A.; Johnson, L.; Tran, D. N.; Losic, D. *ACS Appl. Mater. Interfaces* **2015**, 7, 28482.

(65) Lima, A. C.; Mano, J. F. *Nanomedicine* **2015**, *10*, 271.

(66) Gordon, R.; Losic, D.; Tiffany, M. A.; Nagy, S. S.; Sterrenburg, F. A. *Trends Biotechnol.* **2009**, *27*, 116.

CHAPTER IV

EFFECT OF ALKYL CHAIN LENGTH ON THE SURFACE PROPERTIES OF SILANE-TREATED DIATOMACEOUS EARTH COATINGS

4.1. ABSTRACT

Modification of diatomaceous earth (DE) was performed using alkyltrimethoxysilanes of different chain lengths (C3, C8, C12, C16, and C18) and the wettability of functionalized DE containing surfaces was studied using water contact angle measurements. We also investigated the thermal properties of these alkyltrimethoxysilane treated DE powders using thermogravimetric analysis and temperature-modulated differential scanning calorimetry (TMDSC). The TMDSC results showed that silanes on the treated DE became more crystalline with increasing chain length for $Cn \geq 12$ and adsorbed hydrocarbon amounts ($AA \geq 2.2$ mg/m^2). The formation of a crystalline/ordered structure from the low-surface energy material led to the formation of superhydrophobic coatings from treated DE. Samples with adsorbed amounts less than 2.2 mg/m^2 and chain lengths shorter than C12 were only hydrophobic. At similar adsorbed hydrocarbon amounts, as the carbon chain length of coupling agents increased, we observed a concomitant increase in the water contact angle.

The water contact angles were also studied as a function of the loading of treated DE particle loadings in polyurethane coatings. The contact angles exceeded 150° for coatings with at least 30% particle loadings of silane-treated DE, and decreased slightly for samples with more than 50% particle loadings due to the reduction of roughness/number of particles on the surface. These results were in agreement with SEM observations. The surface properties of these systems, studied with Brunauer–Emmett–Teller (BET) specific surface area and pore volume measurements, showed that the surface area and porosity of treated DE particles decreased with increased adsorbed hydrocarbon amounts of alkyltrimethoxysilanes.

4.2. INTRODUCTION

Superhydrophobic surfaces have received considerable attention because of their unique potential for applications in water-repellent, self-cleaning, anti-fouling, and anti-icing coatings.[1-7] The development of artificial superhydrophobic surfaces was inspired by natural surfaces such as the lotus leaf, with water contact angles larger than 150°, on which water drops remain almost spherical and easily roll off.[8-9] The superhydrophobicity was found to be a combined effect of both micrometer and nanometer scale roughness and chemical modification of the surface.[5, 10] Superhydrophobic surfaces can be prepared by either creating roughness on low surface energy materials or lowering the surface energy of a surface with the appropriate roughness.[9]

Diatomaceous earth (DE) is a naturally occurring mineral compound, made from fossilized diatoms, and is mainly amorphous silicon dioxide.[11-13] There are many species of diatoms with a variety of unusual morphologies,[14-15] and sizes in the range of less than one micron to more than one millimeter.[16-17] Commercial DE contains 86-94% silicon dioxide (SiO_2). The remaining material is mostly composed of alumina (Al_2O_3) and ferric oxide (Fe_2O_3).[11, 16, 18] The distinctive hollow structure of diatom frustules with microscale and nanoscale porosity causes the diatoms to have significant surface roughness, [19-20] which is an important factor in formation of superhydrophobic materials. DE has attracted considerable attention due to its porous structure, low density, fine particles, and chemical inertness.[11, 21] The hydrophilic nature of DE can also be modified by appropriate surface treatment. Despite the many advantages of DE in a variety of applications,[19, 22-35] very few studies have examined water/DE interactions and the water repellency of chemically-modified DE surfaces, which are important if DE is used in coatings.

Modification of silica surfaces via the reaction of alkyl silanol groups has been studied and used in many chemical applications such as chromatography,[36-37] superhydrophobic coatings,[38] immobilization of biosensors, and catalysis.[39-40] Alkylsilanes can be anchored onto a silica surface through covalent bonds between the hydrolyzed silanes and the hydroxyl groups of the silica. These covalent bonds enable the durable immobilization of the organic moieties and the introduction of hydrophobicity to the surface. Hydrophobic surfaces can be achieved when well-ordered fluoroalkyl or alkyl chains are able to form low energy surfaces[41-45] due to the high density of CF_2, CF_3, CH_2 or CH_3 moiety on surfaces.[41, 46-47] To date, a few studies have reported attempts to tune the superhydrophobicity of DE functionalized with fluorosilane coupling agents.[20, 48-50] However, there do not appear to be any reports on tuning the hydrophobic properties of functionalized DE with non-fluorosilane coupling agents.

In this study, we have investigated the role of both the chain length and carbon content of alkyltrimethoxysilane coupling agents on the hydrophobicity of polyurethane coatings containing treated DE particles. Since the hydrocarbon amounts of the coupling agents change with alkyl chain length, one might choose to compare effects based on either the adsorbed amount (mass) of hydrocarbon or the molecular grafting density (molecules). In this study, we focus on both as both are important. Initially, we compare behavior as a function of the amount (mass) of *adsorbed hydrocarbon* (i.e., only the hydrocarbon material, which does not include the silicon-containing portion) on different silanes. In this way, we somewhat decouple the effects of chain length from the number of molecules on hydrophobicity. The goal is to provide a systematic comparison on how chemical modification of DE with alkyltrimethoxysilane groups can be used to alter the surface wettability and determine the importance of different parameters on hydrophobicity and superhydrobicity.

4.3. MATERIALS AND METHODS

Alkyltrimethoxysilanes with the general formula of $H_3C(CH_2)_{n-1}$-$Si(OCH_3)_3$ with n = 3, 8, 12, 16, and 18, were purchased from Gelest Inc. (Morrisville, PA). Dry Surface Coatings (Guthrie, OK) provided the untreated DE (Celite, mainly composed with disk-shaped particles). An aliphatic polyisocyanate resin based on hexamethylene diisocynate (Desmodur N75) with isocyanate-NCO content of 16.5 ± 0.3% having equivalent weight average of 255 was obtained from Bayer MaterialScience (Baytown, TX). An alkoxylated polyol curing agent (Polyol 3611) with hydroxyl number of 610 ± 25 was supplied by Innovadex (Overland Park, KS). The *p*-toluenesulfonic acid monohydrate (PTSA) was from SigmaAldrich (St. Louis, MO), tetrahydrofuran (THF) was from Fisher Scientific (Pittsburgh, PA), and toluene was from Pharmco-aaper (Brookfield, CT). All chemicals were used as received.

4.3.1. Silylation reaction

A series of DE treated samples with different chain-lengths of alkyltrimethoxysilanes and varying adsorbed hydrocarbon amounts (0.6, 1.6, 2.2, and 3.4 mg/m^2) were prepared in toluene. Previously reported reaction conditions were used in the synthesis of silane treated DE with *p*-toluenesulfonic organic acid as a catalyst.[38] DE (1 g) was placed in a glass vial, 15 mL of toluene was added, and the mixture was mixed on a mechanical shaker for 30 min to wet the DE particles. PTSA monohydrate (~ 0.02 g) and different amounts of alkyltrimethoxysilane were added to each vial. To determine the adsorbed hydrocarbon amounts on the DE, appropriate masses for silanes of different chain lengths were calculated using equation 4.1.

$$AA_{HC} = \frac{[\frac{m_{silane}}{MW_{silane}}] \times MW_{HC} \times 1000}{S_{DE} \times m_{DE}} \tag{4.1}$$

where AA_{HC} is adsorbed hydrocarbon amount (mg hydrocarbon/m^2 DE) from the initial composition, MW_{silane} is the molecular mass of silane (g/mol), MW_{HC} is the molecular mass of hydrocarbon chain portion of corresponding silane (g/mol), S_{DE} is the specific surface area of DE (m^2/g), m_{DE} is mass of DE (g), m_{silane} is amount of silane (g) and the 1000 term converts g to mg.

Glass vials containing DE and alkyltrimethoxysilane mixtures were shaken using a mechanical shaker for 4 h in a 50 °C water bath and then cooled down to room temperature. The alkyltrimethoxysilane functionalized DE samples were then obtained from the reaction medium by passing air through the samples using Pasteur pipettes followed by drying under vacuum at 50 °C for 48 h. The resulting treated DE particles are labeled according to the number of carbons on the chain. For example, DE treated with propyltrimethoxysilane is called C3-TMS treated DE.

The adsorbed hydrocarbon amounts of alkyltrimethoxysilane in treated DE samples were verified with thermogravimetric analysis (TGA) using a Q-50 Thermogravimetric Analyzer (TA Instruments, New Castle, DE). Samples were heated from 20 to 900 °C at a heating rate of 20 °C/min under a 40 mL/min of continuous air flow. Since the samples were not washed, all of the coupling agents used should be adsorbed in the sample. This assumption was checked by TGA, although this check was complicated by the adsorption of PTSA. After correction for PTSA adsorption, the target amounts of coupling agents were found to be within 5% of the estimated value from the initial composition. This level of uncertainty was consistent with studies of other adsorbed silanes and suitably accurate for this work.[51-52]

Temperature modulated differential scanning calorimetry (TMDSC) analysis was carried out using a Q-2000 (TA Instruments, New Castle, DE) to study the melting and freezing of the silanes on the treated DE. The heating and cooling scans were run in the temperature range of -80 to 120 °C with a scan rate of 3 °C/min, modulation amplitude of ± 1.0 °C, and modulation period of 60 s. Fourier transform infrared spectroscopy (FTIR) spectra were taken in transmission mode using a Varian 800 FTIR spectrometer by placing a small amount of dry treated and untreated DE on NaCl plate. The scanning range was from 600 to 4000 cm^{-1} with a spectral resolution of 4 cm^{-1}.

Nitrogen adsorption–desorption isotherms over a relative pressure range from 0.005 to 0.990 (P/P_0) were made with a NOVA 2200e instrument (Quantachrome Instruments, Boynton Beach, FL) at 77 K to measure the specific surface area and pore size distribution of the samples. Samples were outgassed at 50 °C for 3 h under a nitrogen stream prior to the analysis. Surface areas were calculated using at least five relative pressures within the range of linearity of the physical adsorption theory ($0.05 < P/P\text{o} < 0.35$) by applying the Brunauer-Emmet-Teller (BET) equation.[53] The pore size distributions were determined using the density functional theory (DFT) method.[54] The surface features were characterized by scanning electron microscopy (SEM) using an FEI Quanta 600 (FEI Company, Hillsboro, OR). For SEM studies, a dispersion of each sample was coated on an aluminum pan and was attached to the top of an aluminum stud. The samples were then made conductive by sputtering of Au/Pd.

4.3.2. Sample preparation for contact angle measurements

A polyurethane binder solution was prepared by mixing stoichiometric amounts of polyisocyanate and polyol curing agent in THF in a ratio of 3:67 w/w, respectively. In the preparation of the polyurethane binder solution, an excess amount of polyisocyanate was added to ensure complete reaction of the polyol curing agent and the polyisocyanate. The polyisocyanate and polyol curing agents were prepared in a 1.05 to 1 molar ratio. The binder was mixed in a mechanical shaker for 15 min to make a homogenous solution. Treated DE samples were then added to the polyurethane binder in the correct ratio and solutions were mixed using mechanical shaker for 30 min.

All samples for contact angle measurements were prepared by adding 2 mL of the solution mixture to a glass coverslip in an aluminum pan. The samples were kept on a flat surface to air dry and then heated at 140 °C for 15 min to cure the polyurethane coatings. Water contact angle measurements were then performed using the static sessile drop method at room temperature using a homebuilt contact angle measurement instrument and a high resolution Proscope camera.[50] The contact angles were measured using Low Bond Axisymmetric Drop Shape Analysis (LB-ADSA) technique[55-57] by fitting the best profile to an image of 4 µL of deionized water droplet. These droplets were analyzed using ImageJ, drop analysis plugin, software. For each composition studied, two identical coatings mixtures were each used to prepare two coatings, which were cured. For each coating, four images from different locations on the surface were taken, with the average and standard deviation reported for the contact angle. Thus for each reported value, 16 measurements were made.

Effect of chain length and adsorbed hydrocarbon amount: Samples with 3:70 w/w mass ratio of treated DE and polyurethane binder were used to study the effect of chain length and adsorbed hydrocarbon amounts of the coupling agents using water contact angle measurements.

Effect of water droplet stability: Samples with 2.2 mg/m^2 adsorbed hydrocarbon amount and different chain length of alkyltrimethoxysilanes were used to study the stability of water droplets on the surface with time. Treated DE samples were mixed with the polyurethane binder in a ratio of 3:70, w/w.

Effect of mass fraction of treated DE particles: Samples with 3.4 mg/m^2 adsorbed hydrocarbon amount of C12-TMS were used to study the effect of the particle loading of treated DE particle mass fractions on contact angles. Different particle loadings of treated DE (0 – 70 %) were used to prepare these samples.

4.4. RESULTS

4.4.1. Surface properties of untreated and treated DE samples

The TGA curves of untreated DE without and with PTSA are shown in Figure 4.1. In order to observe the decomposition behavior clearly, both the mass loss and its derivative are plotted on the same graph. The derivative curves of both untreated DE without and with PTSA showed a main peak in the temperature range of 20-250 °C. This peak, centered at around 160 °C, was mainly due to the loss of physically adsorbed water.[26, 58] A significant broad mass loss occurred in the range of 250-900 °C for both samples. For DE with and without PTSA, mass losses of around 2.4%[26] and 4.4%, respectively, were found. A 2.4% mass loss was attributed to the dehydroxylation of DE silanol groups due to condensation[52, 59-60] and consistent with the results of other studies.[61]

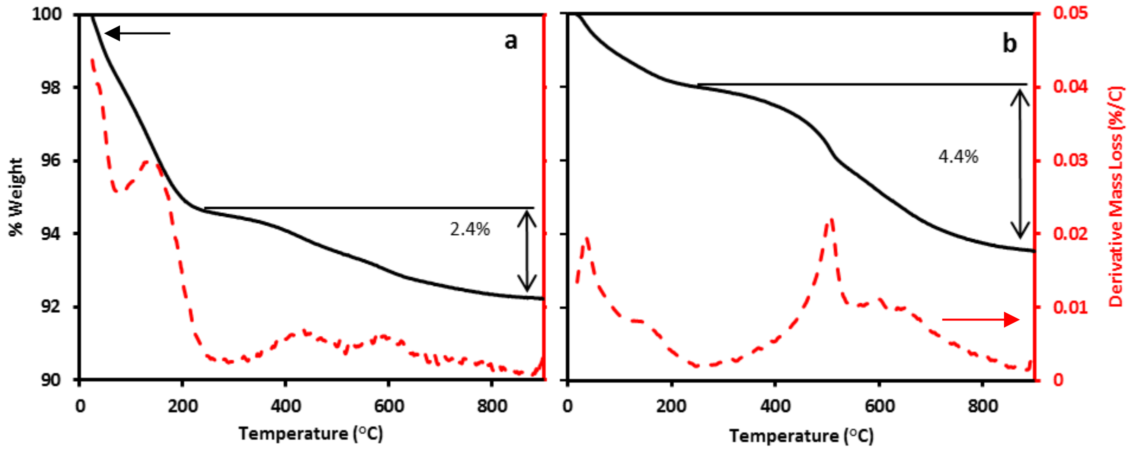

Figure 4.1. TGA curves of untreated DE (a) without and (b) with PTSA (0.88 mg/m^2). The difference between the mass loss of DE with and without PTSA gave the initial PTSA adsorbed amount.

The decomposition of untreated DE with PTSA gave a well resolved peak around 500 °C, in addition to the other peaks present in untreated DE without PTSA, as shown in Figure 4.1(b). Testing a large number of samples showed that this peak was attributed to the decomposition of PTSA. The mass loss difference between Figure 4.1(a) and (b) was due to PTSA.

TGA thermograms were also used to determine the amounts of grafted silane on the surface of DE. The C18-TMS treated DE samples showed the main decomposition step in the range of 250-900 °C and were very broad, as shown in Figure 4.2. This degradation step can be assigned to the decomposition of the hydrocarbon chains.[58] PTSA with untreated DE showed a narrower peak in the same temperature range. The overlapping of the decomposition temperatures of PTSA and adsorbed silanes can be clearly seen in Figure 4.2. Accounting for the PTSA amounts, the amount of adsorbed coupling agent was calculated and was essentially the same as the amount added in the initial solution.

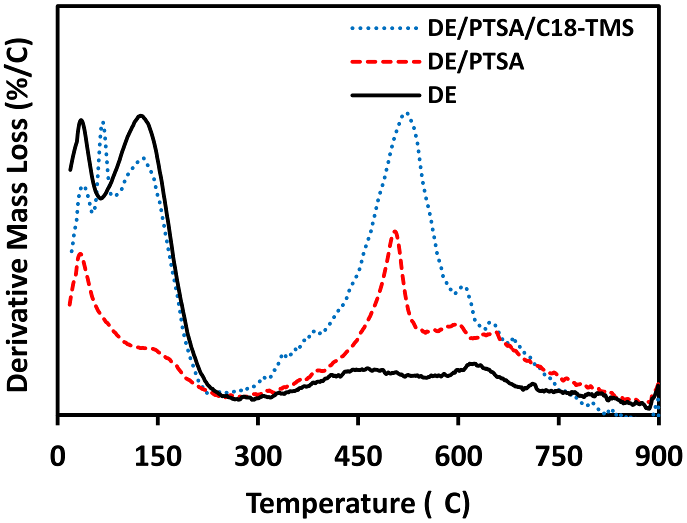

Figure 4.2. Derivative mass loss TGA curves of untreated DE (continuous line), untreated DE with 0.88 mg/m^2 PTSA (dashed line), and 1.6 mg/m^2 C18-TMS with 0.88 mg/m^2 PTSA (dotted line).

FTIR spectra of untreated and alkyltrimethoxysilane grafted DE (C3-TMS to C18-TMS) are shown in Figure 4.3 in the CH stretching region. Untreated DE showed no activity in this region. Alkyltrimethoxysilane treated DE (with 2.2 mg/m^2 adsorbed hydrocarbon amount) showed two prominent peaks at around 2920 and 2850 cm^{-1} showing the asymmetric and symmetric stretching modes of the methylene (CH_2) groups. The resonance at 2958 cm^{-1} corresponded to the CH_3 asymmetric stretching. These peaks confirm the presence of the alkyltrimethoxysilanes on the DE particles. With decreasing chain length of the alkyltrimethoxysilane groups, we observed shifts in the position of CH_2 asymmetric and symmetric stretching peaks to higher frequencies. The peak positions, shifted from 2920 to 2930 cm^{-1} and from 2850 to 2870 cm^{-1} for asymmetric and symmetric CH_2 vibrations, respectively.

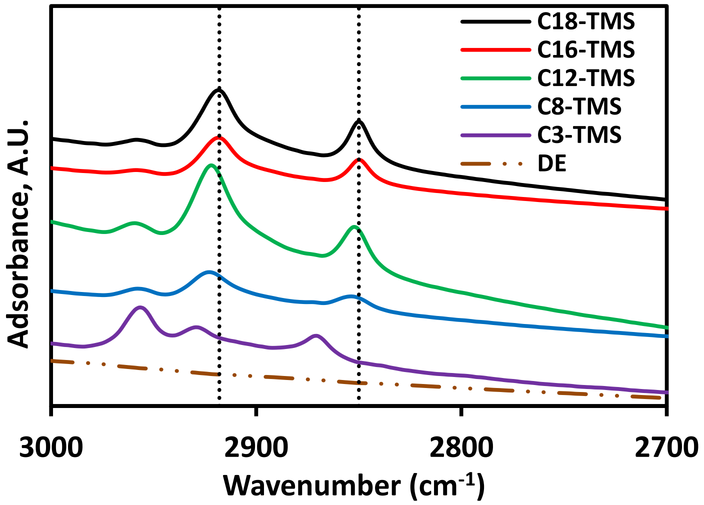

Figure 4.3. C-H stretching region of the FTIR spectra of untreated DE and 2.2 mg/m^2 adsorbed hydrocarbon amounts of alkyltrimethoxysilane treated DE particles (with different chain lengths). Shifts to higher frequency for symmetric and asymmetic CH_2 vibrations with decreasing chain length indicated less order for the shorter chains. The vertical positions are shifted for clarity.

We also investigated the effect of different adsorbed hydrocarbon amounts of the C12-TMS molecular arrangement using FTIR. The frequencies for the CH_2 stretches for C12-TMS with different grafted densities are shown in Figure 4.4. The FTIR spectra in the stretching region of these samples are presented in Figure S4.1 of the **Supporting Information**. Figure 4.4 clearly indicates that as the density of adsorbed coupling agents on the surface increased, the CH_2 symmetric and asymmetric stretching frequencies moved to lower frequency.[62] At the smallest adsorbed amount, 1.8. chains/nm^2 (which corresponds to 0.6 mg/m^2), the CH_2 stretching frequencies were close to the liquid alkane frequencies.[63]

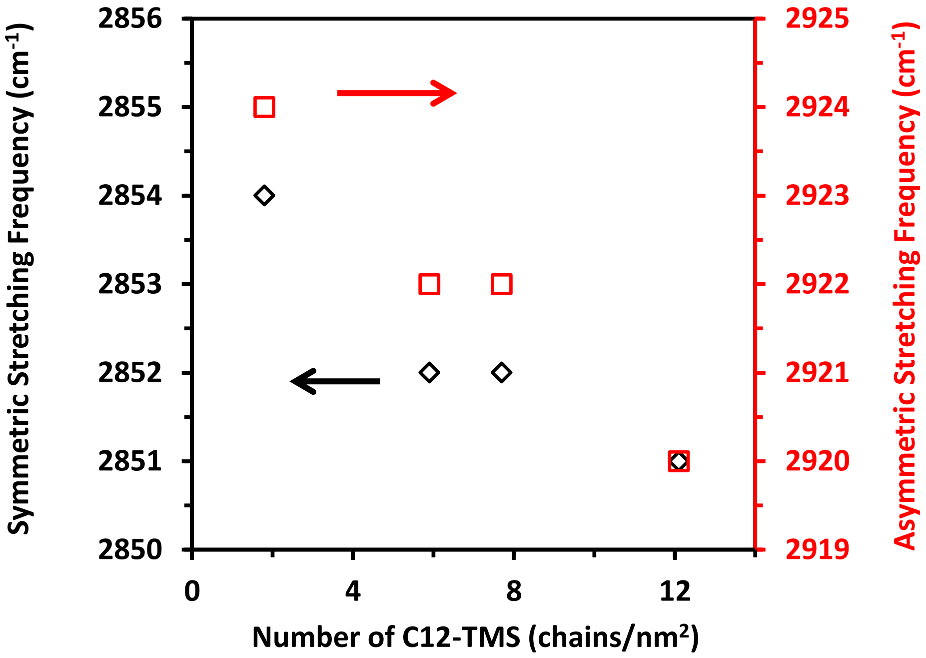

Figure 4.4. Symmetric and asymmetric CH_2 stretching frequencies of C12-TMS as a function of packing densities. The CH_2 symmetric and asymmetric stretching frequencies moved to lower frequencies (indicating more ordered chains) with increased adsorbed amount of coupling agents.

We note that the silanols are not necessarily all directly adsorbed to the surface as single molecules. There is likely the formation of oligomers before adsorption, due to the self-condensation in solution, especially at higher adsorbed amounts. At the larger adsorbed amounts, amounts greater than about 4 chains/nm^2 must be from oligomers.[51] We observed similar behavior with the variation of the packing density of C16-TMS and C18-TMS.

The specific surface areas of untreated and treated DE, as a function of adsorbed hydrocarbon amounts of C16-TMS, are shown in Figure 4.5. A specific surface area of 24.1 ± 0.8 m^2/g was found for the untreated DE. The treated DE samples showed smaller specific surface areas than untreated DE, as was also found in previous studies.[26] Specific surface areas decreased with the adsorbed hydrocarbon amount of C16-TMS. The uncertainties of the measurements were less than the size of the symbols unless otherwise shown.

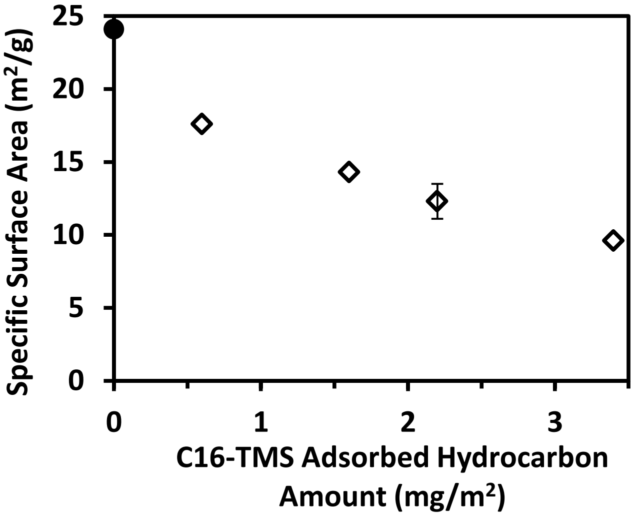

Figure 4.5. Specific surface area of untreated DE (Filled circle) and treated DE with different adsorbed hydrocarbon amounts of C16-TMS. The specific surface area decreased with increased adsorbed hydrocarbon amounts.

Pore size distributions of samples with different adsorbed hydrocarbon amounts of C16-TMS are shown in Figure 4.6. The untreated DE sample showed a heterogeneous distribution of pore diameters with major pore size ranges above 12 nm, and were mostly composed of pore diameters larger than micro pores.[53] The pore-size distribution intensities, decreased with increasing the adsorbed hydrocarbon amount. A similar trend was found for different adsorbed amounts of C18-TMS samples (not shown). The coupling agents filled up some of the pores and decreased the total pore volume resulting in a reduction of the specific surface area and porosity.[64]

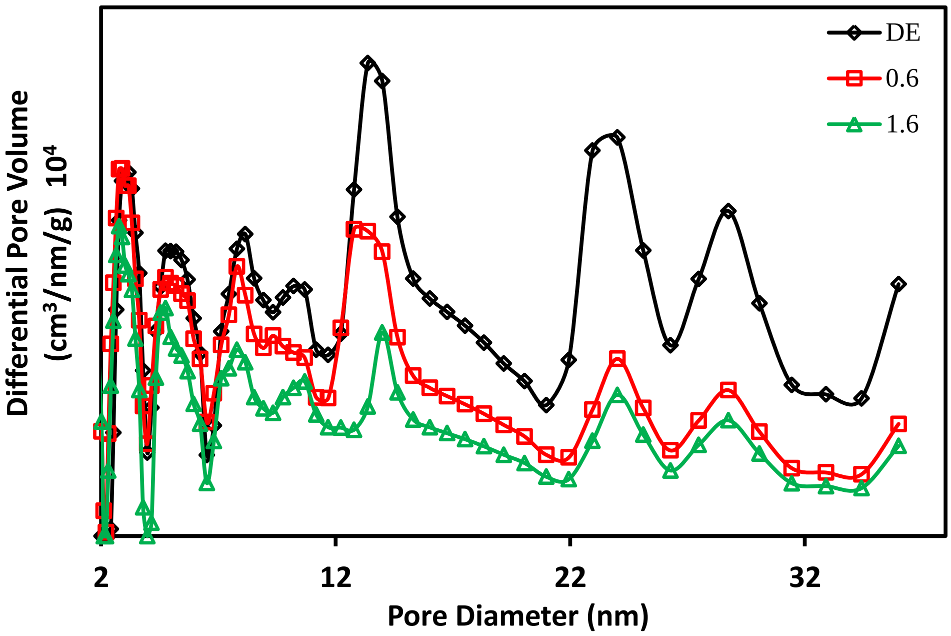

Figure 4.6. DFT pore size distribution curves for C16-TMS at different adsorbed hydrocarbon amounts in mg/m^2. Increased adsorbed amounts resulted in decreasing pore size intensities.

SEM images of untreated and treated DE particles are shown in Figure 4.7. Most of the diatom frustules were disk shaped with ordered micro- and nano-size pores and well defined dimensions, as shown in Figure 4.7 (a) and (b). The diameters of diatoms frustules were in the range of 10-20 µm. The SEM image of treated DE particles with 0.6 mg/m^2 adsorbed hydrocarbon amount for C18-TMS is shown in Figures 4.7 (c), and an image for C3-TMS treated DE are shown in Figures 4.7 (d) and (e). In the C3-TMS treated DE, most of the pores were partially or fully covered with the coupling agent (Figure 4.7 (e)); however, in C18-TMS treated DE, most of the pores appear unclogged. These findings were consistent with a measured decrease in BET specific surface areas from 24.1 mg/m^2 for untreated to 16.1 ± 0.4 and 17.0 ± 0.2 m^2/g for DE treated with C3-TMS and C18-TMS, respectively. These results were further supported by the pore size distributions (**Supporting Information**, Figure S4.2) which showed that the pore volume of the DE samples with 0.6 mg/m^2 of C3-TMS was smaller than those for C18-TMS.

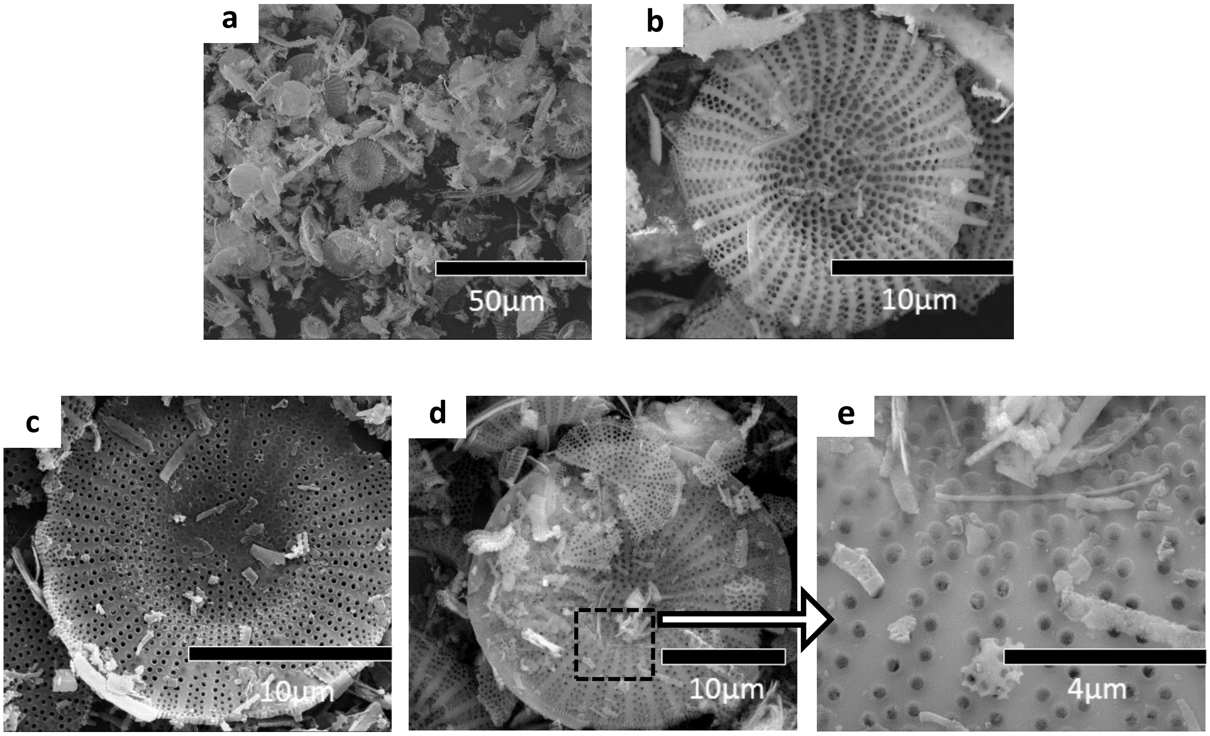

Figure 4.7. SEM images of untreated DE (a and b), treated DE with C18-TMS (c), and treated DE with C3-TMS (d and e) at the adsorbed hydrocarbon amount of 0.6 mg/m^2. In the C3-TMS sample, the pores appeared to be more filled than in the C18-TMS sample. There is possibility of formation of oligomers in C3-TMS samples on the surface at this adsorbed amount.

The crystallinity of the alkyl silane chains with increasing chain length were investigated with TMDSC. Thermograms of treated DE with 12 or more carbon atoms on the alkyl chains showed endothermic peaks upon heating (Figure 4.8). The melting temperatures and melting enthalpies increased with increased alkyl chain length.[65] The endothermic peaks of 2.2 mg/m^2 C12-TMS, C16-TMS, and C18-TMS treated DE were observed at 8.4, 38.0, and 49.2 °C, respectively. The melting enthalpies (ΔH_m) of all samples are summarized in Table S4.1 of **Supporting Information**. The melting temperatures of adsorbed coupling agents were lower than those for the corresponding bulk coupling agents. For comparison, the endothermic peaks for the bulk samples appeared at 13.7, 41.9, and 57.9 °C for self-condensed bulk C12-TMS, C16-TMS, and C18-TMS, respectively.[66] We also studied the TMDSC thermograms for different adsorbed hydrocarbon amounts of coupling agents. Samples with small adsorbed amounts of hydrocarbon did not show significant endothermic peaks. However, with increased adsorbed hydrocarbon amounts, the melting temperatures and the enthalpies increased toward those of the condensed bulk coupling agents. The results of the TMDSC scans for bulk and grafted C12-TMS on DE are shown in Figure S4.3 in the **Supporting Information**. Treated DE systems with C16-TMS and C18-TMS showed similar behavior (Figure S4.4 and S4.5 in the **Supporting Information)**.

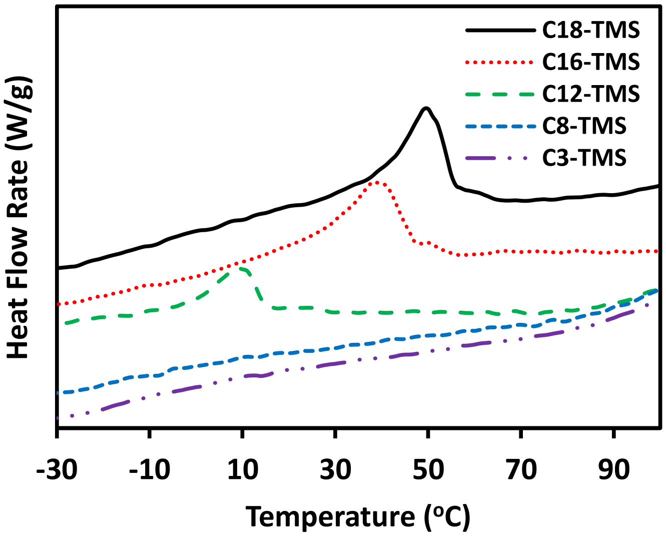

Figure 4.8. TMDSC thermograms for 2.2 mg/m^2 adsorbed hydrocarbon amount of DE with different chain length alkyltrimethoxysilanes. Only samples with 12 to 18 carbon atoms on the coupling agents showed endothermic melting peaks.

4.4.2. Wettability of treated and untreated DE polyurethane coatings

Water contact angles of polyurethane coatings with untreated and treated DE with different adsorbed hydrocarbon amounts (0.6, 1.6, 2.2, and 3.4 mg/m^2) and different chain lengths of alkyltrimethoxysilanes are shown in Figure 4.9. The DE-containing coating, without any alkyltrimethoxysilane was hydrophilic with a water contact angle around 88°. The water contact angles of coatings prepared with treated DE were larger and showed hydrophobic or superhydrophobic properties. The water contact angles of samples with 0.6 mg/m^2 adsorbed hydrocarbon amounts for C8 to C18 were roughly within experimental error of each other. With increased adsorbed hydrocarbon amounts up to 1.6 mg/m^2, the water contact angles increased compared to the 0.6 mg/m^2 sample. Samples with C12-TMS and C16-TMS entered the superhydrophobic region. With increased adsorbed hydrocarbon amounts of 2.2 and 3.4 mg/m^2, coatings with treated samples with 12 or more carbon at in the chains were superhydrophobic and similar. Samples treated with C3-TMS and C8-TMS were only hydrophobic at all adsorbed hydrocarbon amounts. In general, the water contact angles increased with chain lengths up to C12-TMS and then remained almost constant, up to n = 18, corresponding to the longest alkyltrimethoxysilane used in this study. It is possible that the samples with small adsorbed hydrocarbon amounts had greater error because at those small adsorbed amounts the coupling agents were not uniformly adsorbed.

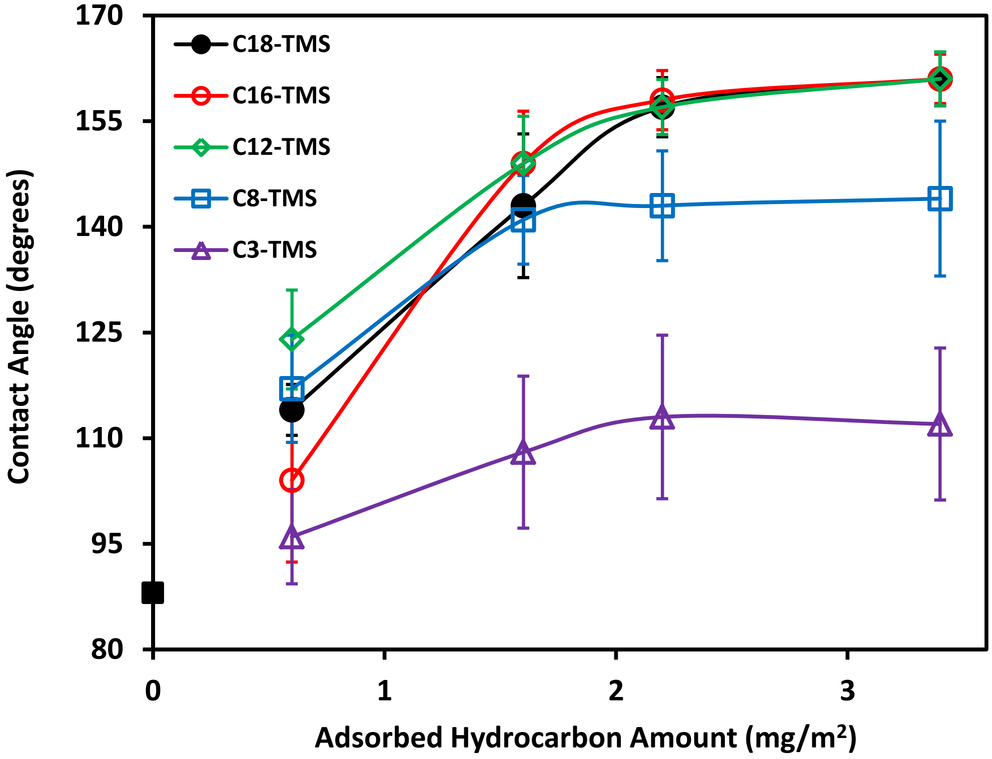

Figure 4.9. Water contact angles of untreated DE (filled square), and treated DE coatings (50% treated DE particle loadings with polyurethane binder) with different chain length alkyltrimethoxysilanes and adsorbed hydrocarbon amounts 0.6, 1.6, 2.2, and 3.4 mg/m^2. Samples containing treated DE with larger adsorbed amounts and longer

alkyltrimethoxysilane chains were superhydrophobic. The lines are drawn to guide the eye.

The time dependent spreading of water droplets on the DE-containing surfaces were also studied. Coatings, including untreated DE, had water contact angles around 82° immediately after deposition of the water on the surface. Within a minute, the contact angle decreased to 27° and a few seconds later the water droplet was completely spread on the surface. Therefore, an accurate measurement of the contact angle of untreated DE was not possible after 1 min. Once DE was grafted with C12-TMS and longer alkyltrimethoxysilanes, the water contact angles did not change significantly in 10 min. However, the contact angles for coatings with C3-TMS and C8-TMS remained almost constant only for 2 min and then started to decrease by around 10 to 15° from 114° and 133°, respectively. The time dependent contact angle results are presented in the Figure S4.6 of the **Supporting Information**.

The water contact angles of the polyurethane coatings containing different amounts of treated DE particles with 3.4 mg/m^2 adsorbed hydrocarbon amounts of C12-TMS are shown in Figure 4.10. Polyurethane coatings with different mass fractions of treated DE were prepared in order to study the effect of the amount of treated DE particle loadings. The contact angles of the films increased with increased particle loadings of treated DE particles and reached superhydrophobicity at around 30% treated DE particle loadings. The contact angles of the coatings then remained constant for samples with up to 50% of treated DE particles and then decreased slightly with the mass fraction of treated DE.

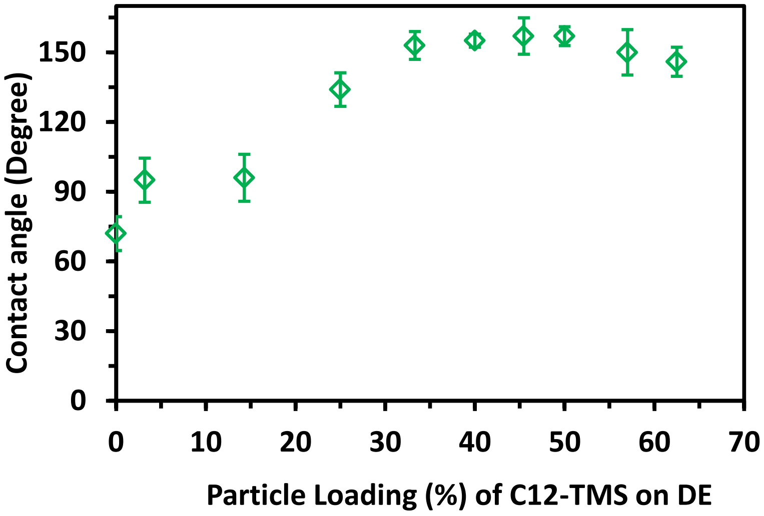

Figure 4.10. Contact angles of polyurethane coatings with 3.4 mg/m^2 C12-TMS treated DE as a function of the particle loading. Samples with at least 30% by mass of treated DE showed superhydrophobicity.

To study the correlation between the surface morphology and water contact angles of the polyurethane coatings, SEM images were taken. The SEM images of polyurethane coatings with different mass fractions of 3.4 mg/m^2 C12-TMS treated DE with a water droplet picture on each surface, as an inset, are shown in Figure 4.11. Note that the magnification of these pictures is much less than that in Figure 4.7 to show a more broad-based particle distribution rather than the details of the particles. The surface of the polyurethane, Figure 4.11 (a), coating without treated DE was very smooth and featureless, as was expected. With addition of treated DE, the coating surfaces displayed micro-roughness with even distributions of treated DE particles. Figure 4.11 (b) and (c) clearly show an enhancement in the surface roughness (particle loading) and contact angle with increasing the fraction of treated DE. The surface roughness of samples with larger amounts of treated DE particles (more than 50%) decreased, leading to a reduction in contact angle, as shown in Figure 4.11(d). These observations were consistent with previous studies.[67-68]

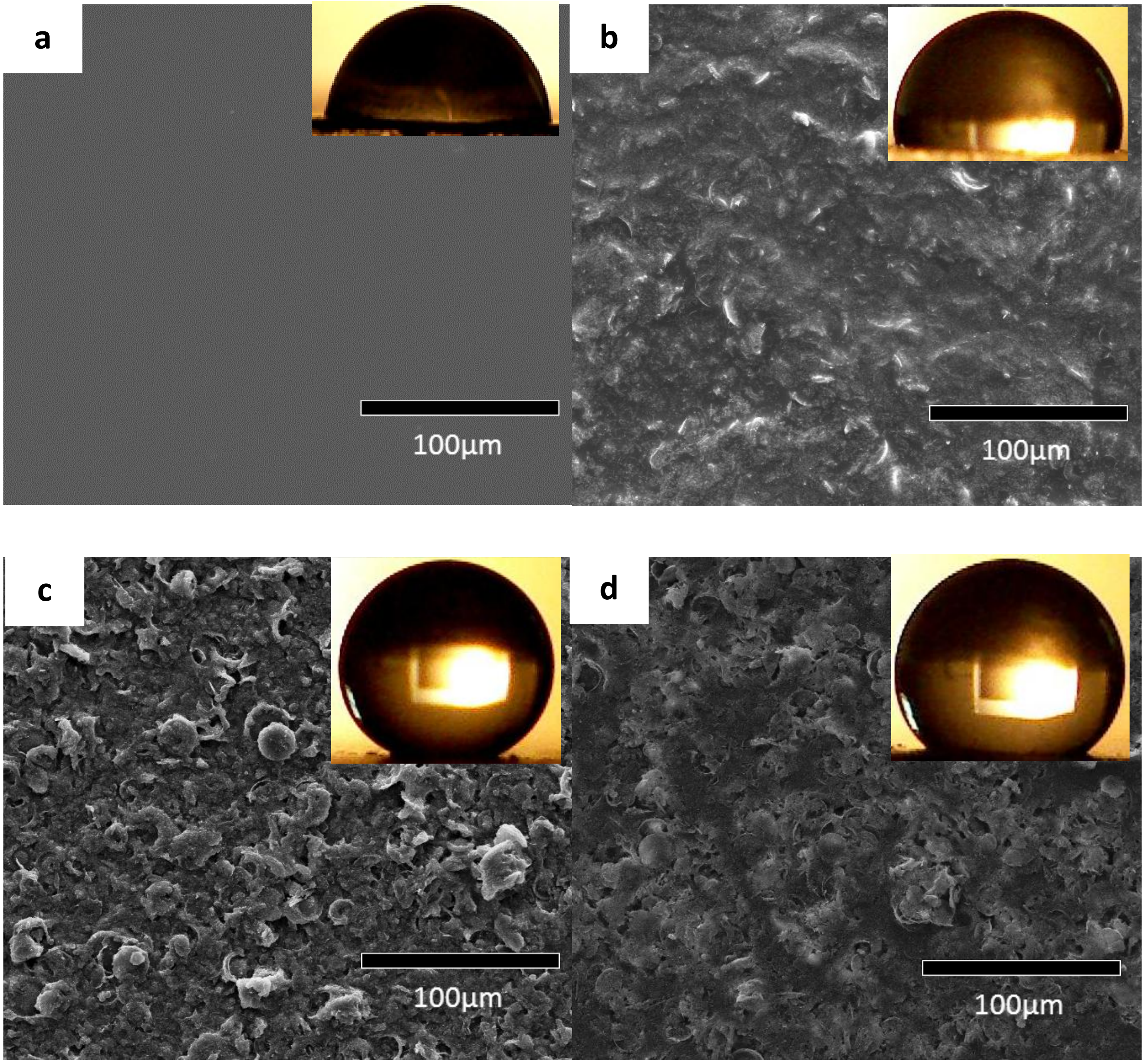

Figure 4.11. SEM images and water droplet pictures (insets) of polyurethane coatings with different particle loadings of 3.4 mg/m^2 C12-TMS treated DE for a) polyurethane binder alone, b) 14.3%, c) 40%, and d) 62.5% -treated DE. Roughness and water contact angles of the coatings increased up to around 50% of treated DE and then decreased slightly. The scale bars represent 100 µm.

4.5. DISCUSSION

4.5.1. FTIR and TMDSC results showed ordered structure for longer chains with larger adsorbed amount of coupling agent

FTIR spectroscopy provided information on the presence and structure of alkyltrimethoxysilane with different chain lengths grafted to the DE particles.[69-72] Weak van der Waals interactions played an important role in formation of ordered structures of alkyltrimethoxysilanes on the surface of DE. The FTIR results showed that the vibrational frequencies of symmetric and asymmetric CH_2 resonances decreased as the chain lengths of alkyltrimethoxysilane increased (Figure 4.3). The CH_2 stretching frequencies varied with the alkyl chains' environment and conformations (trans/gauche). In crystalline n-alkanes, with mostly trans conformers, symmetric and asymmetric stretching frequencies lie around 2850 and 2916 cm^{-1}, respectively.[63] The higher frequencies observed for samples with shorter chains indicated the presence of a larger number of gauche conformers. The presence of more gauche conformers in shorter chains is due to their more amorphous nature, as compared to longer chains. With increased chain-length of the alkyltrimethoxysilane (≥ C12), more ordered structures were formed on the surface. For adsorbed coupling agents with longer chain length hydrocarbons, the chains were more ordered at larger adsorbed amounts. At small adsorbed amounts, CH_2 stretching frequencies were similar to liquid alkane CH_2 stretching frequencies, indicating that molecules were more disorganized. With increasing adsorbed amounts, CH_2 stretching frequencies also moved to a lower frequency (see Figures 4.4 and S4.1). At larger adsorbed hydrocarbon amounts, more ordered structures with mainly trans-trans conformations were formed and the FTIR stretching frequencies were similar to those for crystalline hydrocarbons.

The change in the conformational order with increased adsorbed amounts were confirmed with TMDSC (Figures S4.3, 4.4 and 4.5), where the areas under the endothermic peaks and melting temperatures increased with increased adsorbed amounts, approaching those of the bulk condensed coupling agent. At small adsorbed amounts (0.6 mg/m^2), the TMDSC thermograms did not show any melting due to the disordered structures of the CH_2 hydrocarbon chains likely resulting from the relatively large distances between chains.

Self-condensed bulk and adsorbed longer chain coupling agents had higher melting temperatures than their monomeric counterparts. Melting requires the breaking of the van der Waals interactions between alkyl chains.[65] For the monomer, the entropy increase upon melting was greater than that in the condensed or adsorbed samples because of the larger translational entropy for monomers. Immobilization of the chains in either bulk-condensed or adsorbed polymers resulted in lower translational entropy and higher melting temperatures.

A summary of the melting temperatures for different adsorbed amounts, monomer, and bulk condensed samples is given in Table S4.2 of the **Supporting Information**. For simplicity, a subset of the data is compared in Figure 4.12 for only the 2.2 mg/m^2 adsorbed, bulk-condensed, and monomer long chain alkyltrimethoxysilanes. As shown in Figure 4.8 and Table S4.1, melting temperatures and melting enthalpies increased with alkyl chain length.[73] The increase in melting temperature with alkyl chain length is a well-known phenomenon in homologous series. As an example, with varying alkyl side chains length (12, 16, and 18) of poly(alkyl methacrylate)s, the polymer melting points were -33.4, 20.8, and 35.7 °C, respectively.[74] This effect has been attributed to the decrease in the number of chain ends inside a crystal.[75] The similarity of the higher melting temperatures for the bulk-condensed and adsorbed species were likely due to similarities in the structures of the crystalline chains in both of them. The condensation of the silanols may allow similar proximity of the hydrocarbon chains in the coupling agents in either state.

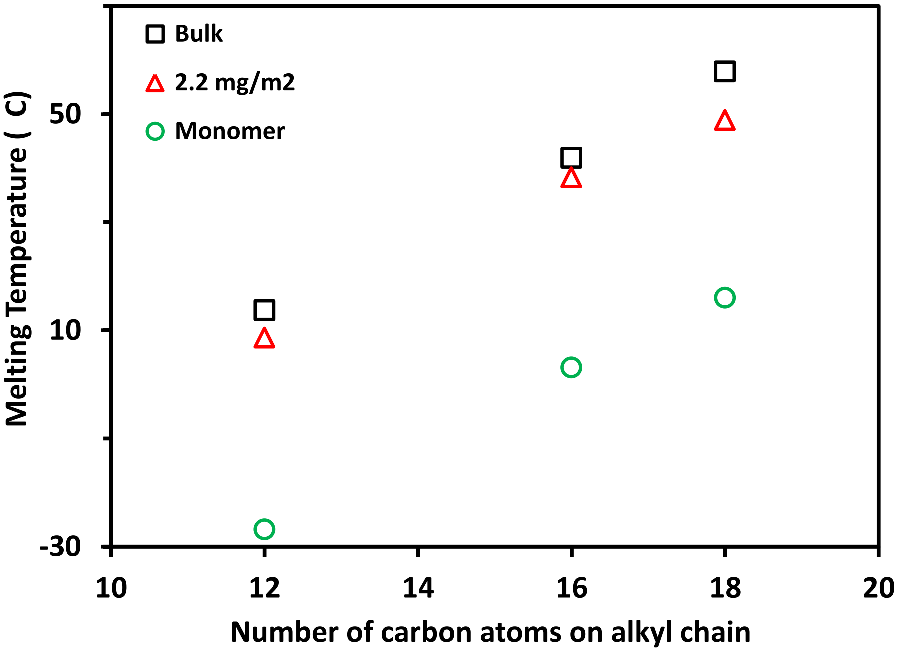

Figure 4.12. Melting temperatures of the bulk-condensed (□), 2.2 mg/m^2 adsorbed hydrocarbon on the DE surface (**Δ**), and monomers of the alkyltrimethoxysilane (○) as a function of the chain length. The results for the other adsorbed amounts are given in the **Supporting Information**.

The BET surface area and pore size distribution results were in agreement with the findings from FTIR and TMDSC. At large adsorbed hydrocarbon amounts, hydrocarbon chains formed a dense layer bonded chains, while at small adsorbed hydrocarbon amounts, the chains had a larger surface area per molecule. This lead to a larger specific surface area compared to the samples with larger adsorbed hydrocarbon amounts (Figure 4.5). One implication of the lack of crystallinity at small adsorbed amounts was that the longer chain coupling agents did not appear to form patchwise aggregates on the surface. With increased numbers of hydrocarbon chains per nm^2, the area per molecule on the surface and the specific surface area decreased. At the same time, the volumes of the pores decreased as the adsorbed hydrocarbon amounts increased (Figure 4.6). These observations suggested that the alkyltrimethoxysilane coated the surface of the DE particles and decreased their porosity. Decreasing surface areas and pore volumes with increased adsorbed amounts were observed in previous studies of 3-aminopropyltriethoxysilane on montmorillonite as well.[76]

Diatom frustules were decorated with unique patterns of nano features,[25] as observed in Figure 4.7, which can be affected with treatment of alkylsilanes. These features include pores, ridges, spikes, channels, and spines. After modifying the DE particles with C3-TMS and C18-TMS, we observed some topographical changes compared to bare DE, as shown in Figure 4.7(e). As was expected, at the same adsorbed hydrocarbon amount, shorter chains had many more chains on the surface compared to longer chains. These shorter chains also had a much larger concentration of silanol groups in solution, therefore, it was more likely that they formed oligomers in solution due to self-condensation. Consequently, oligomers could cover the mesoporous structures and possibly the larger pores too. In other words, at the same adsorbed hydrocarbon amount, shorter chains should have covered a larger surface area of DE relative to longer chains.

This effect was observed as a decrease in the surface area and pore size of 0.6 mg/m^2 adsorbed C3-TMS compared to C18-TMS (Figure S4.2). This observation was in good agreement with the SEM images, where the silane chains appeared to fill the pores.

4.5.2. Water contact angles increased with increasing chain lengths and adsorbed amounts of silane coupling agents

The structure of long chain alkyltrimethoxysilanes, converted the DE into a superhydrophobic material after a minimum adsorbed hydrocarbon amount. DE is a natural source of silicon dioxide and composed of large number of free silanol groups.[77-78] These silanol groups make DE a hydrophilic material. With the treatment of the DE surface with alkyltrimethoxysilanes, the number of free silanol groups decreased and resulted in larger contact angles.[77, 79] As shown in Figure 4.9, as treated DE materials became superhydrophobic when the alkyl chain length was ≥ C12 and the adsorbed hydrocarbon amount was ≥ 2.2 mg/m^2. Several studies,[72, 80] have shown that as the length of the alkyl chain decreases, the structure of the grafted chains became more disordered. This was reflected by a smaller water contact angle. Previous studies showed perpendicular orientation of long alkyl chains at large adsorbed amounts[45, 80-82] with low surface energy around 20 mN/m.[80] This indicates that well aligned, long alkyl chains (n ≥ 12) can repel the water further from the surface due to their low surface energies. In this study, superhydrophobic surfaces were formed from DE, due to the ordered packing structures as discussed in conjunction with the FTIR and TMDSC results.

Samples with small adsorbed amounts of silane, i.e., 0.6 mg/m^2, did not reach superhydrophobicity *at any chain length*, as Figure 4.9 shows. To understand the reason behind this observation, we calculated the number of chains per nm^2 of DE particles

(**Supporting Information** Table S4.3). At the same adsorbed hydrocarbon amount, number of molecules on the surface was smaller for longer chain length silanes. The cross-section of the long hydrocarbon chains is 0.19 – 0.24 nm^2 per molecule,[52] when the molecules are closely packed.[58, 83] This means that the closely packed surface has around 4-5 long hydrocarbon molecules per nm^2. Of course, this is an idealized estimate. Therefore, longer chain length silane coupling agents did not have a well-ordered structure at 0.6 mg/m^2. In other words, those with longer chains with 0.6 mg/m^2 are not closely packed and the water droplets can penetrate and reach the surface. This leads to only a hydrophobic coating with $C \geq 12$ silane coupling agents. The treated DE samples with 0.6 mg/m^2 and C3-TMS has larger number of chains per nm^2 than a hypothetical closely packed system. However, since the chains are short, the surface energy is not small enough to repel the water enough to reach superhydrophobicity. At this adsorbed amount, the contact angles of the treated samples with longer chains are larger than those of the smaller chains, because the longer chains are able to shield the hydrophilic groups on the DE surface, although they might not all be directly grafted to these groups as they likely adsorb as oligomers.

The number of alkyltrimethoxysilane chains per nm^2 has a direct relationship to the contact angle measurement of the surface as shown in Figure 4.13. As grafted density (molecules/surface area) increased, the contact angles increased for all sets of coupling agents. For longer chain length coupling agents, the contact angles increased steeply and reached superhydrophobicity at small grafted densities. However, the increases in the contact angles were gradual with the grafting density for shorter chains. Those surfaces never became superhydrophobic even at large grafted densities. This distinction, based on chain length, was due to the formation of more well-packed structures on the surface and also the lower surface energy for the larger chain length species.

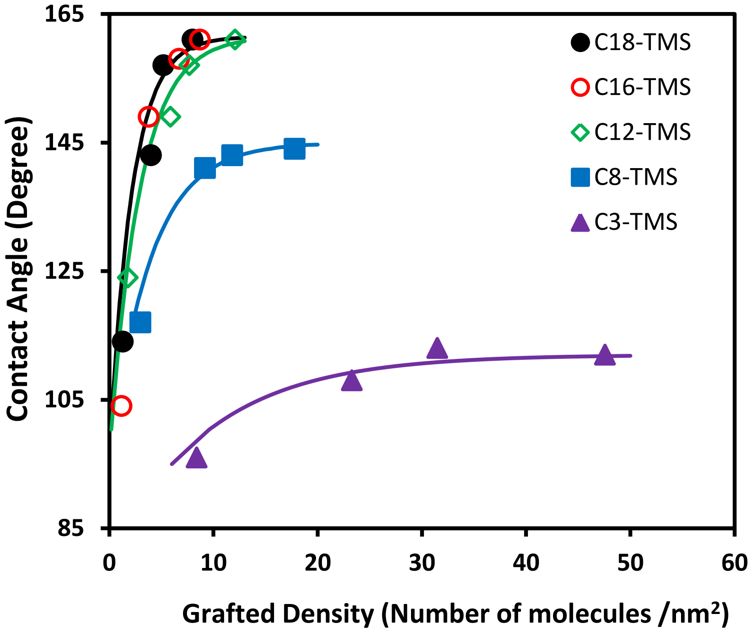

Figure 4.13. Contact angles as function of grafted densities for different chain length alkyltrimethoxysilanes.

It should be noted that the adsorbed hydrocarbon amount does play an important role in the surface behavior of DE. At one extreme, short chains did not facilitate superhydrophobicity regardless of the adsorbed hydrocarbon amount. At the other extreme, a long chain coupling agent, C12-TMS, (Figure 4.13) could cause superhydrophobicity, but only at higher grafted densities than the other long chains studied. At adsorbed hydrocarbon amounts greater than, say 2 mg/m^2, there was no difference in the superhydrophobicity of C12, C16 and C18. In other words, from Figure 4.9, superhydrobicity seemed to be controlled by the adsorbed hydrocarbon amount.

Superhydrophobicity occurs due to the combination of roughness, which may manifest itself as porosity, and low surface energy. The surface morphology of polyurethane coatings changed with the mass fraction of treated DE particles as reflected in the SEM images in Figure 4.11. The contact angle also increased with increased particle loading of treated DE (Figure 4.10). This showed that the increase in the surface roughness/porosity increased the contact angle[67, 84] due to the treated-DE particles coming to the surface of the coatings. The increases in the contact angles of the surfaces with the amount of DE were observed up to 50% particle loadings. The contact angle decreased after this point due to decrease in the roughness of the surface (Figure 4.11(d)). Decreasing the surface roughness caused a decrease in the air volume fraction beneath the water droplet and led to a decrease in the contact angle of the surface.[67, 84] In contrast, with increasing *fluorosilane* treated DE particle loading, the contact angles did not decrease at larger particle loadings.[50] This is due to the lower surface energy of fluorosilane coupling agent compared to the non-fluorosilane.

4.6. CONCLUSIONS

The surface properties of DE with grafted alkyltrimethoxysilane [$CH_3(CH_2)_{n-1}Si(OCH_3)_3$, n = 3, 8, 12, 16, and 18] were studied with a focus on the effect of the chain length on the superhydrophobic behavior of the DE. The results of TGA, FTIR, BET, and contact angle measurements confirmed that alkyltrimethoxysilanes with different chain lengths were successfully grafted onto hydrophilic DE particles by reacting with silanol groups of the DE with the silane. The surface wettability was estimated using water contact angle measurements. It was found that, at similar adsorbed hydrocarbon amounts, the contact angles increased as the alkyl chain lengths of grafted alkyltrimethoxysilanes increased and reached a plateau with chains of C12 or greater. Superhydrophobicity occurred with adsorbed hydrocarbon amounts of about 2 mg/m^2 or more of long alkyl chains, such as dodecyltrimethoxysilane, which seemed to correlate with the ability of the alkylsilanes to crystallize. We also showed that the longer chains were packed with a higher order, and the presence of ordered structure are critical in the formation of superhydrophobic DE particles. After a minimum chain length, C12 in this case, superhydrophobicity was a function of the amount of adsorbed hydrocarbon, but this was not the case for shorter chains (C3 to C8).

Surface roughness, including pores, also plays an important role in the formation of superhydrophobicity. When a sufficient adsorbed hydrocarbon amount (≥ 2.2 mg/m^2) was present, with increased amounts of treated DE ($\geq$ C12-TMS) particles, the contact angle increased up to 50% of loading (increasing of surface roughness) and the contact angle decreased with mass fraction of treated DE particles (decreasing of trapped air volume fraction). SEM images at different mass fractions further confirmed increased roughness up to 50% and then decreased roughness due to the covering up of open spaces with the particles.

4.7. ACKNOWLEDGEMENTS

The authors acknowledge the financial support of the Dry Surface Coating Guthrie, OK and the Oklahoma State University.

4.8. REFERENCES

(1) Cao, L.; Jones, A. K.; Sikka, V. K.; Wu, J.; Gao, D. *Langmuir* **2009**, *25*, 12444.

(2) Zhang, J.; Pu, G.; Severtson, S. J. *ACS Appl. Mater. Interfaces* **2010**, *2,* 2880.

(3) Fürstner, R.; Barthlott, W.; Neinhuis, C.; Walzel, P. *Langmuir* **2005**, *21*, 956.

(4) Wang, H.; Tang, L.; Wu, X.; Dai, W.; Qiu, Y. *Appl. Surf. Sci.* **2007**, *253*, 8818.

(5) Loo, C.-Y.; Young, P. M.; Lee, W.-H.; Cavaliere, R.; Whitchurch, C. B.; Rohanizadeh, R. *Acta Biomater.* **2012**, *8*, 1881.

(6) Sun, T.; Tan, H.; Han, D.; Fu, Q.; Jiang, L. *Small* **2005**, *1*, 959.

(7) Hou, X.; Wang, X.; Zhu, Q.; Bao, J.; Mao, C.; Jiang, L.; Shen, J. *Colloids Surf., B* **2010**, *80*, 247.

(8) Gao, L.; McCarthy, T. J. *J. Am. Chem. Soc.* **2006**, *128*, 9052.

(9) Hejazi, I.; Hajalizadeh, B.; Seyfi, J.; Sadeghi, G. M. M.; Jafari, S.-H.; Khonakdar, H. A. *Appl. Surf. Sci.* **2014**, *293*, 116.

(10) Shirtcliffe, N. J.; McHale, G.; Atherton, S.; Newton, M. I. *Adv. Colloid Interface Sci.* **2010**, *161*, 124.

(11) Korunic, Z. *J. Stored Prod. Res.* **1998**, *34*, 87.

(12) Crawford, S. A.; Higgins, M. J.; Mulvaney, P.; Wetherbee, R. *J. Phycol.* **2001**, *37*, 543.

(13) Fuhrmann, T.; Landwehr, S.; El Rharbi-Kucki, M.; Sumper, M. *Appl. Phys. B* **2004**, *78*, 257.

(14) Gordon, R.; Losic, D.; Tiffany, M. A.; Nagy, S. S.; Sterrenburg, F. A. S. *Trends Biotechnol.* **2009**, *27*, 116.

(15) Round, F. E.; Crawford, R. M.; Mann, D. G. *Diatoms: biology and morphology of the genera*; Cambridge University Press: Cambridge, 1990.

(16) Tu, K. L.; Sharon, V. R.; Fung, M. A. *J. Cutan. Pathol.* **2011**, *38*, 762.

(17) Lebeau, T.; Robert, J.-M. *Appl. Microbiol. Biotechnol.* **2003**, *60*, 612.

(18) Tsai, W.-T.; Lai, C.-W.; Hsien, K.-J. *J. Colloid Interface Sci.* **2006**, *297*, 749.

(19) Bariana, M.; Aw, M. S.; Kurkuri, M.; Losic, D. *Int. J. Pharm.* **2013**, *443*, 230.

(20) Polizos, G.; Winter, K.; Lance, M. J.; Meyer, H. M.; Armstrong, B. L.; Schaeffer, D. A.; Simpson, J. T.; Hunter, S. R.; Datskos, P. G. *Appl. Surf. Sci.* **2014**, *292*, 563.

(21) Lopez, P. J.; Desclés, J.; Allen, A. E.; Bowler, C. *Curr. Opin. Biotechnol.* **2005**, *16*, 180.

(22) van Garderen, N.; Clemens, F. J.; Kaufmann, J.; Urbanek, M.; Binkowski, M.; Graule, T.; Aneziris, C. G. *Microporous Mesoporous Mater.* **2012**, *151*, 255.

(23) Ediz, N.; Bentli, İ.; Tatar, İ. *Int. J. Miner. Process.* **2010**, *94*, 129.

(24) Losic, D.; Rosengarten, G.; Mitchell, J. G.; Voelcker, N. H. *J. Nanosci. Nanotechnol.* **2006**, *6*, 982.

(25) Losic, D.; Triani, G.; Evans, P. J.; Atanacio, A.; Mitchell, J. G.; Voelcker, N. H. *J. Mater. Chem.* **2006**, *16*, 4029.

(26) Yuan, P.; Liu, D.; Tan, D.-Y.; Liu, K.-K.; Yu, H.-G.; Zhong, Y.-H.; Yuan, A.-H.; Yu, W.-B.; He, H.-P. *Microporous Mesoporous Mater.* **2013**, *170*, 9.

(27) Lettieri, S.; Setaro, A.; De Stefano, L.; De Stefano, M.; Maddalena, P. *Adv. Funct. Mater.* **2008**, *18*, 1257.

(28) Fowler, C. E.; Buchber, C.; Lebeau, B.; Patarin, J.; Delacôte, C.; Walcarius, A. *Appl. Surf. Sci.* **2007**, *253*, 5485.

(29) Bello, O. S.; Adegoke, K. A.; Oyewole, R. O. *Sep. Sci. Technol.* **2014**, *49*, 1787.

(30) Al Bakain, R. Z.; Abu-Zurayk, R. A.; Hamadneh, I.; Khalili, F. I.; Al-Dujaili, A. H. *Desalin. Water Treat.* **2014**, 1.

(31) Zidan, N. *Acta Phytopathol. Entomol. Hung.* **2014**, *49*, 117.

(32) Szczech, J. R.; Jin, S. *J. Solid State Chem.* **2008**, *181*, 1565.

(33) Arias, J. L. d. O.; Rombaldi, C.; Caldas, S. S.; Primel, E. G. *J. Chromatogr. A* **2014**, *1360*, 66.

(34) Poulsen, N.; Berne, C.; Spain, J.; Kröger, N. *Angew. Chem. Int. Ed.* **2007**, *46*, 1843.

(35) Milović, M.; Simović, S.; Lošić, D.; Dashevskiy, A.; Ibrić, S. *Eur. J. Pharm. Sci.* **2014**, *63*, 226.

(36) Berendsen, G. E.; Galan, L. d. *J. Liq. Chromatogr.* **1978**, *1*, 561.

(37) Buszewski, B.; Jezierska, M.; Wełniak, M.; Berek, D. *J. High. Resolut. Chromatogr.* **1998**, *21*, 267.

(38) García, N.; Benito, E.; Guzmán, J.; Tiemblo, P. *J. Am. Chem. Soc.* **2007**, *129*, 5052.

(39) Taguchi, A.; Schüth, F. *Microporous Mesoporous Mater.* **2005**, *77*, 1.

(40) Impens, N. R. E. N.; van der Voort, P.; Vansant, E. F. *Microporous Mesoporous Mater.* **1999**, *28*, 217.

(41) Wang, J.; Mao, G.; Ober, C. K.; Kramer, E. J. *Macromolecules* **1997**, *30*, 1906.

(42) Kempe, M. D.; Kornfield, J. A.; Ober, C. K.; Smith, S. D. *Macromolecules* **2004**, *37*, 3569.

(43) Honda, K.; Morita, M.; Sakata, O.; Sasaki, S.; Takahara, A. *Macromolecules* **2009**, *43*, 454.

(44) Sohn, E.-H.; Kim, J.; Kim, B. G.; Kang, J. I.; Chung, J.-S.; Ahn, J.; Yoon, J.; Lee, J.-C. *Colloids Surf., B* **2010**, *77*, 191.

(45) Honda, K.; Morita, M.; Otsuka, H.; Takahara, A. *Macromolecules* **2005**, *38*, 5699.

(46) W. A, Z. In *Contact Angle, Wettability, and Adhesion*; American Chemical Society: Washington, D.C., 1964; Vol. 43, p 1.

(47) Hare, E. F.; Shafrin, E. G.; Zisman, W. A. *J. Phys. Chem.* **1954**, *58*, 236.

(48) Oliveira, N. M.; Reis, R. L.; Mano, J. F. *ACS Appl. Mater. Interfaces* **2013**, *5*, 4202.

(49) Sedai, B. R.; Khatiwada, B. K.; Mortazavian, H.; Blum, F. D. *Appl. Surf. Sci.* **2016**, *386*, 178.

(50) Perera, H. J.; Khatiwada, B. K.; Paul, A.; Mortazavian, H.; Blum, F. D. *J. Appl. Polym. Sci.* **2016**, *133*, 44072.

(51) Blum, F. D.; Meesiri, W.; Kang, H.-J.; Gambogi, J. E. *J. Adhes. Sci. Technol.* **1991**, *5*, 479.

(52) Jo, H.; Blum, F. D. *Langmuir* **1999**, *15*, 2444.

(53) Lowell, S.; Shields, J. E. *Powder Surface Area and Porosity*; 2nd ed.; Chapman and Hall: New York, NY, 1984.

(54) Seaton, N. A.; Walton, J. P. R. B.; quirke, N. *Carbon* **1989**, *27*, 853.

(55) Stalder, A. F.; Melchior, T.; Müller, M.; Sage, D.; Blu, T.; Unser, M. *Colloids Surf., A* **2010**, *364*, 72.

(56) Rotenberg, Y.; Boruvka, L.; Neumann, A. W. *J. Colloid Interface Sci.* **1983**, *93*, 169.

(57) Williams, D. L.; Kuhn, A. T.; Amann, M. A.; Hausinger, M. B.; Konarik, M. M.; Nesselrode, E. I. *Galvanotechnik* **2010**, *101*, 2502.

(58) Parikh, A.; Schivley, M.; Koo, E.; Seshadri, K.; Aurentz, D.; Mueller, K.; Allara, D. *J. Am. Chem. Soc.* **1997**, *119*, 3135.

(59) Chaisena, A.; Rangsriwatananon, K. *Suranaree J. Sci Technol* **2004**, *11*, 289.

(60) Yuan, P.; Wu, D. Q.; He, H. P.; Lin, Z. Y. *Appl. Surf. Sci.* **2004**, *227*, 30.

(61) Akhtar, F.; Rehman, Y.; Bergström, L. *Powder Technol.* **2010**, *201*, 253.

(62) Zhang, T.; Xu, G.; Puckette, J.; Blum, F. D. *J. Phys. Chem. C* **2012**, *116*, 11626.

(63) Parikh, A. N.; Liedberg, B.; Atre, S. V.; Ho, M.; Allara, D. L. *J. Phys. Chem.* **1995**, *99*, 9996.

(64) Doadrio, J. C.; Sousa, E. M.; Izquierdo-Barba, I.; Doadrio, A. L.; Perez-Pariente, J.; Vallet-Regí, M. *J. Mater. Chem.* **2006**, *16*, 462.

(65) Marques, E. F.; Brito, R. O.; Wang, Y.; Silva, B. F. B. *J. Colloid Interface Sci.* **2006**, *294*, 240.

(66) Dong, A. W.; Fong, C.; Waddington, L. J.; Hill, A. J.; Boyd, B. J.; Drummond, C. J. *Physical Chemistry Chemical Physics* **2015**, *17*, 276.

(67) Li, Y.; Huang, X. J.; Heo, S. H.; Li, C. C.; Choi, Y. K.; Cai, W. P.; Cho, S. O. *Langmuir* **2006**, *23*, 2169.

(68) Karmouch, R.; Ross, G. G. *Appl. Surf. Sci.* **2010**, *257*, 665.

(69) Vaia, R. A.; Teukolsky, R. K.; Giannelis, E. P. *Chem. Mater.* **1994**, *6*, 1017.

(70) Kojio, K.; Takahara, A.; Kajiyama, T. *Langmuir* **2000**, *16*, 9314.

(71) Park, J.-S.; Smith, A. C.; Lee, T. R. *Langmuir* **2004**, *20*, 5829.

(72) Spori, D. M.; Venkataraman, N. V.; Tosatti, S. G. P.; Durmaz, F.; Spencer, N. D.; Zürcher, S. *Langmuir* **2007**, *23*, 8053.

(73) Xu, F.; Matsubara, S.; Matsumoto, K.; Hagiwara, R. *J. Fluorine Chem.* **2012**, *135*, 344.

(74) Okouchi, M.; Yamaji, Y.; Yamauchi, K. *Macromolecules* **2006**, *39*, 1156.

(75) Mandelkern, L. *Crystallization of polymers*; McGraw-Hill New York: New York, NY, 1964; Vol. 38.

(76) Gopinath, S.; Sugunan, S. *Appl. Clay Sci.* **2007**, *35*, 67.

(77) Yuan, P.; Liu, D.; Tan, D.-Y.; Liu, K.-K.; Yu, H.-G.; Zhong, Y.-H.; Yuan, A.-H.; Yu, W.-B.; He, H.-P. *Microporous Mesoporous Mater.* **2013**, *170*, 9.

(78) Krisanangkura, P.; Packard, A. M.; Burgher, J.; Blum, F. D. *J. Polym. Sci., Part B: Polym. Phys.* **2010**, *48*, 1911.

(79) Vrancken, K. C.; De Coster, L.; Van Der Voort, P.; Grobet, P. J.; Vansant, E. F. *J. Colloid Interface Sci.* **1995**, *170*, 71.

(80) Sohn, E.-H.; Ahn, J.; Kim, B. G.; Lee, J.-C. *Langmuir* **2010**, *27*, 1811.

(81) Kim, B. G.; Sohn, E.-H.; Lee, J.-C. *Macromol. Chem. Phys.* **2007**, *208*, 1011.

(82) Sohn, E.-H.; Kim, B. G.; Chung, J.-S.; Lee, J.-C. *J. Colloid Interface Sci.* **2010**, *343*, 115.

(83) Petty, M. C. *Langmuir-Blodgett Films*; Cambridge University Press: New York, NY, 1996.

(84) Lin, Y.; Ehlert, G. J.; Bukowsky, C.; Sodano, H. A. *ACS Appl. Mater. Interfaces* **2011**, *3*, 2200

4.9. SUPORTING INFORMATION

S4.1. Surface characterization

The CH_2 stretching frequencies of C12-TMS as a function of adsorbed hydrocarbon amount is shown in Figure S4.1. The CH_2 symmetric and asymmetric stretching frequencies moved to lower frequency (indicating that the chains were more ordered), with increased adsorbed hydrocarbon amounts of coupling agents. The vertical scales and positions were adjusted for clarity

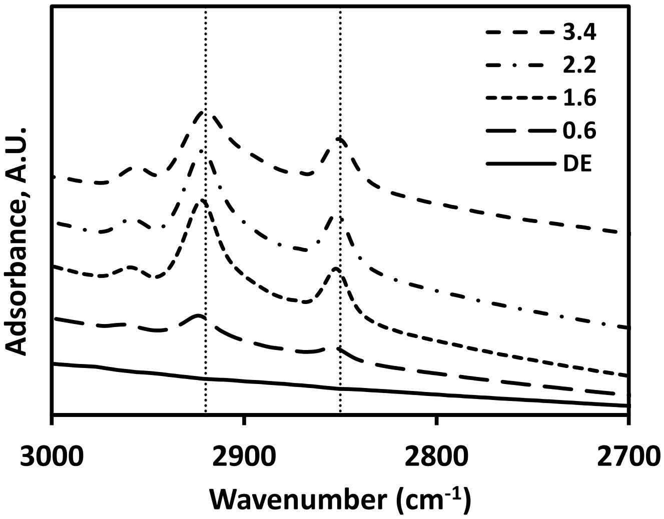

Figure S4.1. Symmetric and asymmetric CH_2 stretching frequencies of C12-TMS as a function of adsorbed hydrocarbon amount.

The pore size distribution of C18-TMS and C3-TMS treated DE with 0.6 mg/m^2 adsorbed hydrocarbon amounts is shown in Figure S4.2. Addition of 0.6 mg/m^2 C3-TMS caused a decrease in the pore volume compared to C18-TMS, due to the formation of more oligomers because at the same adsorbed hydrocarbon amount, there were more silane molecules in the C3-TMS.

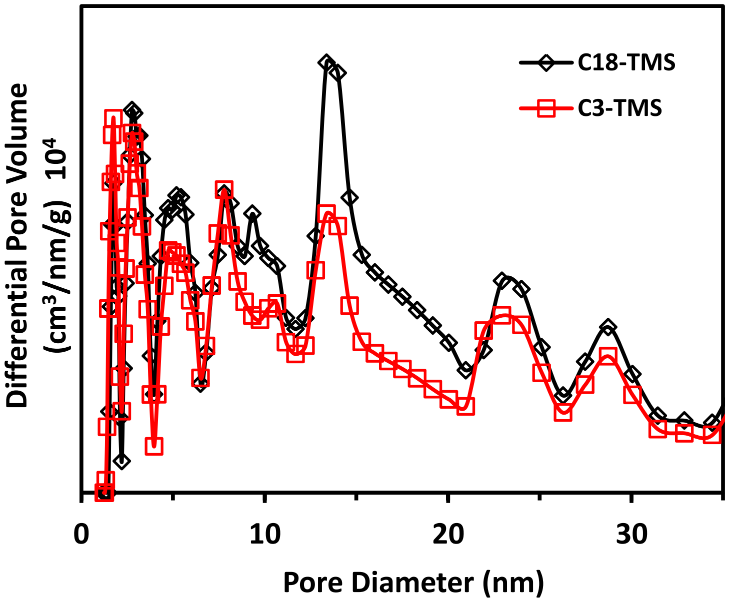

Figure S4.2. Pore size distribution of C18-TMS and C3-TMS treated DE with 0.6 mg/m^2 adsorbed hydrocarbon amount.

S4.2. Thermal characterization

The melting enthalpies for different chain length alkyltrimethoxysilanes on DE are shown in Table S4.1. With increased chain length, the number of van der Waals interactions per chain increased. Therefore, melting temperatures and enthalpies increased with chain length for different alkyltrimethoxysilanes. TMDSC curves for bulk and adsorbed hydrocarbon amounts for different chain lengths as a function of adsorbed amounts are shown in Figures S4.3, S4.4, and S4.5. Finally, the melting temperatures of the alkyltrimethoxysilane in different states are shown in Table S4.2.

Table S4.1. Melting enthalpies for different chain length alkyltrimethoxysilanes with 2.2 mg/m^2 adsorbed hydrocarbon amounts on DE (normalized to the amount of silane).

sample name	ΔH_m (J/g of silane)
C12-TMS	17 ± 3
C16-TMS	24 ± 13
C18-TMS	45 ± 1

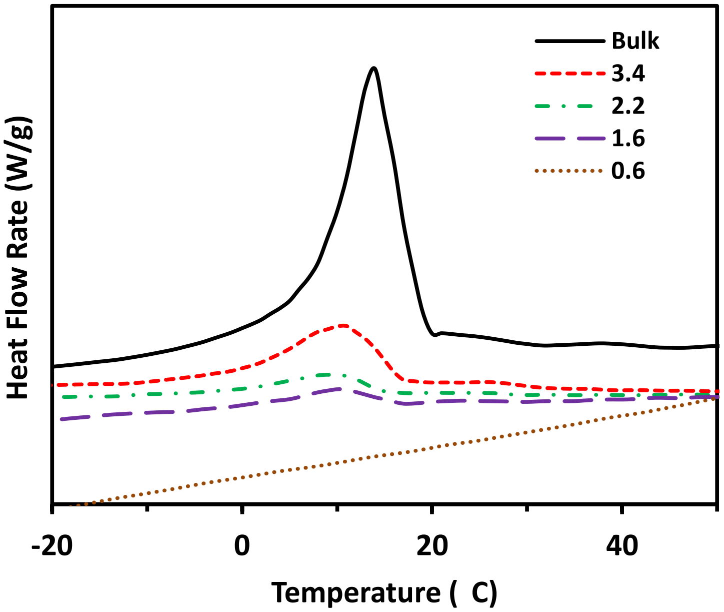

Figure S4.3. TMDSC curves for DE in bulk and with different adsorbed hydrocarbon amounts (in mg/m$^{2)}$ of C12-TMS. With increased adsorbed hydrocarbon amounts the melting temperatures and enthalpies increased, due to the formation of ordered structures. The vertical scales and positions were adjusted for clarity.

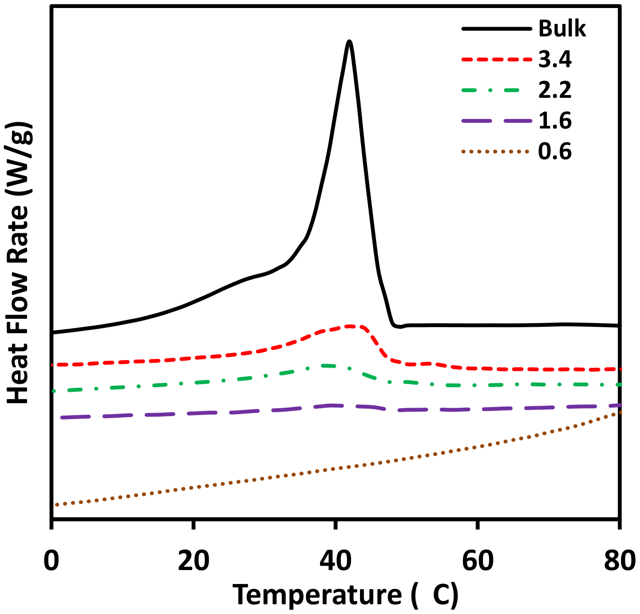

Figure S4.4. TMDSC curves for DE in bulk and with different adsorbed hydrocarbon amounts (in mg/m$^{2)}$ of C16-TMS. With increased adsorbed hydrocarbon amounts the melting temperatures and enthalpies increased, due to the formation of ordered structures. The vertical scales and positions were adjusted for clarity.

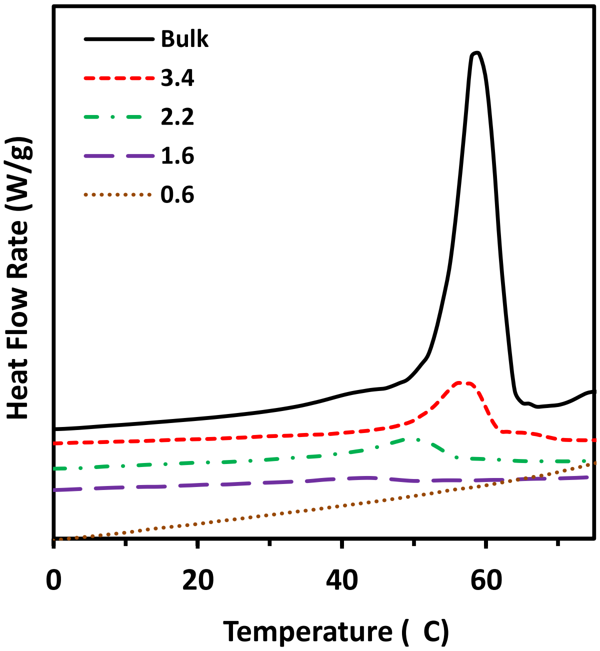

Figure S4.5. TMDSC curves for DE in bulk and with different adsorbed hydrocarbon amounts (in mg/m$^{2)}$ of C18-TMS. With increased adsorbed hydrocarbon amounts the melting temperatures and enthalpies increased, due to the formation of ordered structures. The vertical scales and positions were adjusted for clarity.

Table S4.2. Melting temperatures of the longer chain alkyltrimethoxysilane in different states.

Alkyltrimethoxysilane	Melting Temperature (°C)					
	Monomer	Bulk condensed	Adsorbed amount (mg/m^2)			
			0.6	1.6	2.2	3.4
C12-TMS	-26.8	13.7	NA	10.1	8.6	10.6
C16-TMS	3.1	41.9	NA	38.7	38.3	41.9
C18-TMS	16.0	57.9	NA	43.1	48.9	59.2

S4.3. Contact angle measurements

Contact angle changes with time for 50% particle loading of silane treated DE in polyurethane coatings with different chain lengths of alkyltrimethoxysilanes are shown in Figure S4.6. The number of molecules per nm^2 as a function of adsorbed amount and chain length are shown in Table S4.3.

For these samples, longer chains (C12-C18) showed superhydrophobic properties and did not change much with time. However, shorter chains showed only hydrophobicity and water contact angle decreased with time.

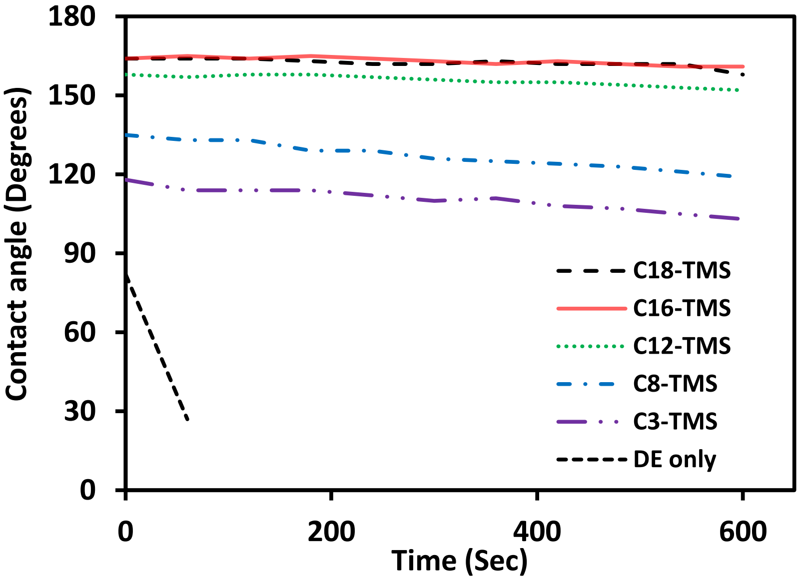

Figure S4.6. Contact angle changes with time for 50% particle loading of 2.2 mg/m^2 adsorbed hydrocarbon amount of silane treated DE in polyurethane coatings with different chain lengths of alkyltrimethoxysilanes.

Table S4.3. Number of molecules per nm^2 as a function of adsorbed amount and chain length.

Alkyltrimethoxysilane	Adsorbed amount (mg/m^2)			
	0.6	1.6	2.2	3.4
	Number of molecules/nm^2			
C3-TMS	8.4	23.3	31.5	47.6
C8-TMS	3.0	9.2	11.8	17.8
C12-TMS	1.8	5.9	7.7	12.1
C16-TMS	1.2	3.8	6.7	8.7
C18-TMS	1.3	4.0	5.2	8.0

CHAPTER V

DEVELOPMENT OF STRUCTURE IN ADSORBED HEXADECYLTRIMETHOXYSILANE ON SILICA

5.1. ABSTRACT

The determination of the structural assemblies of hexadecyltrimethoxysilane (HDTMS) on silica particles were made using temperature–modulated differential scanning calorimetry (TMDSC), thermogravimetric analysis (TGA), Fourier transform infrared spectroscopy (FTIR) and powder X-ray spectroscopy. At very small adsorbed amounts (< 0.6 mg/m^2), HDTMS molecules were individually direct bound to the silica surface through covalent bonding, and their aggregates were primarily amorphous. Direct attachment to the silica surface was found to significantly lower the enthalpies for both melting and crystallization of HDTMS. The enthalpies for the melting of directly bound HDTMS molecules increased linearly with their adsorbed amount until 0.6 mg/m^2. Compared to bulk HDTMS, these bound HDTMS molecules on silica decomposed at higher temperatures. At larger adsorbed amounts of 0.6 mg/m^2 or more, e.g. "multilayer region", both melting and crystallization enthalpies for the HDTMS were found to increase exponentially, and eventually, approach the bulk enthalpies.

The significant enthalpy changes for the melting/crystallization transitions indicated that the adsorbed HDTMS molecules underwent structural changes, from directly bonded on the surface to bulk-like with an exponential constant of about 1.6 mg/m^2.

5.2. INTRODUCTION

Silica, or silicon dioxide, represents a group of widely used minerals with a crystalline or amorphous form.[1] Because of its structural and surface properties,[2] silica has been used in various applications, such as chromatography,[3-4] gelation,[5-6] polymer reinforcement,[7] separation of metal ions,[8] environmental technology,[9] and immobilization of enzymes and catalysts.[10-11] In order to improve the interfacial properties with nonpolar materials, hydrophilic silica surfaces can be modified with organosilanes. It has been shown that the surface properties of organosilane-functionalized silica can be controlled by the reaction conditions (temperature, water content, type and nature of reagent), the number of functional groups on the organosilane, and the surface history.[12-16]

Hydrolyzed organosilanes can react with silica in variety of ways. The structures of the adsorbed organosilanes can play an important role in their function and are dependent on their adsorbed amount. The properties of organically modified silica have been characterized using FTIR,[17-22] NMR,[23-26] Raman spectroscopy,[27-30] fluorescence[31-32] ellipsometry and contact angle measurements.[33] At small adsorbed amounts, the organosilane molecules are typically adsorbed individually and cover the silica surface randomly. In this case, the hydrocarbon chains of the organosilanes are disordered and more flattened on the surface.[34] But with increasing adsorbed amounts, ordered and disordered structures start to form island-like structures, which have more closed packed molecules, plus regions of disordered molecules.[34-36] At larger adsorbed amounts from higher concentrations, organosilane molecules can cross-link through intermolecular condensation of neighboring silanol groups.[37] These siloxane bonds create oligomeric, and even polymeric organosilanes, leading to the formation of more ordered structures. For long chain alkyl groups, these structures are concomitant with the formation of trans conformations.[35,38-40] A maximum surface density (close packed) of 4.5–5 groups/nm^2 can be reached.[33,41-42]

Hydrolyzed long chain alkylsilanes are capable of the formation of closely packed self-assembled monolayers with highly oriented alkyl chains via spontaneous adsorption on to hydrated solid surfaces. Compared to monofunctional silanes, trifunctional organosilanes are more reactive with surface silanols and have greater stability on the surface. Trifunctional organosilane are polymerizable in the presence of proper catalysts, leading to structures on the surface, such as self-assembly (horizontal polymerization), covalent attachments, and vertical polymerization.[33] Organosilane coupling agents typically contain an R-Si(X)$_3$ group, where X is a hydrolysable functional group, such as amine, chloride, methoxy, and ethoxy group, and R is an alkyl group.[43] Several studies have characterized the formation of self-assembled monolayers of organosilanes with long hydrocarbon chains, with and without a solid surface.[44-46] However, the adsorbed structures of the organosilane *at different adsorbed amounts* on silica surface have not been investigated experimentally using differential scanning calorimetry. In this study, hexadecyltrimethoxysilane (HDTMS), an organosilane with a C-16 hydrocarbon tail, was used for modify the surface of silica. A schematic diagram of idealized modifications with HDTMS is shows on Figure 5.1. HDTMS adsorbed structures on silica with different adsorbed amounts were characterized using temperature–modulated differential scanning calorimetry (TMDSC), thermogravimetric analysis (TGA), and Fourier transform infrared spectroscopy (FTIR).

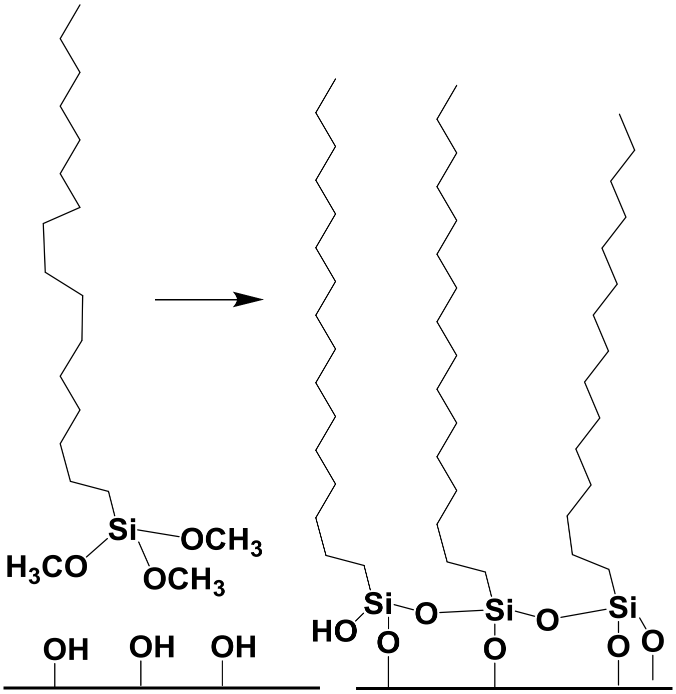

Figure 5.1. Schematic diagram of idealized modifications with HDTMS.

5.3. MATERIALS AND METHODS

HDTMS and LM130 silica were obtained from Gelest Inc. (Morrisville, PA) and Cabot Corporation (Billerica, MA), respectively. The *p*-toluenesulfonic acid monohydrate was (PTSA) from SigmaAldrich (St. Louis, MO) and toluene was from Pharmco-aaper (Brookfield, CT). All chemicals were used as received.

Silica (0.5g) was reacted with different mass fractions of HDTMS in the presence of the catalyst, PTSA (0.02g), in glass vials with 15 mL of toluene. The reactions of the silanes were carried out in a water bath at 50 °C with shaking for 4 h. After shaking, the solutions were cooled to room temperature. The HDTMS treated silica products were obtained by blowing air through the samples. The samples were then kept under vacuum at 40 °C for 48 h prior to analysis.

The grafted amounts of HDTMS on the treated silica were quantified by using a TA Instruments model Q-50 Thermogravimetric Analyzer (TA Instruments, New Castle, DE). The treated silica samples were heated from 20 to 700 °C with a heating rate of 20 °C/min in air.

TMDSC analyses of HDTMS adsorbed silica samples were carried out using a Q-2000 (TA Instruments, New Castle, DE). The heating and cooling scans were run from -50 to 120 °C, and a scan rate of 3 °C/min with a modulation amplitude of ± 1.0 °C/60 s was used. Due to the supercooling behavior of HDTMS, the total heat flow rates were reported. The Universal Analysis software package from TA Instruments was used to calculate the enthalpy changes from the area under the heat flow rate curves.

FTIR spectra were obtained using a Nicolet 50 FTIR spectrometer (Thermo Fisher Scientific Inc., Waltham, MA) in attenuated total reflection (ATR) mode with a smart iTR diamond crystal. The scanning frequencies were from 600 to 4000 cm^{-1} with a spectral resolution 4 cm^{-1} and 64 scans. X-ray diffraction (powder XRD) patterns were obtain on a Bruker AXS Smart APEX diffractometer (Bruker, Billerica, MA) operating with Mo Kα (λ = 0.7107 Å) radiation.

Two-state and multilayer models were used to fit the enthalpy data by iterating on the values of the fitted parameters until the value of the sum of the squares of the residuals was minimized. The uncertainties in each of the parameters were estimated by varying each parameter independently from the set of best-fit values until the sum of the squares of residuals became the predicted sum of the squares of residual, with 95% confident value.[47-48]

5.4. RESULTS

The methylene (CH_2) asymmetric and symmetric stretching frequencies for the adsorbed HDTMS on silica are plotted in Figure 5.2. The CH_2 stretching frequencies are often used to probe the conformation and orientation of alkyl chains.[17,29,49-50] As shown in Figure 5.2, the asymmetric and symmetric CH_2 stretching frequencies were observed around 2916 and 2849 cm^{-1} for the bulk crystalline HDTMS. At the very small adsorbed amounts, the asymmetric and symmetric stretching frequencies for HDTMS were at 2927 and 2856 cm^{-1}, respectively. With increasing adsorbed amounts, both CH_2 stretching frequencies decreased and approached values for the bulk crystalline HDTMS. The asymmetric and symmetric stretching frequencies became constant after adsorbed amounts of about 10 mg/m^2.

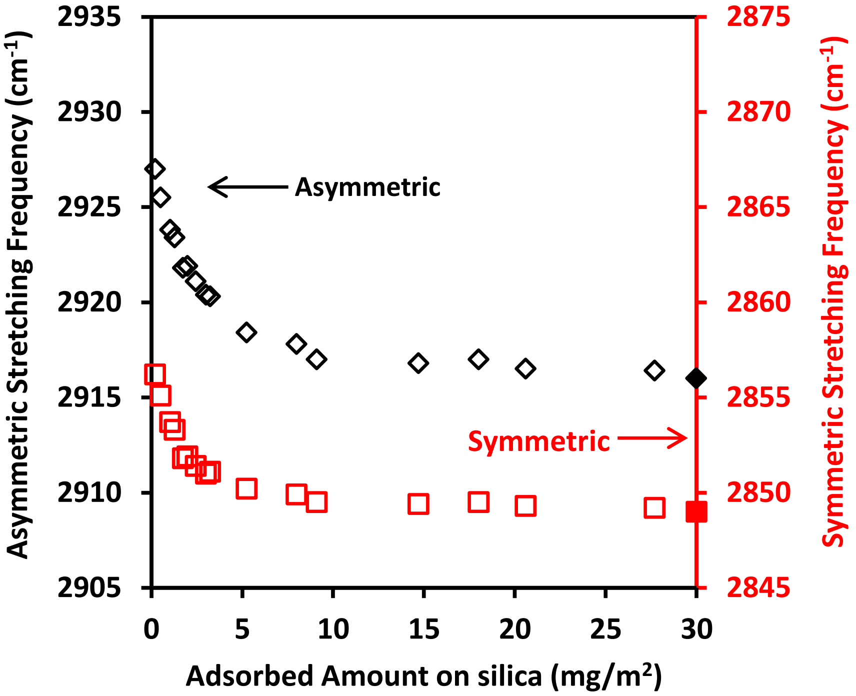

Figure 5.2. Asymmetric (◊) and symmetric (□) vibration frequencies for CH_2 stretches of HDTMS adsorbed silica samples. The values for bulk, crystalline HDTMS, are shown as filled symbols (♦, ■) located at 30 mg/m^2. The experimental uncertainty was roughly the size of the symbols.

The TGA curves for the different adsorbed amounts of HDTMS samples are shown in Figure 5.3. In order to show the nature of the decomposition behavior, the first derivatives of mass losses are plotted against temperature. The TGA curve for crystalline HDTMS showed one main decomposition temperature peak around 519 °C with a tail on the low temperature side. At the lowest adsorbed amount of HDTMS, a single peak was observed around 527 °C. It was asymmetric, with a tail on the lower temperature side. This decomposition temperature was 8 °C higher than that in bulk-crystalline HDTMS. With increased amounts of adsorbed HDTMS, the decomposition peak was first shifted to a lower temperature, and then shifted towards higher temperatures with additional adsorbed HDTMS, eventually reaching the decomposition temperature for bulk crystalline material. It is worth noting that the decomposition on the lower temperature side was still present for all adsorbed samples. Based on the literature,[51-53] the silanes that decomposed at lower temperatures were likely to have significant amorphous fractions of the HDTMS.

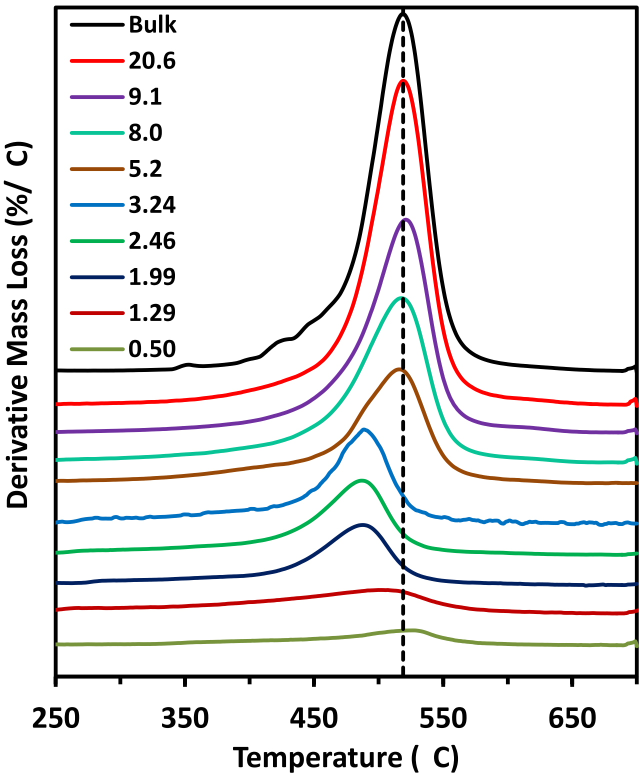

Figure 5.3. Derivative mass loss curves of crystalline and HDTMS adsorbed silica samples. The curves are in the order shown in the legend. The numerical values are the adsorbed amounts in mg HDTMS/m^2 silica.

The thermograms for the melting and crystallization transitions of the hydrocarbon chains of HDTMS are shown in Figure 5.4. The vertical scales for the melting and crystallization thermograms were adjusted to more clearly show the nature of the transition. In Figure 5.4(a), for the heating scan for bulk HDTMS, a significant endothermic peak was found around 42 °C with a tail on the lower temperature side. This temperature is for the melting of the HDTMS hydrocarbon chains originating from the order-disorder arrangements of the hydrocarbon chains.[54] As shown in Figure 5.4(b), the cooling scan for bulk crystalline HDTMS showed an exothermic peak around 37 °C corresponding to the crystallization of the HDTMS hydrocarbon chains. The temperature difference (5 °C in this case) between melting and crystallization implies that the melting/crystallization transition for HDTMS hydrocarbon chain is a supercooling process.

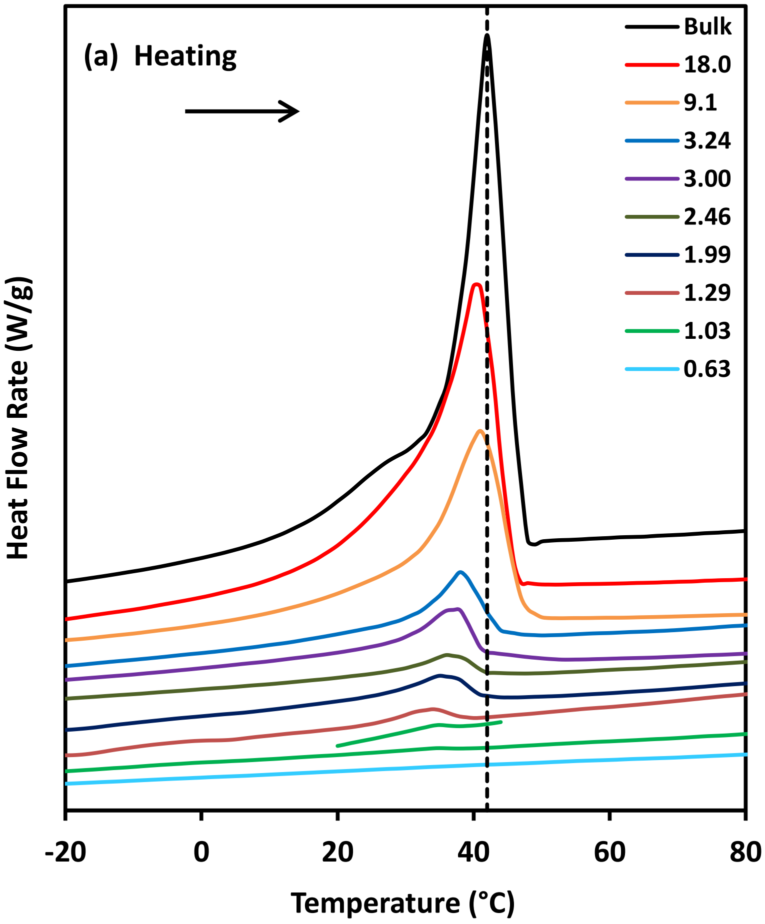

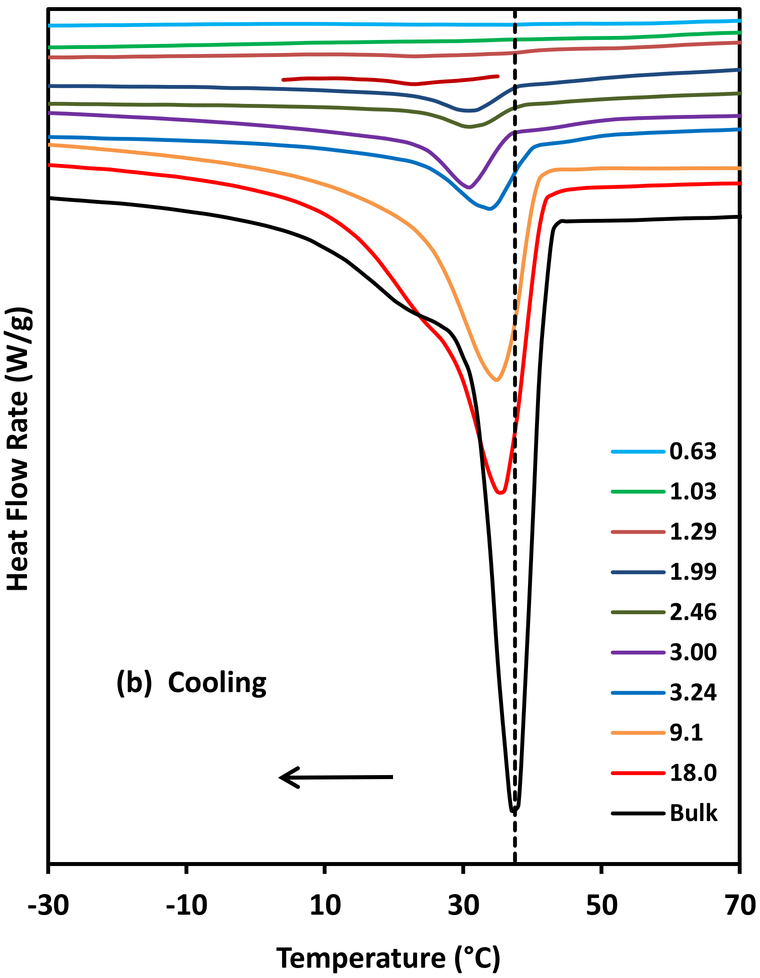

Figure 5.4. Heat flow rates for bulk and surface HDTMS samples from the (a) heating scans with the short trace being a vertically expanded region for the 1.03 mg/m^2 adsorbed amount sample and (b) cooling scans with the short trace for the 1.29 mg/m^2 adsorbed amount sample. The numerical values are the adsorbed amounts in mg HDTMS/m^2 silica and the order as shown in the legends. The thermograms are scaled to make the most prominent components more obvious in the figure.

For the adsorbed samples, a low temperature asymmetric melting peak was centered at 34 °C for the samples with small adsorbed amounts. As the HDTMS adsorbed amount increased, the transition enthalpies increased and a new peak emerged around 37 °C.

With increased adsorbed amounts, the peak centered on 37 °C dominated the transition and moved toward higher temperature with increased intensity. Eventually, it reached the melting temperature for bulk HDTMS. Similarly, at larger adsorbed amounts, the low temperature peak was overshadowed by the larger intensities of higher temperature peak. When the adsorbed amount was greater than 9 mg/m^2, the transition was symmetric and the peak shifted to 40 °C with a tail on the low temperature side.

For the cooling scans of the samples with very small adsorbed amounts of HDTMS, the crystallization transition for HDTMS chains was located around 29 °C with very small enthalpies. With increased adsorbed amounts, the crystallization transitions shifted to the higher temperatures leaving tails on the lower temperature sides. These small tails remained even with higher adsorbed amounts (> 9 mg/m^2), which was consistent with the observations in the heating scans. With further increased adsorbed amounts, the lower temperature peak (around 29 °C) moved toward the bulk temperature with increasing intensity. When the adsorbed amount increased above 9 mg/m^2, the peak temperature remained constant.

The enthalpy changes during the melting and the crystallization of bulk and adsorbed HDTMS samples are shown in the Figure 5.5. The enthalpies were calculated from the area under the peaks. No transition was observed for the silica over the temperature range used in this study. The reported enthalpies for the HDTMS adsorbed samples were normalized to per gram of HDTMS. At each composition, the enthalpies for both melting and crystallization were very similar. The enthalpy for bulk crystalline HDTMS was found to be around 90.0 J/g$_{HDTMS}$. With very small adsorbed amounts of HDTMS (< 0.8 mg/m^2), the enthalpies were very small and increased very gradually. With further increased adsorbed amounts, the enthalpies increased approximately exponentially and approached the bulk values.

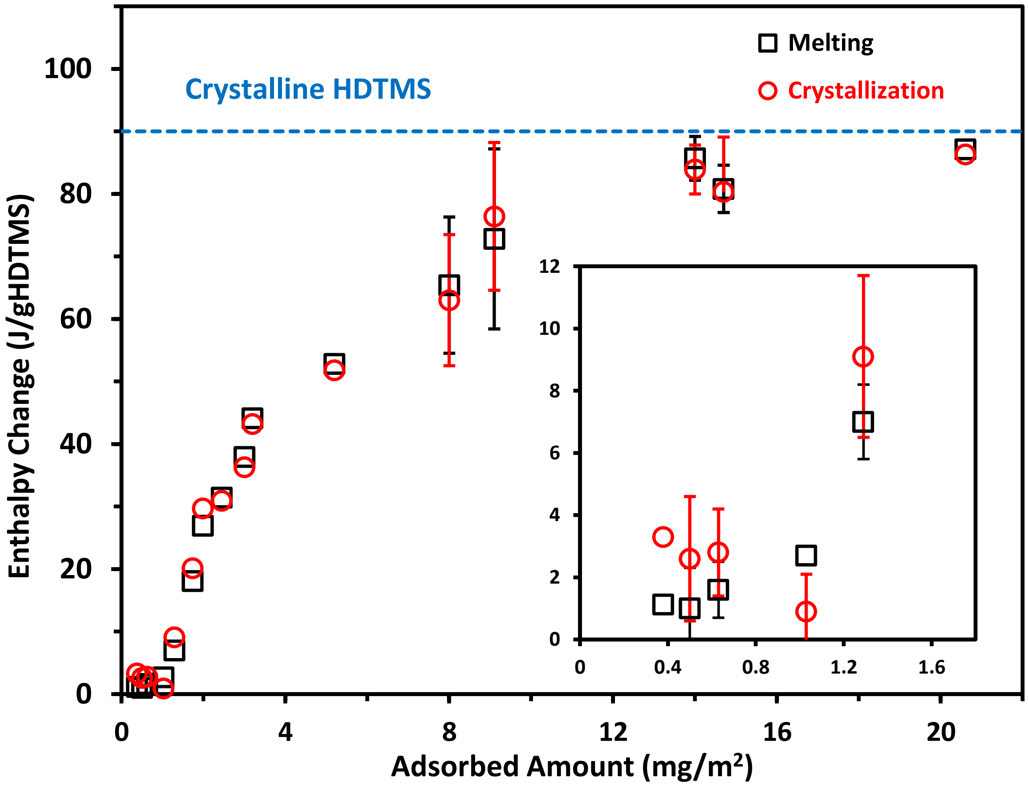

Figure 5.5. Enthalpy change of HDTMS during melting (□) and crystallization (○). One standard deviation is shown by the error bars and in some cases were about or less than the size of the symbols used on data points unless shown.

Two adsorbed samples and the bulk condensed sample were selected for powder XRD analysis: (1) 0.5 mg/m^2 was in the very small adsorbed amount region, (2) 20.6 mg/m^2 was close to the bulk like HDTMS enthalpy, and (3) was bulk condensed HDTMS. The XRD spectra are shown in Figure 5.6. Applying Bragg's Law equation ($d = I/(2 \sin \theta)$, $I = 0.7107$ Å) in to the bulk HDTMS, one peak was observed at $2\theta = 9.6°$ which is assigned to be the lateral interchain spacing for alkyl chains of 4.6 Å.[37,55] With decreasing adsorbed amounts, the peak was broader and centered at a smaller angle, as observed for the sample with an adsorbed amount of 0.5 mg/m^2. Since the presence of amorphous hydrocarbon chains on the surface shows a broad band in the powder XRD,[56] it was likely that the HDTMS structures for the samples with small adsorbed amounts are loosely packed. In contrast, the other samples appear to be more well packed.

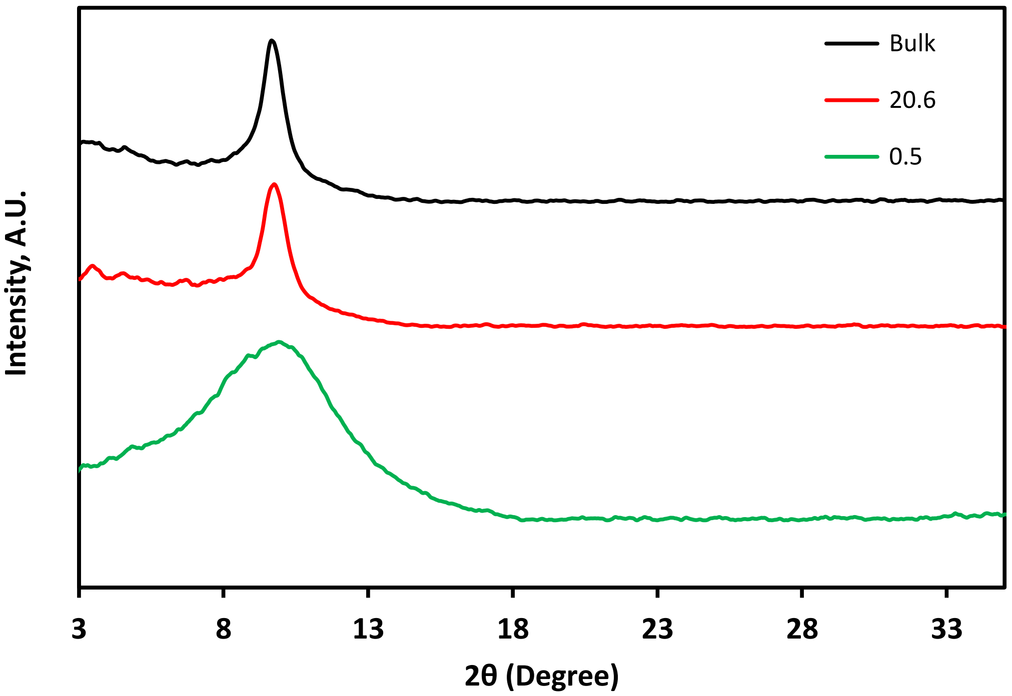

Figure 5.6. Powder XRD spectra of adsorbed 0.5 (bottom) and 20.6 (middle) mg$_{HDTMS}$/m^2, and bulk condensed (top) HDTMS.

5.5. DISCUSSION

The asymmetric and symmetric CH_2 stretching bands are often used to probe the conformations of hydrocarbon chains because they are sensitive to the gauche/trans conformer ratio. The CH_2 frequency for bulk HDTMS was very close to that for crystalline n-alkanes.[35] Therefore, the bulk condensed HDTMS has highly ordered trans-

trans conformations below melting temperature[57] due to the packing density of the hydrocarbon chains. For the adsorbed amounts less than 1 mg/m^2, antisymmetric CH_2 stretching frequencies were very close to those of liquid alkanes (2927 cm^{-1}). This indicates that the hydrocarbon chains of HDTMS on silica at very small adsorbed amounts were rather disordered and contained many trans and gauche conformations.[58] In addition, the adsorbed hydrocarbon chains showed very small enthalpies in both melting and crystallization (Figure 5.4(a) and 5.4(b)), which is in agreement with the observation that most of the HDTMS molecules are more likely to be in disordered structures. With increasing adsorbed amounts, the shifting of the stretching frequency of CH_2 bonds toward lower frequency, suggested increased conformational order on the surface of silica. With adsorbed amounts of greater than 10 mg/m^2, the asymmetric and symmetric stretching frequencies remained constant and reached the bulk value for crystalline alkanes of about 2916 and 2849 cm^{-1}, respectively.[29,35] The density of hydrocarbon chains on the silica surface increased because of the interactions between the neighboring chains.

While a variety of studies have been made on silane coupling agents, the dependence of decomposition temperatures on adsorbed amount have not been the focus of studies in the literature.[52,59-62] We found that the hydrocarbon chain decomposition temperatures were sensitive to the arrangements of HDTMS molecules on the surface of silica. From the TGA results, the decomposition temperatures moved around with different adsorbed amounts; higher decomposition temperatures for small adsorbed amounts, lower decomposition temperatures for intermediate adsorbed amounts, and, again, higher decomposition temperatures for larger adsorbed amounts, which were similar to the bulk-like structure. As seen in Figure 5.3, at adsorbed amounts less than 1.3 mg/m^2, the decomposition temperature was slightly higher than the bulk condensed decomposition temperature. Based on the literature, typically, the thermal decomposition of adsorbed organic molecules occur at higher temperature than that for bulk species.[49] It is likely, based on the infrared data, that the HDTMS molecules were directly bound to the surface randomly as flat isolated molecules[34,43,63-64] yielding a higher decomposition temperature as well. Overall the thermal stability of the adsorbed samples was lower than bulk HDTMS similar to that observed with adsorbed octadecyltrichlorosilane compared to polyoctadecylsiloxane.[65] This difference may be due to differences in the structural arrangements of the adsorbed samples compared to the bulk condensed ones.[65]

Decomposition of long organic chains occur through the β elimination, where the first two carbon atoms next to the head group are arranged parallel to the surface. This transition state only occurs at higher temperature, leading to a higher decomposition temperature as observed for the adsorbed HDTMS.[66-67] With increased adsorbed amounts, the decomposition temperature shifted to lower temperatures, which may be due to the formation of amorphous oligomers patchwise on the surface[43] from the vertical polycondensation of HDTMS molecules.[33] As a result of vertical polymerization, many molecules were not directly attached to the surface. Therefore, decomposition temperatures started to move toward the lower temperature side. In the adsorption of cetyltrimethylammomiun bromide (CTAB) of Zhang el al.,[49] the transition from monolayer to multilayer could easily be distinguished in the thermograms. Because at the small adsorbed amounts, CTAB molecules were individually attached and formed monolayers, with further increases the adsorbed amount, multilayer formation was observable as a shoulder. The difference for this HDTMS system may be due to the oligomerization of the silane coupling agent in the solution at higher coupling agent concentrations. At higher concentrations, it is likely that the silane molecules were not bound as individual molecules. With increasing adsorbed amounts (> 5 mg/m^2), decomposition temperatures increased toward the bulk decomposition temperature due to the formation of crystalline structures on the surface of silica similar to that of the bulk material.[52] It has been proposed that the lower-temperature side of the bulk transition for adsorbed HDTMS decomposition peaks, originates from the presence of the less crystalline alkylsilanes.[52]

For adsorbed amounts smaller than 1 mg/m^2 the adsorbed HDTMS have very small enthalpy changes for the melting which were assumed to increase linearly with the adsorbed amounts (vide infra). In contrast, the crystallization enthalpies, in this range, do not show linearity. The exact nature of this region is uncertain as the enthalpies are very small, even an order of magnitude smaller than these in CTAB at similar compositions.[49] The melting and crystallization enthalpies appeared to increase exponentially with further increased adsorbed amounts, which indicated a structural arrangement change occurred in the HDTMS molecular arrangement when molecules are going from surface (molecules directly adsorbed to the surface) to bulk like structures. This transition to exponential behavior occurred in a range roughly the size of the cross-section of a hexadecane molecule (0.54 nm^2) in solution.[68]

In order to interpret the transition enthalpies as a function of adsorbed amount and determine how the properties varied with adsorbed amount, we tested two different models. The first of which was a simple two-state model, in which the enthalpy changes of the adsorbed HDTMS on silica consisted of two distinct layers, a "monolayer" and a "bulk-like layer". The second model, called the multilayer model, consisted of a monolayer and a series of multilayers which transitioned the adsorbed silanes from monolayer to bulk-like.

In the two-state model, the first layer, corresponded to the formation of (i) "monolayer-like" surface bound HDTMS, in which the enthalpy linearly increased with adsorbed amount. Beyond the monolayer amount, (ii) bulk-like material, with a constant enthalpy was added. The total enthalpy changes for these layers consisted of: ΔH_1, the enthalpy for directly bound HDTMS and ΔH_{bl}, the enthalpy for bulk-like HDTMS (above the first layer). The total enthalpy for the adsorbed HDTMS layers, $\Delta \mathrm{H}_{\mathrm{HDTMS}}$, (enthalpy for melting per g of HDTMS) was calculated using Equation 5.1a[49]

$$\Delta H_{HDTMS} = \frac{m_1 \Delta H_1 + m_{bl} \Delta H_{bl}}{M_{HDTMS}} \tag{5.1a}$$

where m_1 and m_{bl} are the masses of the HDTMS in the monolayer and bulk-like HDTMS on 1 m^2 of silica surface, respectively, and M_{HDTMS} is the total mass for HDTMS.

In the multilayer model, m_{bl} and ΔH_{bl} were replaced by m_{ml} and ΔH_{ml}. Similarly, the enthalpy of the multilayer model is given by equation 5.1b,

$$\Delta H_{HDTMS} = \frac{m_1 \Delta H_1 + m_{ml} \Delta H_{ml}}{M_{HDTMS}} \tag{5.1b}$$

where m_{ml} and ΔH_{ml} are the for the multilayers. It should be noted that as ΔH_{bl} was taken to be a constant, ΔH_{ml} varied as a function of the adsorbed amount.

At small adsorbed amounts, the silane molecules were attached to the silica surface randomly, and formed isolated structures fairly randomly on the surface with the hydrocarbon chains interacting with the silica. As chains were added, they interacted, resulting in an increase in HDTMS enthalpy (ΔH_1) with adsorbed amount. It should be noted that in trialkoxy-silane coupling agent systems, there was the likelihood of the formation of oligomers in solution before deposition can take place. In which case, this monolayer would not necessarily be a uniform monolayer as with the other systems reported in literature.[49,69-70] In melting, these surface attached silane molecules ("monolayer like") have a linear dependence with the ΔH_1 [49] or

$$\Delta H_1 = Am_1 \tag{5.2}$$

where A is the slope parameter. The initial HDTMS silane molecules are expected to be adsorbed randomly and relatively flat on the surface. Then with an addition of more silane coupling agent molecules, form patchwise structures on the surface of silica. This results in the hydrocarbon chains extending away from the surface. As more chains are more extended, the enthalpy per gram of HDTMS increased until a "monolayer-like" coating was formed. The total amount of HDTMS in the monolayer-like material is denoted, m_1'. After the completion of the "monolayer-like" structure, addition of more silane molecules formed different structures on the top of the monolayer. Based on the *two-state model*, the bulk-like silanes are taken to have a constant enthalpy (ΔH_{bl}) which does not vary with the amount of adsorbed HDTMS silane. The results of fitting the enthalpy data to the two-state model are shown in Figure 5.7 and the fitted parameters shown in Table 5.1.

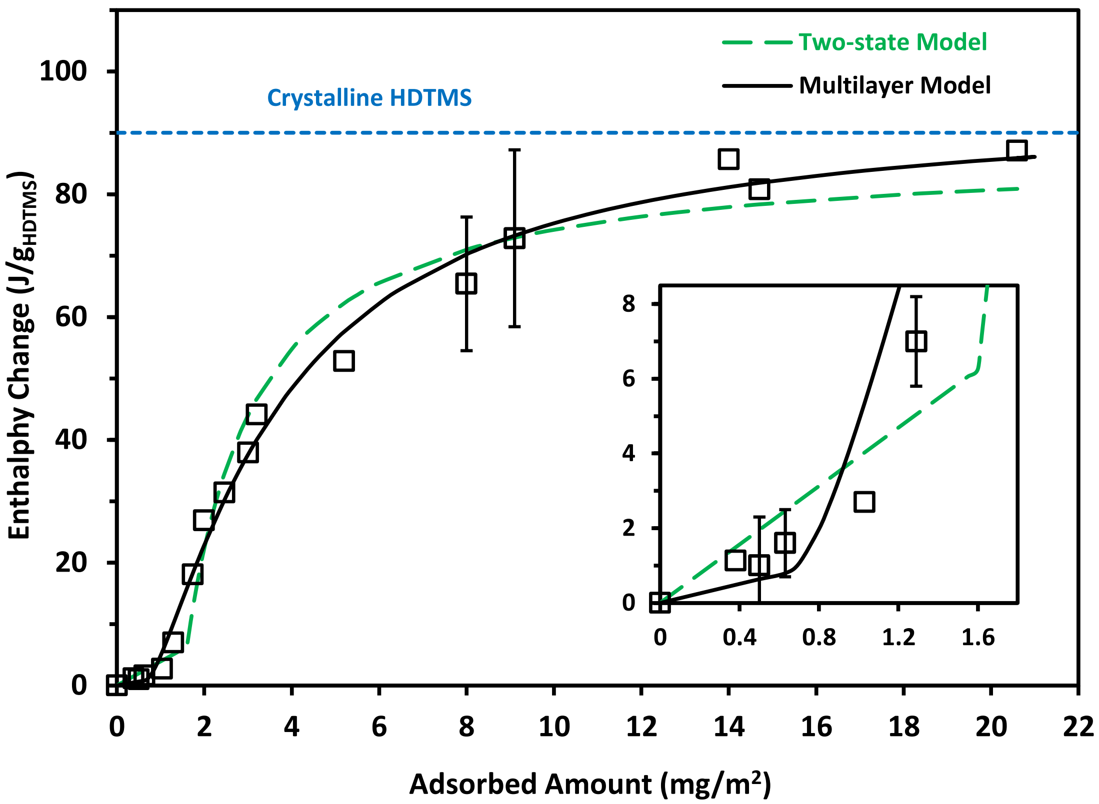

Figure 5.7. Enthalpy of melting of adsorbed HDTMS as a function of adsorbed amount showing the fits from the *two-state* and *multilayer model*. The horizontal dashed line shows the enthalpy for the bulk condensed HDTMS. The inset shows the behavior in the small adsorbed amount region.

The best-fit parameters for the *two-state model* are listed in the Table 5.1. For a complete monolayer coverage, ΔH_1 (= Am_1') was found to be 6.2 J/g with m_1' = 1.60 mg/m^2 of adsorbed HDTMS, where m_1' is the value of m_1 for full monolayer coverage. For the adsorbed amounts larger than 1.60 mg/m^2, a multilayer enthalpy, ΔH_{bl} of 87.2 J/g, was found. This fitted ΔH_{bl} was slightly lower than the bulk HDTMS value of 90 J/g. While the two-state model does approach the bulk HDTMS value with increasing adsorbed amount, the fit as shown in Figure 5.7, was not totally satisfying.

The *two-state model* fits well for the very small adsorbed amount samples, but overestimates the amount for full monolayer coverage, m_1'. In the intermediate range, this model overestimated the enthalpy. At larger adsorbed amounts the two-state model underestimated the enthalpy. The increasing of the melting and the crystallization temperature with increasing adsorbed amount indicates the formation of more ordered HDTMS layers with increased adsorbed amounts. FT-IR frequencies, at small adsorbed amounts, for the CH_2 resonance position indicated mostly gauche conformations and trans conformations at larger adsorbed amounts. Thus, both FTIR and thermal analysis data independently suggest that the behavior of the adsorbed chains change with adsorbed amounts. In particular, the first few layers (just top of the monolayer) in the HDTMS multilayers were not bulk-like.

Table 5.1. Fitting Parameters for the Enthalpy Models for Adsorbed HDTMS on silica

model	**A (J/g) (m^2/mg)**	**ΔH_{bl} or $\Delta H_{ml}'$ (J/g)**	**m_1' (mg/m^2)**	**a (mg/m^2)**	**SD***
two-state	3.9 (± 5.08)	87.2 (± 7.3)	1.60 (± 0.25)	_	4.8
multilayer	1.3 (± 4.8)	95.2 (± 5.6)	0.62 (± 0.17)	1.56 (± 0.3)	2.9

* SD is the standard deviation of the residuals from the fits to the models.

Perhaps a better approach to estimating the enthalpy variation with the adsorbed amount is a "multilayer model". In this case, we have chosen a simple exponential dependence of the enthalpy on the adsorbed amount, m. Starting with the enthalpy for the monolayer, we have chosen an exponential dependence on the enthalpy as it transitions to bulk. This dependence has been effective for the prediction for the modelling of the enthalpy of adsorbed CTAB.[49] In the monolayer regime, the enthalpy from the two models are similar. The total enthalpy is given for the monolayer region by equation 5.3a, for the post monolayer region by equation 5.3b. In equation 5.3c, the integral is expanded to show the form that the data was fit to:

$$\Delta H_{HDTMS} = \ m_1 \Delta H_1 \ /M_{HDTMS} \ \text{(for sub- and monolayer, } 0 \leq \text{m}_1 \leq \text{m}_1\text{')} \qquad (5.3a)$$

$$\Delta H_{HDTMS} = \ m_1{}'\Delta H_1 + \ {}_{m_1'}^{m_1} \ \Delta H_1 + \Delta H_2 \ \ 1 - e^{-x/a} \ \ \ dx \ \ /M_{HDTMS} \ \text{(for m}_1 \geq \text{m}_1\text{')} \qquad (5.3b)$$

$$\Delta H_{HDTMS} = \ m_1' \Delta H_1 + \ m_1 - m_1' \ \ \ m_1' A + \Delta H_2 \ \ \ + \ \ \Delta H_2 a e^{\frac{- \ m - m_1'}{a}} \ \ -1 \ \ /M_{HDTMS} \qquad (5.3c)$$

where *a* is the exponential constant which describes the scale for which the adsorbed amount transitions to bulk behavior. The best fit to the *multilayer model* is plotted in the Figure 5.7 with the parameters given in Table 5.1, and parameters of *A* = 1.3 (J/g) (m^2/mg) (ΔH_1' = Am_1' = 0.81 J/g) and m_1' = 0.62 mg/m^2 were found. In addition, ΔH_2 = 95.2 J/g and *a* = 1.6 mg/m^2 were found from the fitting. Compared with *two-state model*, *multilayer model* fits better with the experimental data as can be seen in the figure and also in the size of the standard deviation of the residuals in Table 5.1.

From *multilayer model*, the parameters yielded insight on the behavior of the adsorbed HDTMS. The maximum enthalpy was obtained when the adsorbed amount approached infinity, ΔH_{ml}' = ΔH_1' + ΔH_2 = 96.0 J/g, which was close to the crystalline HDTMS enthalpy (90.0 J/g). Bulk HDTMS enthalpy had a value which was smaller than the bulk CTAB (155 J/g of CTAB), for example.[49] With the same numbers of carbon atoms in the hydrocarbon chains, the different head group can significantly affect the bulk enthalpy. The oligomerization and surface bonding of HDTMS changes the registry of the hydrocarbon tails obviously making them less or more imperfectly crystallinity.

The growth of the enthalpy in the multilayer region, was shown to be well modelled as an exponential dependence. This growth is modelled by the distance parameter, "*a*" in equation 5.3(b). The value of the *a* was 1.6 mg/m^2 which was similar to CTAB distance scale parameter which was 1.2 mg/m^2.[49] This parameter was an effective measure of the distance scale describing the surface effects. It is interesting to note the similarities between HDTMS and CTAB on silica.

Putting all data together we were able understand how the HDTMS molecules are arranged on the surface of silica. The first "monolayer-like" structure is mostly amorphous and this "monolayer-like" material is followed by multilayers, which approaching bulk like HDTMS with an exponential dependence with a constant of about 1.6 mg/m^2, or assuming a density of about 1 g/cm^3, about 1.6 nm worth of material.

5.6. CONCLUSIONS

In this chapter, we have probed the structural arrangement of HDTMS molecules on a silica surface using FTIR and TMDSC. With small adsorbed amounts of HDTMS, form disordered "monolayer-like" structures on the silica with small enthalpies of melting/crystallization. The enthalpies increased linearly with the adsorbed amount up to 0.6 mg/m^2 ("monolayer-like"). With the increasing adsorbed amounts > 0.6 mg/m^2, multilayers started to form with increasing ordered arrangements of HDTMS chains. The enthalpy variation for melting and crystallization was able to be modelled quite successfully with multilayer model. The enthalpies were small for the monolayer-like (0.81 J/g, linearly dependent on the adsorbed amount) material. Multilayers had an exponential dependency with the adsorbed amount. Multilayer structures were able to reach the bulk like HDTMS eventually with the increasing adsorbed amount with an exponential distance scale of about 1.6 nm.

5.7. ACKNOWLEDGEMENTS

The authors thank Dr. Reza Latifi for measuring the powder XRD for the HDTMS adsorbed silica samples and the financial support of the Dry Surface Coating Guthrie, OK and the Oklahoma State University.

5.8. REFERENCES AND NOTE

(1) Leadbetter, A. J. *J. Chem. Phys* **1969**, *51*, 779.

(2) Walcarius, A. *Electroanalysis* **1998**, *10*, 1217.

(3) Vidal, A.; Papirer, E.; Wang Meng, J.; Donnet, J. B. *Chromatographia* **1987**, *23*, 121.

(4) Grushka, E.; Kikta, E. J. *Anal. Chem.* **1977**, *49*, 1004A.

(5) Zhang, T.; Xu, G.; Regev, O.; Blum, F. D. *J. Colloid Interface Sci.* **2016**, *461*, 128.

(6) Zhang, T.; Xu, G.; Li, Z.-F.; Regev, O.; Maddumaarachchi, M.; Blum, F. D. *J. Colloid Interface Sci.* **2015**, *451*, 161.

(7) Hong, R. Y.; Fu, H. P.; Zhang, Y. J.; Liu, L.; Wang, J.; Li, H. Z.; Zheng, Y. *J. Appl. Polym. Sci.* **2007**, *105*, 2176.

(8) Jal, P. K.; Patel, S.; Mishra, B. K. *Talanta* **2004**, *62*, 1005.

(9) Huang, H. Y.; Yang, R. T.; Chinn, D.; Munson, C. L. *Ind. Eng. Chem. Res.* **2003**, *42*, 2427.

(10) Jonkheijm, P.; Weinrich, D.; Schröder, H.; Niemeyer, C. M.; Waldmann, H. *Angew. Chem. Int. Ed.* **2008**, *47*, 9618.

(11) Angeletti, E.; Canepa, C.; Martinetti, G.; Venturello, P. *Tetrahedron Lett.* **1988**, *29*, 2261.

(12) Parikh, A. N.; Allara, D. L.; Azouz, I. B.; Rondelez, F. *J. Phys. Chem.* **1994**, *98*, 7577.

(13) Fairbank, R. W. P.; Wirth, M. J. *J. Chromatogr. A* **1999**, *830*, 285.

(14) Bierbaum, K.; Grunze, M.; Baski, A. A.; Chi, L. F.; Schrepp, W.; Fuchs, H. *Langmuir* **1995**, *11*, 2143.

(15) Vallant, T.; Brunner, H.; Mayer, U.; Hoffmann, H.; Leitner, T.; Resch, R.; Friedbacher, G. *J. Phys. Chem. B* **1998**, *102*, 7190.

(16) Lambert, A. G.; Neivandt, D. J.; McAloney, R. A.; Davies, P. B. *Langmuir* **2000**, *16*, 8377.

(17) Kaas, R. L.; Kardos, J. L. *Polym. Eng. Sci.* **1971**, *11*, 11.

(18) Graf, R. T.; Koenig, J. L.; Ishida, H. *Anal. Chem.* **1984**, *56*, 773.

(19) Chiang, C.-h.; Koenig, J. L. *J. Colloid Interface Sci.* **1981**, *83*, 361.

(20) Chiang, C.-H.; Ishida, H.; Koenig, J. L. *J. Colloid Interface Sci.* **1980**, *74*, 396.

(21) Chiang, C.-H.; Koenig, J. L. *Polym. Compos.* **1980**, *1*, 88.

(22) Blitz, J. P.; Murthy, R. S. S.; Leyden, D. E. *J. Colloid Interface Sci.* **1988**, *121*, 63.

(23) Kang, H.-J.; Meesiri, W.; Blum, F. D. *Mater Sci Eng A* **1990**, *126*, 265.

(24) Zaper, A. M.; Koenig, J. L. *Polym. Compos.* **1985**, *6*, 156.

(25) Clauss, J.; Schmidt-Rohr, K.; Adam, A.; Boeffel, C.; Spiess, H. W. *Macromolecules* **1992**, *25*, 5208.

(26) Pursch, M.; Brindle, R.; Ellwanger, A.; Sander, L. C.; Bell, C. M.; Händel, H.; Albert, K. *Solid State Nucl. Magn. Reson.* **1997**, *9*, 191.

(27) Orendorff, C. J.; Ducey, M. W.; Pemberton, J. E. *J. Phys. Chem. A* **2002**, *106*, 6991.

(28) Harrand, M. *J. Chem. Phys* **1983**, *79*, 5639.

(29) Snyder, R. G.; Strauss, H. L.; Elliger, C. A. *J. Phys. Chem.* **1982**, *86*, 5145.

(30) Doyle, C. A.; Vickers, T. J.; Mann, C. K.; Dorsey, J. G. *J. Chromatogr. A* **2000**, *877*, 25.

(31) Lochmuller, C. H.; Colborn, A. S.; Hunnicutt, M. L.; Harris, J. M. *J. Am. Chem. Soc.* **1984**, *106*, 4077.

(32) Lochmüller, C. H.; Marshall, D. B.; Wilder, D. R. *Anal. Chim. Acta* **1981**, *130*, 31.

(33) Fadeev, A. Y.; McCarthy, T. J. *Langmuir* **2000**, *16*, 7268.

(34) Ulman, A. *Chem. Rev.* **1996**, *96*, 1533.

(35) Parikh, A. N.; Liedberg, B.; Atre, S. V.; Ho, M.; Allara, D. L. *J. Phys. Chem.* **1995**, *99*, 9996.

(36) Liu, Y.; Wolf, L. K.; Messmer, M. C. *Langmuir* **2001**, *17*, 4329.

(37) Parikh, A. N.; Schivley, M. A.; Koo, E.; Seshadri, K.; Aurentz, D.; Mueller, K.; Allara, D. L. *J. Am. Chem. Soc.* **1997**, *119*, 3135.

(38) Kessel, C. R.; Granick, S. *Langmuir* **1991**, *7*, 532.

(39) Brzoska, J. B.; Azouz, I. B.; Rondelez, F. *Langmuir* **1994**, *10*, 4367.

(40) Allara, D. L.; Parikh, A. N.; Rondelez, F. *Langmuir* **1995**, *11*, 2357.

(41) Helm, C. A.; Möhwald, H.; Kjaer, K.; Als-Nielsen, J. *Biophys. J.* **1987**, *52*, 381.

(42) Blum, F. D.; Meesiri, W.; Kang, H.-J.; Gambogi, J. E. *J. Adhes. Sci. Technol.* **1991**, *5*, 479.

(43) Daniels, M. W.; Francis, L. F. *J. Colloid Interface Sci.* **1998**, *205*, 191.

(44) Bourlinos, A. B.; Chowdhury, S. R.; Jiang, D. D.; An, Y.-U.; Zhang, Q.; Archer, L. A.; Giannelis, E. P. *Small* **2005**, *1*, 80.

(45) Ni, L.; Chemtob, A.; Croutxé-Barghorn, C.; Brendlé, J.; Vidal, L.; Rigolet, S. *J. Mater. Chem.* **2012**, *22*, 643.

(46) Ni, L.; Chemtob, A.; Croutxé-Barghorn, C. l.; Brendlé, J.; Vidal, L.; Rigolet, S. v. *Langmuir* **2012**, *28*, 7129.

(47) Motulsky, H.; Christopoulos, A. *Fitting models to biological data using linear and nonlinear regression: a practical guide to curve fitting*; OUP USA: San Diego, CA, 2004, p 109.

(48) Alternatively, we also fit data using the normalized residuals (residual divided by the experimental value) as the criteria for the best fit. This method put greater emphasis on the smaller enthalpy values from the small adsorbed amount samples. This method yielded a slope of 2.4 J/g and monolayer adsorbed amount of 0.93 mg/m^2, and ΔH_{ml} of 85.6 J/g. Since the enthalpy values at small adsorbed amounts were small and known with much less accuracy, we felt that this fit was less satisfactory in the large enthalpy region where the values are known with much greater accuracy.

(49) Zhang, T.; Xu, G.; Puckette, J.; Blum, F. D. *J. Phys. Chem. C* **2012**, *116*, 11626.

(50) Porter, M. D.; Bright, T. B.; Allara, D. L.; Chidsey, C. E. D. *J. Am. Chem. Soc.* **1987**, *109*, 3559.

(51) Ni, L.; Rigolet, S.; Chemtob, A.; Croutxé-Barghorn, C.; Brendlé, J.; Vidal, L. *Comptes Rendus Chimie* **2013**, *16*, 897.

(52) Dhôtel, A.; Li, H.; Fernandez-Ballester, L.; Delbreilh, L.; Youssef, B.; Zeng, X. C.; Tan, L. *J. Phys. Chem. C* **2011**, *115*, 10351.

(53) T. J. Keene, M.; D. M. Gougeon, R.; Denoyel, R.; K. Harris, R.; Rouquerol, J.; L. Llewellyn, P. *J. Mater. Chem.* **1999**, *9*, 2843.

(54) Bourlinos, A. B.; Chowdhury, S. R.; Jiang, D. D.; An, Y. U.; Zhang, Q.; Archer, L. A.; Giannelis, E. P. *Small* **2005**, *1*, 80.

(55) Shimojima, A.; Sugahara, Y.; Kuroda, K. *Bull. Chem. Soc. Jpn.* **1997**, *70*, 2847.

(56) Iwamoto, K.; Ohnuki, Y.; Sawada, K.; Senō, M. *Molecular Crystals and Liquid Crystals* **1981**, *73*, 95.

(57) Okouchi, M.; Yamaji, Y.; Yamauchi, K. *Macromolecules* **2006**, *39*, 1156.

(58) Urata, C.; Masheder, B.; Cheng, D. F.; Hozumi, A. *Langmuir* **2012**, *28*, 17681.

(59) Kim, J. T.; Lee, D. Y.; Oh, T. S.; Lee, D. H. *J. Appl. Polym. Sci.* **2003**, *89*, 2633.

(60) Yang, H.; Li, F.; Shan, C.; Han, D.; Zhang, Q.; Niu, L.; Ivaska, A. *J. Mater. Chem.* **2009**, *19*, 4632.

(61) Nishio, E.; Ikuta, N.; Hirashima, T.; Koga, J. *Appl. Spectrosc.* **1989**, *43*, 1159.

(62) Xu, L.; Zhuang, W.; Xu, B.; Cai, Z. *Appl. Surf. Sci.* **2011**, *257*, 5491.

(63) Ishida, H. *Polym. Compos.* **1984**, *5*, 101.

(64) Naik, V. V.; Sta□dler, R.; Spencer, N. D. *Langmuir* **2014**, *30*, 14824.

(65) Wang, R.; Baran, G.; Wunder, S. L. *Langmuir* **2000**, *16*, 6298.

(66) Heinz, H.; Castelijns, H. J.; Suter, U. W. *J. Am. Chem. Soc.* **2003**, *125*, 9500.

(67) Jiménez, R. M.; Soltero, J. F. A.; Manríquez, R.; López-Dellamary, F. A.; Palacios, G.; Puig, J. E.; Morini, M.; Schulz, P. C. *Langmuir* **2002**, *18*, 3767.

(68) Smith, A. L. *Theory and Practice of Emulsion Technology: Proceedings ... Edited by A.L. Smith*; Academic Press, London, 1976.

(69) Tao, Y. T. *J. Am. Chem. Soc.* **1993**, *115*, 4350.

(70) Arnold, T.; Parker, J. E.; Macdonald, P. *J. Phys. Chem. C* **2012**, *116*, 10599.

CHAPTER VI

STRUCTURAL ARRANGEMENT OF HEXADECYLTRIMETHOXYSILANE ON DIATOMACEOUS EARTH

6.1. ABSTRACT

Fabrication of superhydrophobic coats with the help of mico-nano particles become an interesting topic on research field during last few years. Recently exoskeleton of diatoms started to use on formation of superhydrophobic coating, because of its wide accessible, cheap, and micro/nano scale morphology. Most of the superhydrophobic coatings were synthesis with the help of low surface energy silanes. The structural association of silane coupling agents on the surface of diatomaceous earth (DE) was studied with the help of different techniques, such as, temperature–modulated differential scanning calorimetry (TMDSC), thermogravimetric analysis (TGA), X-ray spectroscopy and Fourier transform infrared spectroscopy. Hexadecyltrimethoxysilane (HDTMS) was used for the determination of structural properties of the silane on the surface of DE. At smaller HDTMS adsorbed amounts, higher decomposition temperature was observed compared to the bulk HDTMS due to the molecules being directly bound to the surface.

FTIR and TMDSC results confirmed that at smaller adsorbed amounts, the molecules were amorphous. However, compared to HDTMS adsorption on silica, in DE at smaller adsorbed amounts enthalpies were unable to be measured. Further increased adsorbed amounts caused the enthalpies to increase exponentially and eventually reach the bulk HDTMS value.

6.2. INTRODUCTION

Silica sedimentary rock formed from eukaryotic, single-celled, photosynthetic algae are known as diatomaceous earth or kieselgur.[1-3] Siliceous rocks are mainly made of diatom's silicon dioxide shells (frustules), which can be found in nearly every aquatic habitat (both marine and fresh water) on earth.[4,5] Diatoms have unique three-dimensional structures of frustules with highly-ordered micro-nano pore architecture. Figure 6.1 shows typical scanning electron micrographs of the structure of two different kinds of diatoms.

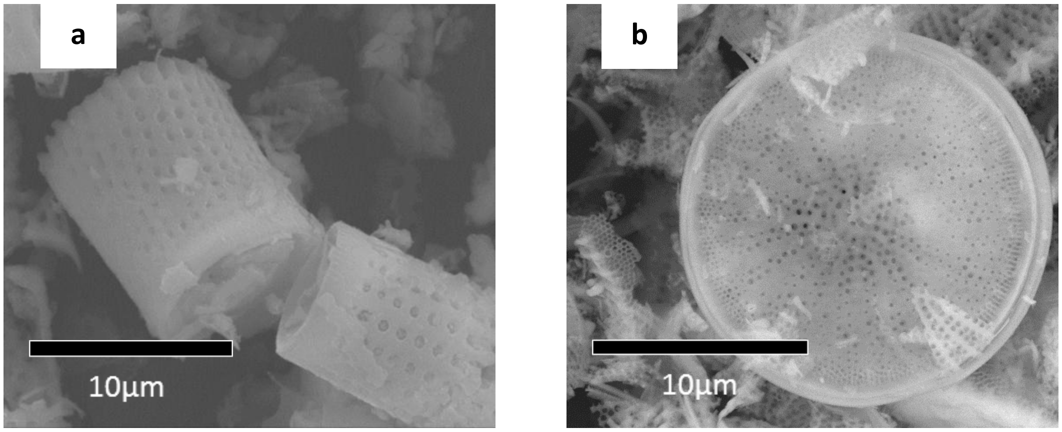

Figure 6.1. (a) Barreled-shaped (b) disc-shaped diatom structures.

The distinct silica frustules of the diatoms structure provide unique mechanical, chemical, optical, and photonic properties.[2,6-9] These properties allow diatomaceous earth (DE) to be used on a wide variety of applications, such as filtration,[10,11] biosensors,[12,13] immunoisolation,[14] superhydrophobic coatings,[15-18] drug carriers,[4,19,20] and heavy metal removal.[21]

Recently diatomite or DE silica has been used for the formation of superhydrophobic applications.[15-18,22] Because of microscale and nanoscale porosity, large surface area, modifiable surface chemistry, non-toxicity, and low cost DE is useful for superhydrophobicity. DE is mainly composed of silicon dioxide (SiO_2), small amounts of alumina (Al_2O_3) and iron oxide (Fe_2O_3), and other minor components.[23] This composition makes DE hydrophilic, which makes it difficult to be used for certain applications such as the superhydrophobicity. However, natural diatomite's pore walls can be chemically functionalized to change the hydrophilicity to hydrophobicity. Chemical modification can be done in the presence of silane coupling agents with different functional groups. A schematic diagram of the proposed modification with presence of organosilanes is shown in Figure 6.2.

Wide ranges of experimental techniques have been developed to study the structure of surface-modified DE with organosilanes. These include scanning electronic microscopy, X-ray fluorescence, X-ray photoelectron spectroscopy, Fourier transform infrared spectroscopy, thermogravimetric analysis, and solid state NMR.[4,24,25]

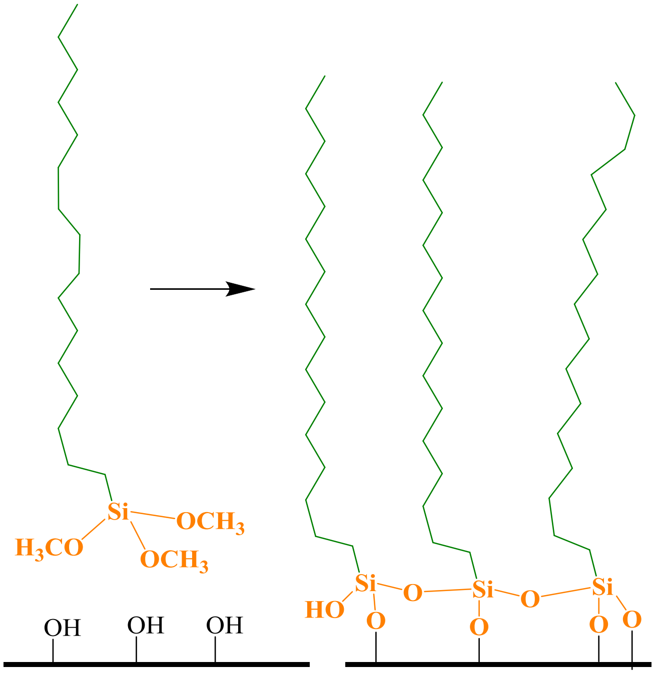

Figure 6.2. Schematic of diatomaceous earth surface modification using organosilanes.

The first objective of the current study was the functionalization of diatom skeletons with organosilanes (R'Si(OR)$_3$) with different adsorbed amounts with the help of a strong organic acid catalyst (*p*-toluenesulfonic acid) together with previously reported reaction conditions to modify the DE.[26] Further objectives were to study the structural aggregation of organosilanes on DE surfaces. DE has a much lower specific surface area than nano-silica particles that we studied previously. Consequently, it is much more difficult to measure the enthalpies of different adsorbed amounts compared to the silica. But, it is important to characterize this system because DE playa an important role in DE coatings. Therefore, in this study, we further try to identify how the structural formations of organosilanes change with the surface morphology of the type of silica. Hexadecyltrimethoxysilane was used as the organosilane to modify the DE. The prepared hexadecyltrimethoxysilane-DE adsorbed samples were characterized by temperaturemodulate differential scanning calorimetry (TMDSC), thermogravimetric analysis (TGA), and Fourier transform infrared spectroscopy (FTIR).

6.3. EXPERIMENTAL

Untreated DE and hexadecyltrimethoxysilane (HDTMS) were obtained from Dry Surface Coatings, (Guthrie, OK) and Gelest, Inc (Morrisville, PA), respectively. The *p*-toluenesulfonic acid monohydrate (PTSA) was purchased from Sigma Aldrich (St. Louis, MO) and toluene from Pharmco-aaper (Brookfield, CT). All chemicals were used as received.

DE (1 g) was separately reacted with different mass fractions of HDTMS in the presence of PTSA (0.02g) as catalyst in separate glass vials with 15 mL of toluene. The reactions were carried out in a mechanical shaker for 4 h at 50 °C in a water bath. After shaking, the solutions were cooled to room temperature. The HDTMS treated DE products were obtained from the reaction medium by passing air through the sample using a Pasteur pipette. The samples were dried under vacuum at 40 °C for 48 h prior to analysis.

The grafted amounts of HDTMS in the treated DE were quantified by TGA using a TA Instruments model TA Q-50 Thermogravimetric Analyzer (TA Instruments, New Castle, DE). The treated DE samples were heated from 20 °C to 900 °C at 20 °C/min under 40 mL/min of continuous nitrogen flow.

The structural features of DE were characterized by scanning electron microscopy (SEM). For SEM studies, DE was spread on the top of an aluminum stud with the help of double-sided sticky tape. The samples were made conductive by sputtering with Au/Pd.

The samples were then imaged using a FEI Quanta 600 SEM (FEI Company, Hillsboro, OR, USA) for SEM micrographs.

TMDSC analysis of treated DE samples were carried out using a Q-2000 (TA Instruments, New Castle, DE). The heating and cooling scans for samples were run from -50 to 120 °C, with a scan rate of 3 °C/min, modulation amplitude of ± 1.0 °C, and a period of 60 s. Because of the supercooling, the heats reported are from the total heat flow curves. The Universal Analysis software package from TA Instruments was used to calculate the enthalpy changes from the area under the heat flow rate curves.

FTIR adsorption spectra were acquired using a Nicolet is 50 FT-IR spectrometer (Thermo Fisher Scientific Inc., Waltham, MA). This instrument was equipped with an ATR accessory with a smart iTR diamond crystal. The scanning range was from 600 to 4000 cm^{-1} with a spectral resolution of 4 cm^{-1} and 64 scans. The spectra were taken by placing small amounts of dry HDTMS adsorbed DE in the cell. A pressure applicator with a torque knob between the cuticle sample and the diamond crystal ensured that the same pressure was applied for all measurements. X-ray diffraction (powder XRD) patterns were obtain on a Bruker AXS Smart APEX diffractometer (Bruker, Billerica, MA) operating with Mo Kα ($\lambda = 0.7107$ Å) radiation.

An exponential model for the enthalpy data was fitted by iterating the values of the fitting parameters until the value of the sum of the squares of the residual was minimized. The uncertainty of the each parameter was estimated by varying each parameter independently from the set of best-fit values until the sum of squares hit the target value, which corresponds to a 95% confidence interval.[27]

6.4. RESULTS

This study used DE composed of mostly disk-shaped diatom shells as shown in Figure 6.3(a). The SEM image (Figure 6.3(a)) shows that the diatom shells are disk-shaped and relatively uniform in diameter (15-20 µm). The diatom shell possesses a highly developed porous structure, with different types of macroporous and mesoporous structures as shown in Figure 6.3(b) and (c).

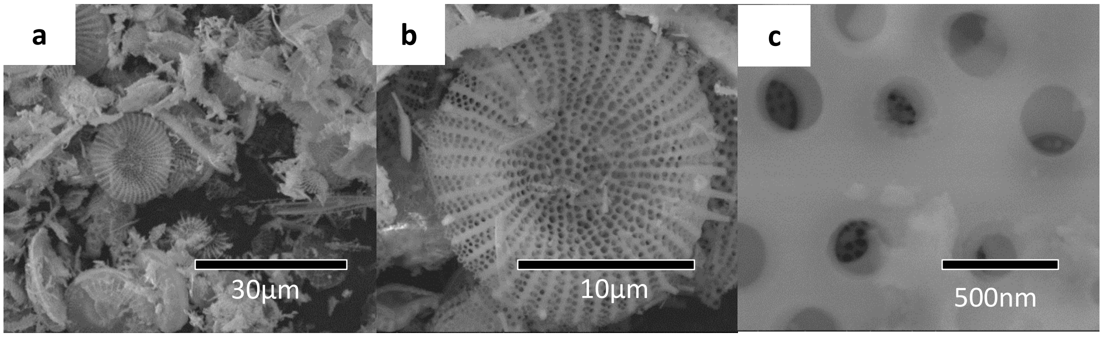

Figure 6.3. SEM images of (a) diatomaceous earth shells (b) macroporous and (c) mesoporous structures of disk-shaped diatomaceous earth.

Asymmetric and symmetric methylene (CH_2) stretching frequencies of HDTMS treated DE samples are plotted in Figure 6.4. As reported previously, symmetric and asymmetric stretching frequencies for crystalline n-alkanes occur around 2850 and 2916 cm^{-1},[28] and liquid like n-alkanes typically occur around 2854-2856 and 2924-2928 cm^{-1}.[29] As shown in Figure 6.4, when the adsorbed amounts were smaller than 1.5 mg/m^2, the asymmetric and symmetric stretching frequencies are around 2926-2922 and 2855-2852 cm^{-1}, respectively. With increasing adsorbed amounts, the stretching frequencies started to decrease and became fairly constant after 6 mg/m^2 and eventually reaching bulk HDTMS with higher adsorbed amounts.

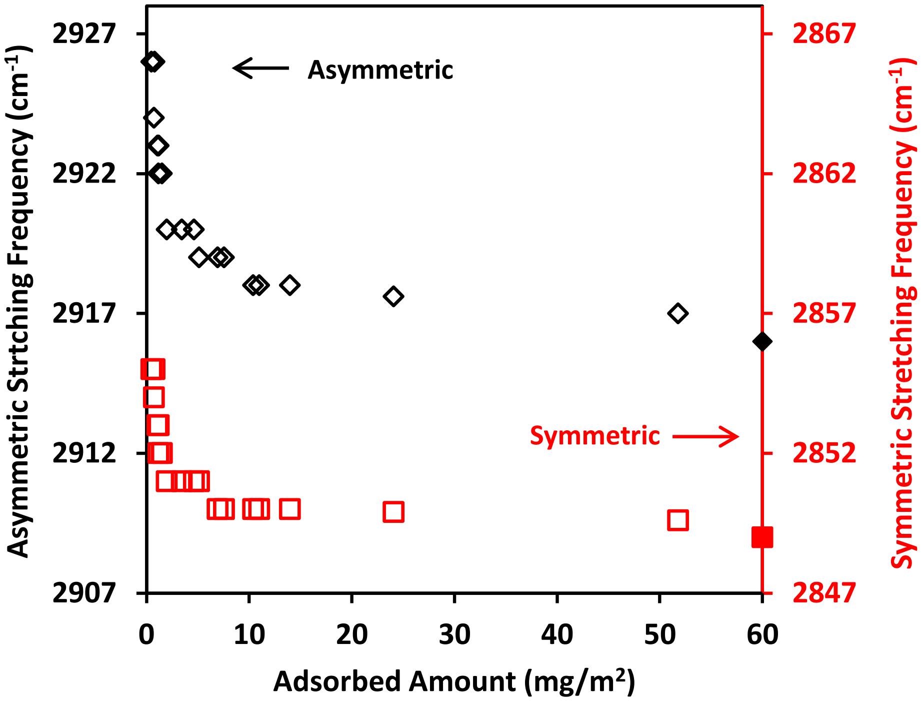

Figure 6.4. Asymmetric (◊) and symmetric (□) vibration frequencies for CH_2 stretches of HDTMS treated DE samples. The values for bulk, crystalline HDTMS, are shown as filled symbols (♦, ■) located at 60 mg/m^2. The experimental uncertainty is less than or equal to about the size of the symbols.

The derivative TGA curves for the different adsorbed amounts of HDTMS on DE and crystalline HDTMS are shown in Figure 6.5. The crystalline HDTMS shows a main peak around 519 °C with a tail on the low temperature side that originates from the amorphous nature or unbound organic molecules.[30-32] DE with PTSA shows two main decomposition temperatures around 460 and 570 °C. As demonstrated on our previous work,[33] the first peak is attributed to the decomposition of PTSA and the high temperature peak is due to the dehydroxylation of the silanols of DE.[34] At very small adsorbed amounts, the higher temperature peak (around 570 °C) started to increase in intensity. This decomposition temperature was higher than the bulk HDTMS. With further increases in the adsorbed amounts, the low temperature peak increased in intensity and the higher temperature peak became overshadowed by the larger signals of the low temperature peak. In the samples with large adsorbed amounts, the derivative mass loss peaks developed into a single peak. With further increases towards the larger adsorbed amounts, the decomposition temperatures shifted to higher temperatures until it reached the bulk HDTMS temperature. The characteristic low temperature side tail on the bulk decomposition was observed in the larger adsorbed amount samples too. It is may due to the material with a significant amorphous fraction of HDTMS molecules.[35]

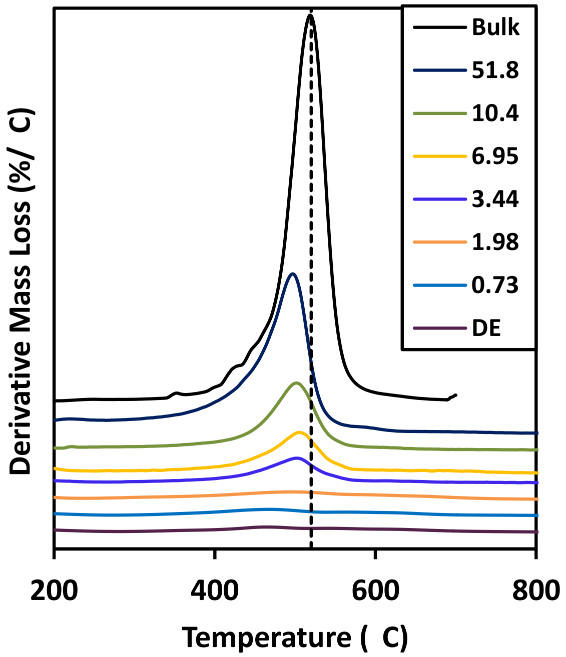

Figure 6.5. Derivative mass loss curves of crystalline and HDTMS adsorbed DE samples. The curves are in the order shown in the legend. The numerical values are the adsorbed amounts in mg_{HDTMS}/m^2 DE.

TMDSC thermograms for melting and crystallization of HDTMS hydrocarbon chains are shown in the Figure 6.6. The vertical scales are adjusted on the thermograms to clarify the transitions of the TMDSC curves. The heating scan of crystalline HDTMS, Figure 6.6(a), exhibited an endothermic peak around 42 °C with a tail to the low temperature side. The cooling scan observed in the Figure 6.6(b), also showed an exothermic peak center around 37 °C with the tail to the lower temperature side. This peak corresponds to the crystallization of HDTMS hydrocarbon chains. The 5 °C difference between the melting and crystallization temperatures indicated that there a supercooling process going on in the crystalline HDTMS. Due to the lack of nucleation sites, crystallization processes in the cooling cycle take place at lower temperatures.[30,31,36]

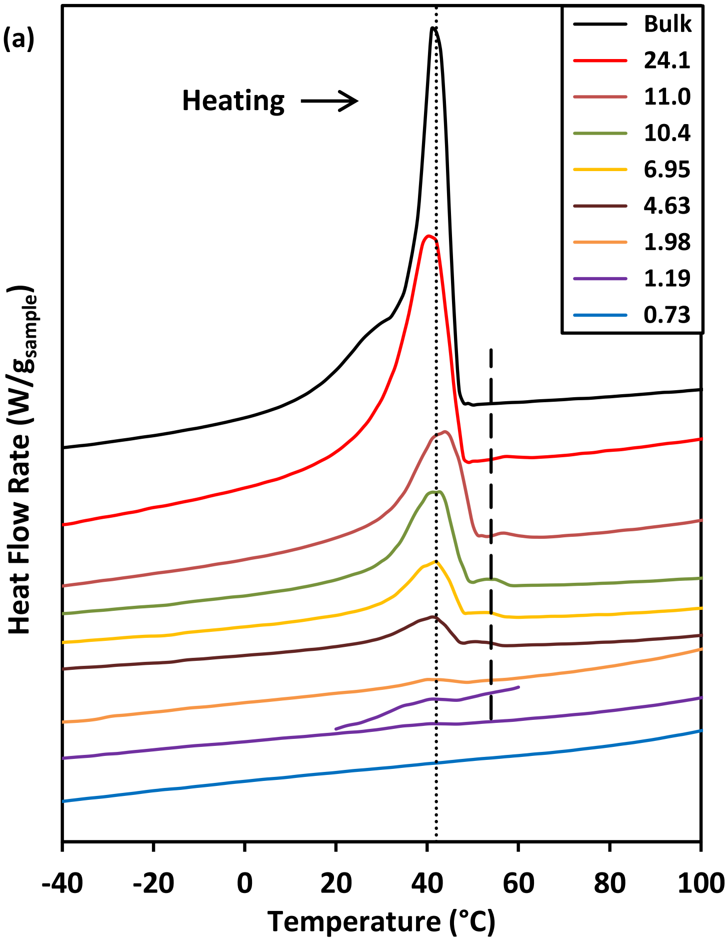

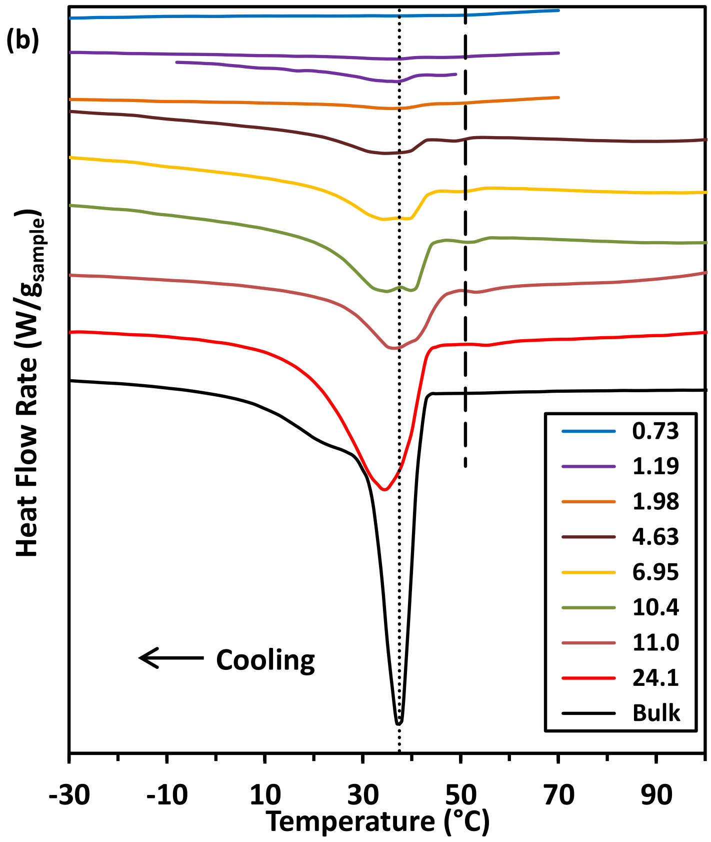

Figure 6.6. Heat flow rates for crystalline and reacted HDTMS samples from the (a) heating scans. and (b) cooling scans with the short trace for the 1.19 mg/m^2 adsorbed amount sample. Dotted lines are indicate the bulk HDTMS melting and crystallization temperature. The numerical values are the reacted amounts in mg HDTMS/m^2 DE and the order as shown in the legend. The bulk HDTMS intensities in the heating and cooling scans were halved to adjust the higher intensity of the curve with the other thermograms. The adsorbed sample thermograms are scaled to make the most prominent components obvious in the figure.

In Figure 6.6(a) for the heating scans, at small adsorbed amounts of HDTMS, a single asymmetric melting peak was centered around 39 °C with small enthalpies. As adsorbed amounts increased, a new peak formed as a shoulder on the higher temperature side with a melting temperature around 40 °C and another new peak at 52 °C (shown as dashed line in the Figure 6.6(a)). With further increases in the adsorbed amount, a new peak formed as a shoulder (40 °C) which tended to dominate and increase the transition enthalpies and overshadowed the lower temperature peak (39 °C). As adsorbed amounts increased, the 40 °C temperature peak moved toward the crystalline melting temperature of HDTMS. A constant peak shape occurred when the adsorbed amounts were greater than 20 mg/m^2, with a melting temperature of 40 °C, which is very close to that of bulk HDTMS melting temperature (42 °C). The heating peak that was centered at 52 °C did not increase intensity with the adsorbed amounts. This peak did not have an equivalent observed on the HDTMS on silica nano particle thermograms.[37] To get more details on this higher temperature peak, further studies are needed to identify the possible factors that influence this peak, such as with different types of DE particles. This higher temperature peak was also not seen with the bulk HDTMS.

In the cooling scans (Figure 6.3(b)), the crystallization transition for the samples with small adsorbed amounts of HDTMS showed a weak peak around 33 °C. As the adsorbed amounts increased, this peak moved to the higher temperature side with increased intensity. At the same time, a separate peak and a shoulder peak started to form at the higher temperature side at 50 °C and 37 °C, respectively. However, the peak centered at 50 °C (shown as dashed line in the Figure 6.6(b)) did not scale up with adsorbed amounts. In addition, the 37 °C peak shifted to 41 °C and started to be overshadowed by the higher intensity of the lower temperature peak at very higher adsorbed amounts.

Melting and crystallization enthalpies of HDTMS chains were calculated using the area under the transition curves of TMDSC thermograms. Since there are no transitions for the DE particles over the temperature range studied, the transition enthalpies for HDTMS were estimated directly from the thermograms. The enthalpies were measured per mass of sample ($\Delta H_{\mathrm{sample}}$). Then the enthalpies were renormalized in order to express enthalpy per gram of HDTMS,

$$\Delta H_{HDTMS} = \Delta H_{sample} \times \frac{m_{sample}}{m_{HDTMS}} \tag{6.1}$$

where $\Delta H_{\mathrm{HDTMS}}$ is the enthalpy change per gram of HDTMS (in J/g), which excludes the contribution from DE.

The enthalpies for melting and crystallization transitions of the HDTMS adsorbed samples are shown in Figure 6.7. The melting and crystallization enthalpies were similar to each other. The enthalpy for bulk HDTMS was 90.0 J/g_{HDTMS} in crystallization and 90.2 J/g_{HDTMS} for melting. At very small adsorbed amounts (< 0.7 mg/m^2), enthalpies were unable to be calculated because the signal to noise ratio was low. With increasing adsorbed amounts, enthalpy started to increase exponentially and reached a relatively constant enthalpy with large adsorbed amounts. It started to flatten around 90 J/g, which was the enthalpy for the bulk crystalline HDTMS.

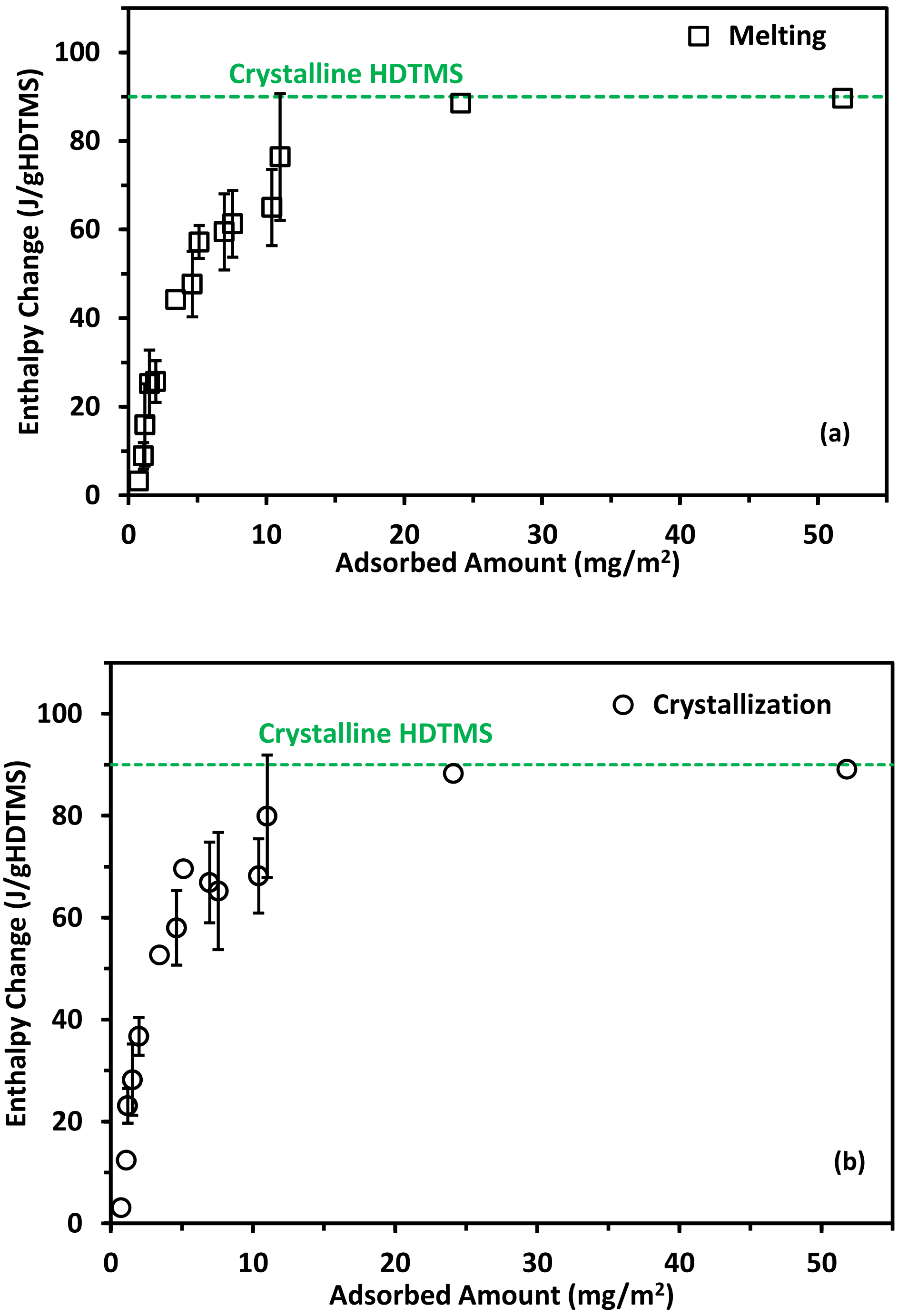

Figure 6.7. Enthalpy change of HDTMS on DE for (a) melting (□) and (b) crystallization (○). Except where shown the error bars, the uncertainties were less than or about the size of the symbol used on the data points.

Powder XRD spectra for bulk condensed HDTMS, adsorbed samples, and untreated DE are shown in Figure 6.8. The samples with the largest adsorbed amount (51.8 mg/m^2) showed a relatively sharp peak, which is very close to bulk HDTMS 2θ value. This indicated that the addition of a lot of HDTMS molecules to DE surface caused the DE to be more crystalline, like the bulk condensed material. Using the Bragg's Law equation ($d = I/(2 \sin \theta)$, $I = 0.7107$ Å) for the $2\theta = 9.6$ peak, d was calculated as 4.6 Å. The calculated d value was able to be assigned to the lateral interchain distance for densely packed alkyl chains (4.1–4.5 Å).[32,38-41] The untreated DE and the 1.98 mg/m^2 adsorbed amount samples contain a very broad peak, due to the amorphous nature of SiO_2 in DE.[42-44] At the same time, the sharp crystalline peak was unable to be observed because at very small HDTMS adsorbed amounts have higher fraction of amorphous material.

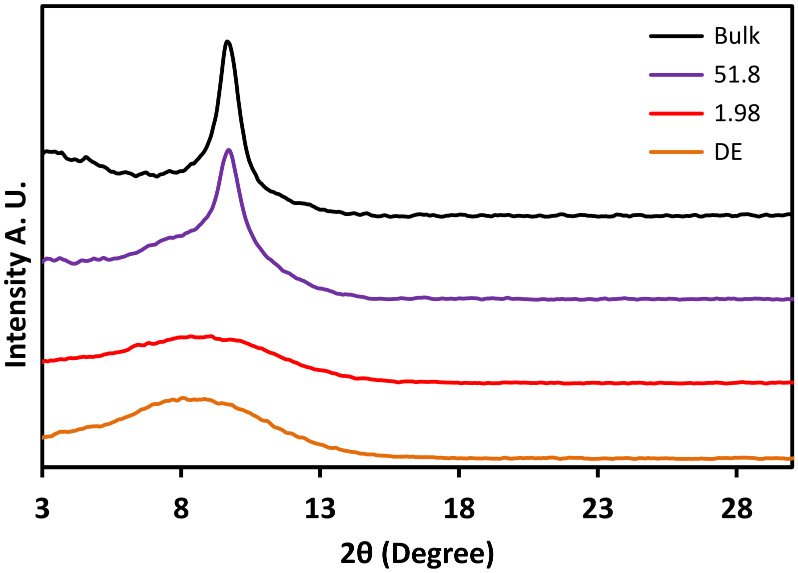

Figure 6.8. Powder XRD spectra of bulk condensed HDTMS, 51.8 and 1.98 mg/m^2 adsorbed DE samples, and untreated DE. The curves are in the order shown in the legend. The numerical values are the adsorbed amounts in mgHDTMS/m^2 DE.

6.5. DISCUSSION

At very small adsorbed amounts (< 1.5 mg/m^2), the asymmetric and symmetric vibrational stretching frequencies of the CH_2s were at a higher frequency compared to the crystalline HDTMS in Figure 6.4. FTIR can detect the molecular structures and dynamics of hydrocarbon chains.[28,45-48] Based on the CH_2 stretching frequencies, bulk crystalline HDTMS hydrocarbon chains are highly ordered and have all trans conformations. At small adsorbed amounts, CH_2 symmetric and asymmetric stretching frequencies lie in between 2855-2852 cm^{-1} and 2926-2922 cm^{-1}. These higher CH_2 frequencies confirms large number of hydrocarbon segments on HDTMS were in gauche conformations.[49] Therefore, when the adsorbed amounts were less than 1.5 mg/m^2, the hydrocarbon chains were more disordered. At the same time, these samples had very small enthalpies of melting and crystallization, and they were unable to be detected in the TMDSC experiments. The reason for this is that the molecules may be far enough apart from each other or the chains not line up well enough to have any significant amount of crystallinity. At large adsorbed amounts, the CH_2 frequencies were closer to the bulk HDTMS value. This is because HDTMS hydrocarbon chains started to form well-ordered structures on the DE surface like crystalline HDTMS. This effect increased the melting and crystallization enthalpies of the sample due to the larger number of interactions between the hydrocarbon chains.

The decomposition temperatures of a substances in TGA can be a very useful tool for the identification of the nature of the structure. When the adsorbed amount was less than 2 mg/m^2, (Figure 6.5) higher decomposition temperatures were observed from adsorbed DE samples. This decomposition temperature was higher for the small adsorbed amount samples than the crystalline HDTMS decomposition temperature. This was a result of the direct attachment of HDTMS silane molecules on to the surface.[28,31] With increased adsorbed amounts, more oligomers are formed patchwise on the surface,[50] and decomposition temperature moved lower. At larger adsorbed amounts, as the FTIR results confirm, hydrocarbon chains were more highly crystalline (trans-trans conformation). As a result, the decomposition temperatures approached the crystalline HDTMS.

The melting and crystallization enthalpies for adsorbed samples increased with adsorbed amount as shown in Figure 6.6. This enthalpy increment occurs exponentially with the adsorbed amount. Once the samples had more than 20 mg/m^2 of silane, enthalpies were reached the bulk HDTMS enthalpy value due to the formation of crystalline material. Lower enthalpy values at the small adsorbed amounts were consistent with the notion that these molecules are randomly distributed on the surface. These molecules were far apart from each other and did not have the interactions to give higher enthalpies. Therefore, molecules are more disordered at small adsorbed amounts, and more arranged structures start to form with increasing adsorbed amount.

Enthalpy changes indicate the structural arrangement on each surface. So to get a realistic picture of how HDTMS molecules arrangement change on the surface of DE, we tested the enthalpy data with two models as in previous developed studies.[30] They were the *two-state model* and *multilayer model*. The two-state model was based on the surface bound "monolayer-like" and "bulk-like" structures. According to our previous study in HDTMS on silica, "monolayer-like" enthalpy showed a linear relationship with adsorbed amount. Molecules arranged beyond the "monolayer-like" structures are referred to as "bulk-like". Bulk like material added constant enthalpy (ΔH_{bl}) with increasing adsorbed amount. The total enthalpy for the total adsorbed HDTMS layers, $\Delta H_{\mathrm{HDTMS}}$, was calculated using Equation 6.2,[30]

$$\Delta H_{HDTMS} = \frac{m_1 \Delta H_1 + m_{bl} \Delta H_{bl}}{M_{HDTMS}} \tag{6.2}$$

where m_1 and m_{bl} are the masses of the HDTMS in the monolayer and bulk-like HDTMS on 1 m^2 of DE surface, and M_{HDTMS} is the total mass for HDTMS.

When DE surfaces were modified with small adsorbed amounts, HDTMS molecules tend to attach randomly on the surface. Therefore, these molecules were relatively flat on the surface due to the lack of interactions between the neighboring molecules. This lead to the very low enthalpy values as were observed on the TMDSC. Consistent with previous studies,[30,37] the enthalpy increased linearly with adsorbed amount, or

$$\Delta H_1 = A m_1 \tag{6.3}$$

where A is the slope parameter. As observed on FTIR, TGA, and TMDSC results, at small-adsorbed amounts molecules are random and disordered. As the adsorbed amount increased, oligomers started to form with elongated chains, as they were located further away from the surface. Molecules were continuously added until a "monolayer-like" structure was formed. In both models, the total adsorbed amount of HDTMS at the "monolayer-like" coating is refered to as m_1'. In the monolayer region both models behave similarly.

The multilayer model is another way to model the development of enthalpy with adsorbed amount. The first part is "monolayer-like", where enthalpies increase linearly.

In the second part of the model, enthalpies have exponential dependence with adsorbed amount, starting at enthalpy values at the end of the linear part of the enthalpy.

$$\Delta H_{HDTMS} = \frac{m_1 \Delta H_1 + m_{ml} \Delta H_{ml}}{M_{HDTMS}} \qquad (6.4a)$$

$$\Delta H_{HDTMS} = \ m_1 \Delta H_1 \ / M_{HDTMS} \quad \text{(for sub- and monolayer, } 0 \leq m_1 \leq m_1'\text{)} \qquad (6.4b)$$

where m_1 and m_{ml} are the masses of the HDTMS in the monolayer and multilayer HDTMS on 1 m^2 of DE surface, respectively, and M_{HDTMS} is the total mass for HDTMS. The total enthalpy for the multilayer and the expanded format of the integrated equation is given by equation 6.4c and 6.4d respectively:

$$\Delta H_{HDTMS} = \ m_1' \Delta H_1 + \ {}_{m_1'}^{m_1} \ \Delta H_1 + \Delta H_2 \ \ 1 - e^{-x/a} \quad dx \ \ / M_{HDTMS} \quad \text{(for } m_1 \geq m_1'\text{)} \qquad (6.4c)$$

$$\Delta H_{HDTMS} = \ m_1' \Delta H_1 + \ m_1 - m_1' \quad m_1' A + \Delta H_2 \quad + \ \Delta H_2 a e^{\frac{- \ m - m_1'}{a}} \quad - 1 \ \ / M_{HDTMS} \qquad (6.4d)$$

where a is the exponential constant, which describes the growth of the "bulk like" behavior with adsorbed amount.

For the behavior of adsorbed HDTMS on silica, in our previous study, we observed a linearly increasing enthalpy in the "monolayer-like" region. However, with HDTMS on DE, we were unable to measure enthalpy changes at very small adsorbed amounts. This was likely due to the smaller specific surface area (specific surface area of DE is 24 m^2/g) and the different surface curvature of DE, compared to the silica (130 m^2/g). With a changing nature of the surface curvature, arrangement of same organosilane coupling agent may differ.[51] As noted, we did not observe any enthalpy values at smaller adsorbed amounts, probably due to the low surface area of DE. From the adsorption of HDTMS on silica, only limited enthalpy values were obtained at the smaller adsorbed amounts, such as at 0.38 mg/m^2, the enthalpy was 1.13 J/g; at 0.5 mg/m^2, the enthalpy was 1.0 J/g; and at 0.63 mg/m^2, enthalpy was 1.6 J/g. Using the multilayer model of DE with a "monolayer-like" (linear part) portion, a linear portion was force fitted to go to zero creating slight curvature at the beginning of curve. This is an artifact that was unavoidable because nearly enthalpies could not be measured in the smaller adsorbed amount region. The linear slope of the multilayer model is sensitive to the enthalpy values of small adsorbed amounts. These data were able to be fit with an a modified multilayer model which is shown in equation 6.5,

$$\Delta H_{HDTMS} = \;{}_{0}^{m_1} \Delta H_2 \;\; 1 - e^{-x/a} \quad dx \;\;/M_{HDTMS} \qquad (6.5)$$

The results of fitting the enthalpy data to model is shown in Figure 6.9 and the fitted parameters are shown in Table 6.1. With the best fit parameters to the modified multilayer model, $\Delta H_2 = \Delta H_{\mathrm{HDTMS}}$ = 97.2 J/g and a = 2.9 mg/m^2. The maximum enthalpy 97.2 J/g was obtained when the adsorbed amount approached to the infinity. This was close to the bulk HDTMS enthalpy value of 90.0 J/g. According to the two-state model of HDTMS adsorbed system composed of "monolayer-like" and "bulk-like" structures. However, with DE "monolayer-like" structure enthalpies were unable measure. Therefore, DE and HDTMS enthalpies were unable to fit with two-state model.

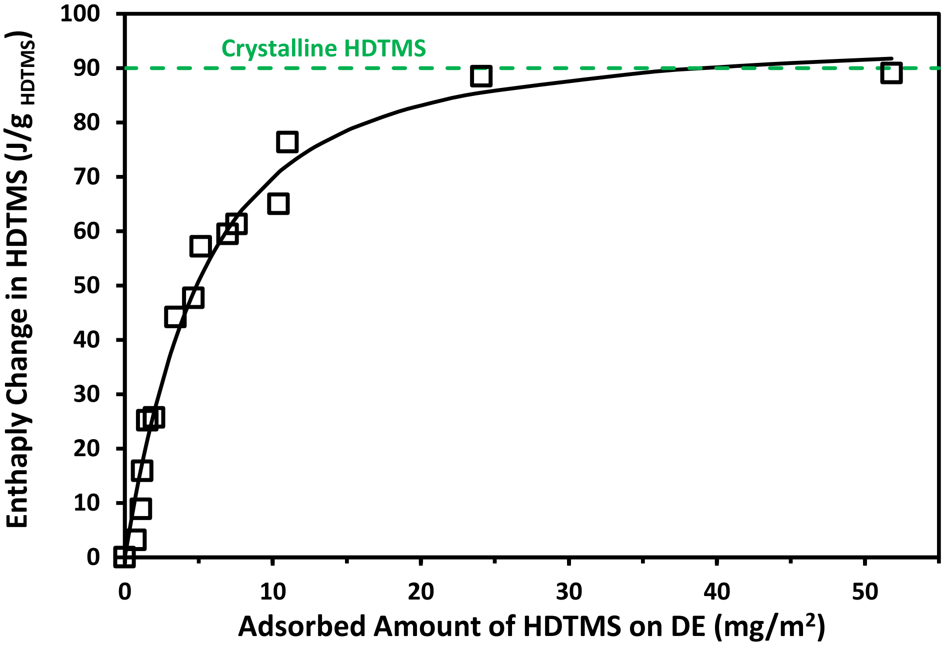

Figure 6.9. Enthalpy of melting of adsorbed HDTMS as a function of adsorbed amount showing the fit from the modified *multilayer model*. The horizontal dashed line shows the enthalpy for the bulk condensed HDTMS.

Table 6.1. Fitting Parameters for the Enthalpy Multilayer Model for Adsorbed HDTMS on DE.

model	**ΔH_{ml} (J/g)**	**a (mg/m^2)**	**S.D.***
multilayer	97.2 (±6.1)	2.9 (±0.5)	4.0

* SD is the standard deviation of the residuals from the fits to the models.

The type of silica surface used has a significant influence on the structural arrangement of HDTMS at small adsorbed amounts. With respect to the nano silica particles (cab-o-sil LM130), clearly we were able to see linear increase in enthalpy with increasing adsorbed amount. However, with DE, even though it is mainly composed of silica, we did not see the linear increase with the smaller adsorbed amounts. At further increased adsorbed amounts, enthalpy started to increase exponentially, independent of the type of surface used. To sum up, at small-adsorbed amounts the structural arrangement of HDTMS depends on the type of silica substrate used, and at lager adsorbed amounts the system is independent of the type of silica surface used and adsorbed HDTMS reaches to the bulk like behavior.

6.6. CONCLUSIONS

Structural arrangements of HDTMS on the surface of DE was probed with TMDSC, FTIR, TGA, and XRD. FTIR and XRD the results confirmed at small adsorbed amounts, HDTMS molecules are amorphous on the surface and did not form a "monolayer-like" structure. At further increased adsorbed amounts ordered structures start to form with higher crystallinity. The higher decomposition temperatures in TGA at small adsorbed amounts indicate molecules are directly attached on to the surface and flat. Enthalpy data at different adsorbed amounts were able to be fit with the modified multilayer model. According to this model, the enthalpy increases exponentially and is able to reach the bulk HDTMS value with higher adsorbed amount.

6.7. ACKNOWLEDGEMENTS

The authors thank Dr. Reza Latifi for measuring the powder XRD for the HDTMS adsorbed silica samples and the financial support of the Dry Surface Coating Guthrie, OK and the Oklahoma State University.

6.8. REFERENCES

(1) Măruţoiu, O. F.; Bratu, I.; Hodişan, S.; Tigae, C. *Croat. Chem. Acta* **2014**, *87*, 1.

(2) Gordon, R.; Losic, D.; Tiffany, M. A.; Nagy, S. S.; Sterrenburg, F. A. S. *Trends Biotechnol.* **2009**, *27*, 116.

(3) Scala, S.; Bowler, C. *CMLS, Cell. Mol. Life Sci.* **2001**, *58*, 1666.

(4) Kumeria, T.; Bariana, M.; Altalhi, T.; Kurkuri, M.; Gibson, C. T.; Yang, W.; Losic, D. *J. Mater. Chem. B* **2013**, *1*, 6302.

(5) Lettieri, S.; Setaro, A.; De Stefano, L.; De Stefano, M.; Maddalena, P. *Adv. Funct. Mater.* **2008**, *18*, 1257.

(6) Sumper, M.; Brunner, E. *Adv. Funct. Mater.* **2006**, *16*, 17.

(7) Parkinson, J.; Gordon, R. *Trends Biotechnol.* **1999**, *17*, 190.

(8) Lopez, P. J.; Desclés, J.; Allen, A. E.; Bowler, C. *Curr. Opin. Biotechnol.* **2005**, *16,* 180.

(9) Losic, D.; Mitchell, J. G.; Voelcker, N. H. *Adv. Mater.* **2009**, *21*, 2947.

(10) Ongerth, J. E.; Hutton, P. *J. Am. Water Works Assoc.* **1997**, *89*, 39.

(11) Schuler, P. F.; Ghosh, M. M.; Gopalan, P. *Water Res.* **1991**, *25*, 995.

(12) Dempsey, E.; Diamond, D.; Smyth, M. R.; Urban, G.; Jobst, G.; Moser, I.; Verpoorte, E. M.; Manz, A.; Widmer, H. M.; Rabenstein, K. *Anal. Chim. Acta* **1997**, *346*, 341.

(13) Meyer, H.; Drewer, H.; Gruendig, B.; Cammann, K.; Kakerow, R.; Manoli, Y.; Mokwa, W.; Rospert, M. *Anal. Chem.* **1995**, *67*, 1164.

(14) Desai, T. A.; Chu, W. H.; Tu, J. K.; Beattie, G. M.; Hayek, A.; Ferrari, M. *Biotechnol. Bioeng.* **1998**, *57*, 118.

(15) Oliveira, N. M.; Reis, R. L.; Mano, J. F. *ACS Appl. Mater. Interfaces* **2013**, *5*, 4202.

(16) Polizos, G.; Winter, K.; Lance, M. J.; Meyer, H. M.; Armstrong, B. L.; Schaeffer, D. A.; Simpson, J. T.; Hunter, S. R.; Datskos, P. G. *Appl. Surf. Sci.* **2014**, *292*, 563.

(17) Sedai, B. R.; Khatiwada, B. K.; Mortazavian, H.; Blum, F. D. *Appl. Surf. Sci.* **2016**, *386*, 178.

(18) Perera, H. J.; Khatiwada, B. K.; Paul, A.; Mortazavian, H.; Blum, F. D. *J. Appl. Polym. Sci.* **2016**, *133*, 44072.

(19) Milović, M.; Simović, S.; Lošić, D.; Dashevskiy, A.; Ibrić, S. *Eur. J. Pharm. Sci.* **2014**, *63*, 226.

(20) Aw, M. S.; Bariana, M.; Yu, Y.; Addai-Mensah, J.; Losic, D. *J. Biomater. Appl.* **2013**, *28*, 163.

(21) Bello, O. S.; Adegoke, K. A.; Oyewole, R. O. *Sep. Sci. Technol.* **2014**, *49*, 1787.

(22) Puretskiy, N.; Chanda, J.; Stoychev, G.; Synytska, A.; Ionov, L. *Adv. Mater. Interfaces* **2015**.

(23) Al-Ghouti, M. A.; Khraisheh, M. A. M.; Allen, S. J.; Ahmad, M. N. *J. Environ. Manage* **2003**, *69*, 229.

(24) Fowler, C. E.; Buchber, C.; Lebeau, B.; Patarin, J.; Delacôte, C.; Walcarius, A. *Appl. Surf. Sci.* **2007**, *253*, 5485.

(25) Huttenloch, P.; Roehl, K. E.; Czurda, K. *Environ. Sci. Technol.* **2001**, *35*, 4260.

(26) García, N.; Benito, E.; Guzmán, J.; Tiemblo, P. *J. Am. Chem. Soc.* **2007**, *129*, 5052.

(27) Motulsky, H.; Christopoulos, A.; OUP USA: San Diego, CA, 2004, p 109.

(28) Osman, M. A.; Ernst, M.; Meier, B. H.; Suter, U. W. *J. Phys. Chem. B* **2002**, *106*, 653.

(29) Parikh, A. N.; Liedberg, B.; Atre, S. V.; Ho, M.; Allara, D. L. *J. Phys. Chem.* **1995**, *99*, 9996.

(30) Zhang, T.; Xu, G.; Puckette, J.; Blum, F. D. *J. Phys. Chem. C* **2012**, *116*, 11626.

(31) Osman, M. A.; Seyfang, G.; Suter, U. W. *J. Phys. Chem. B* **2000**, *104*, 4433.

(32) Dhôtel, A.; Li, H.; Fernandez-Ballester, L.; Delbreilh, L.; Youssef, B.; Zeng, X. C.; Tan, L. *J. Phys. Chem. C* **2011**, *115*, 10351.

(33) Perera, H. J.; Mortazavian, H.; Blum, F. D. *To be submitted* **2016**.

(34) Katsumata, H.; Kaneco, S.; Suzuki, T.; Ohta, K. *Anal. Chim. Acta* **2006**, *577*, 214.

(35) Ni, L.; Rigolet, S.; Chemtob, A.; Croutxé-Barghorn, C.; Brendlé, J.; Vidal, L. *Comptes Rendus Chimie* **2013**, *16*, 897.

(36) Zhang, S.; Wu, J.-Y.; Tse, C.-T.; Niu, J. *Solar Energy Materials and Solar Cells* **2012**, *96*, 124.

(37) Perera, H. J.; Blum, F. D. *To be submitted* **2016**.

(38) Ungar, G. *J. Phys. Chem.* **1983**, *87*, 689.

(39) Doucet, J.; Denicolo, I.; Craievich, A.; Collet, A. *J. Chem. Phys* **1981**, *75*, 5125.

(40) Ni, L.; Chemtob, A.; Croutxé-Barghorn, C.; Brendlé, J.; Vidal, L.; Rigolet, S. . *Mater. Chem.* **2012**, *22*, 643.

(41) Parikh, A. N.; Schivley, M.; Koo, E.; Seshadri, K.; Aurentz, D.; Mueller, K.; Allara, D. *J. Am. Chem. Soc.* **1997**, *119*, 3135.

(42) Li, S.; Li, D.; Su, F.; Ren, Y.; Qin, G. *Appl. Surf. Sci.* **2014**, *317*, 724.

(43) Cabrera, M.; Maciel, J.; Quispe-Marcatoma, J.; Pandey, B.; Neri, D.; Soria, F.; Baggio-Saitovitch, E.; de Carvalho Jr, L. In *LACAME 2012*; Springer: 2013, p 191.

(44) Aw, M. S.; Simovic, S.; Yu, Y.; Addai-Mensah, J.; Losic, D. *Powder Technol.* **2012**, *223*, 52.

(45) Snyder, R. G.; Hsu, S. L.; Krimm, S. *Spectrochimica Acta Part A: Molecular Spectroscopy* **1978**, *34*, 395.

(46) Dubois, L. H.; Zegarski, B. R.; Nuzzo, R. G. *J. Am. Chem. Soc.* **1990**, *112*, 570.

(47) Bardeau, J.-F.; Parikh, A. N.; Beers, J. D.; Swanson, B. I. *J. Phys. Chem. B* **2000**, *104*, 627.

(48) Snyder, R. G.; Strauss, H. L.; Elliger, C. A. *J. Phys. Chem.* **1982**, *86*, 5145.

(49) Venkataraman, N.; Vasudevan, S. *J. Phys. Chem. B* **2002**, *106*, 7766.

(50) Daniels, M. W.; Francis, L. F. *J. Colloid Interface Sci.* **1998**, *205*, 191.

(51) Bernardoni, F.; Kouba, M.; Fadeev, A. Y. *Chem. Mater.* **2007**, *20*, 382.

CHAPTER VII

COMPETITION OF HEXAMETHYLTRIMETHOXYSILANE AND P-TOLUENESULFONIC ACID ON SILICA AND DIATOMACEOUS EARTH

7.1. ABSTRACT

Silica and diatomaceous earth (DE) were modified with hexadecyltrimethoxysilane (C16-TMS) in the presence of p-toluenesulfonic acid (PTSA). PTSA acted as an acid catalyst for the reaction of C16-TMS, however, the acid's presence complicated the determination of the adsorbed amount of the silane. Silanol groups on silicas and DE allowed the sulfonate groups on PTSA to attach to the surfaces and these surface-adsorbed acid groups did not come off the surfaces until higher temperatures, overlapping with the decomposition of the silane. We propose a model for the estimation of the amount of silane under "no-rinse" conditions based on the co-adsorption of the acid and silane. Both the acid and silane adsorb on the surface with the silane prefentially adsorbing and the PTSA filling the remainder of the surface sites. This model allows the accurate determination of the amounts of C16-TMS on these two silicas.

7.2. INTRODUCTION

Silane coupling agents are composed of organic and inorganic moieties in the same molecule. This important property means that silane coupling agents can combine two dissimilar materials. Of these two materials, one member is usually composed of a metal oxide-like material, including silicates, borates, aluminates, titanates, etc.[1,2] For example, silane coupling agents can be used to improve the reinforcement of composites and for resin and surface modification. Considerable synthetic effort has been devoted to modifying the surface of silica using silane coupling agents.[3] Silanes can be anchored onto a silica surface through covalent bonds between the hydrolyzed silanes and hydroxyl groups of the silica. These covalent bonds allow the long-lasting immobilization of organic groups and introduce higher stability.[4]

Alkyltrimethoxysilanes [$R\text{-}Si(OCH_3)_3$] are one of the most effective and most widely used coupling agents for the modification of surfaces. The methoxy/ethoxy or chlorine (R-) groups can hydrolyze in the presence of an acid catalyst to form silanols. The alkylation of silanol groups on silica is most frequently done under acid catalyzed reaction conditions with the help of organic and inorganic acids (p- toluenesulfonic acid, hydrochloric acid, ethanol, and methanol). Bases can also be used in many cases. With the presence of catalysts, the surface reactions can be done in a short time and result in higher grafted densities. It is well known that *p*-toluenesulfonic acid (PTSA) is a convenient, easily available and inexpensive material, which can be used in a variety of reactions. These uses include as dopants for conductive polymers,[5] dehydrating agents, [6] catalysts[7], and intermediates for the production of many useful chemicals such as pcresol. The modification of silica with alkyltrimethoxysilanes can be made with PTSA to control adsorption on the silanol.[8]

PTSA is able to remain active for a long period of time as an acid without losing its activity after entrapment or adsorption onto silica or silica-like surfaces, such as in the production of olefin,[6] esters[9], and ZnO particles.[10] These adsorbed PTSA molecules were able to be quantitatively removed with washing with a polar solvent (water, methanol, ethanol).[10] In this study, the surface modification of silica was made at different adsorbed hydrocarbon amounts of the alkyltrimethoxysilane in the presence of PTSA as an acid catalyst. At the end of the reaction, in this case, the modified samples were not washed with polar solvents to avoid the removal of adsorbed hydrocarbon chains and to achieve higher adsorbed amounts. Therefore, we were unable to directly quantify the adsorbed hydrocarbon amounts of the alkyltrimethoxysilane on the surface due to the presence of PTSA. The main objective of this work was to determine the adsorbed hydrocarbon amount of alkyltrimethoxysilane and PTSA. Cab-O-Sil LM130 and diatomaceous earth (DE) were used as our surfaces and were modified with hexadecyltrimethoxysilane (C16-TMS).

7.3. EXPERIMENTAL

Cab-O-Sil (LM130, specific surface are 130 m^2/g) silica and DE (specific surface area 24 m^2/g) were obtained from Cabot Corporation (Billerica, MA) and Dry Surface Coatings (Guthrie, OK). The C16-TMS was from Gelest Inc. (Morrisville, PA), PTSA was from SigmaAldrich (St. Louis, MO), and toluene was from Pharmco-aaper (Brookfield, CT). All chemicals were used as received.

7.3.1. Silylation reaction

A series of silica and DE treated samples with varying adsorbed hydrocarbon amounts of C16-TMS were prepared in toluene. Silica (0.5 g) or DE (1 g) was placed in a glass vial, 15 mL of toluene was added, and the mixtures were shaken with a mechanical shaker for 30 min to wet the particles. PTSA monohydrate (~ 0.02 g) and different amounts of C16-TMS were added to each vial.

The glass vials containing silica and DE with C16-TMS solutions were shaken using a mechanical shaker for 4 h in a 50 °C in a water bath and then cooled down to room temperature. The C16-TMS/PTSA functionalized silica and DE samples were obtained from the reaction medium by passing air through the samples using Pasteur pipettes, followed by drying under vacuum at 50 °C for 48 h. This process did not remove much, if any PTSA.

7.3.2. Surface Characterization

The adsorbed hydrocarbon amounts of C16-TMS in the treated silica and DE were quantified using thermogravimetric analysis (TGA) with a Q-50 Thermogravimetric Analyzer (TA Instruments, New Castle, DE). The samples were heated from 20 °C to 700 °C and 20 °C to 900 °C for silica and DE, respectively, at a heating rate of 20 °C/min under a 40 mL/min of continuous nitrogen flow. The amounts of adsorbed C16-TMS are reported as the adsorbed hydrocarbon amounts. This is the amount of material which decomposed when the samples were heated to 700 °C or 900 °C. It includes the hydrocarbon chains, but not the Si and O's from the coupling agent as they remained on the silicas at the highest temperature. Fourier transform infrared spectroscopy (FT-IR) spectra were taken in transmission mode using a Varian 800 FT-IR spectrometer placing small amount of dry treated and untreated silica and DE on NaCl plates. The scanning range was from 600 cm^{-1} to 4000 cm^{-1} with a spectral resolution of 4 cm^{-1} and 64 scans.

7.4. RESULTS

The TGA curves of untreated silica and DE without PTSA are shown in Figures 7.1(a) and 7.1(c) and those of untreated silica and DE with PTSA in Figures 7.1(b) and 7.1(d). In order to observe the decomposition behavior clearly, the derivative of the mass loss was plotted on the same graph. Untreated silica without PTSA did not show any significant mass loss from 0 °C to 700 °C, but, with PTSA, gave a well-resolved peak around 540 °C with a mass loss of around 3.3%. Derivative curves of both untreated DE without and with PTSA showed peaks in the temperature range of 20 °C -250 °C, centered at around 160 °C. In DE, both with and without PTSA, a significant broad mass loss occurred in the range of 250 °C -900 °C, with a mass loss of around 2.4%[11] and 4.4%, respectively. Untreated DE with PTSA Figure 7.1(d) gave a well resolved peak around 500 °C in addition to the other peaks present on untreated DE. Based on the testing of a large number of samples, the peaks centered on 500 °C and 540 °C were attributed to the decomposition of PTSA on DE and silica. The mass loss differences between the samples with and without PTSA on the surface were due to PTSA (between Figure 7.1(a) and (b) and between Figure 7.1(c) and (d)).

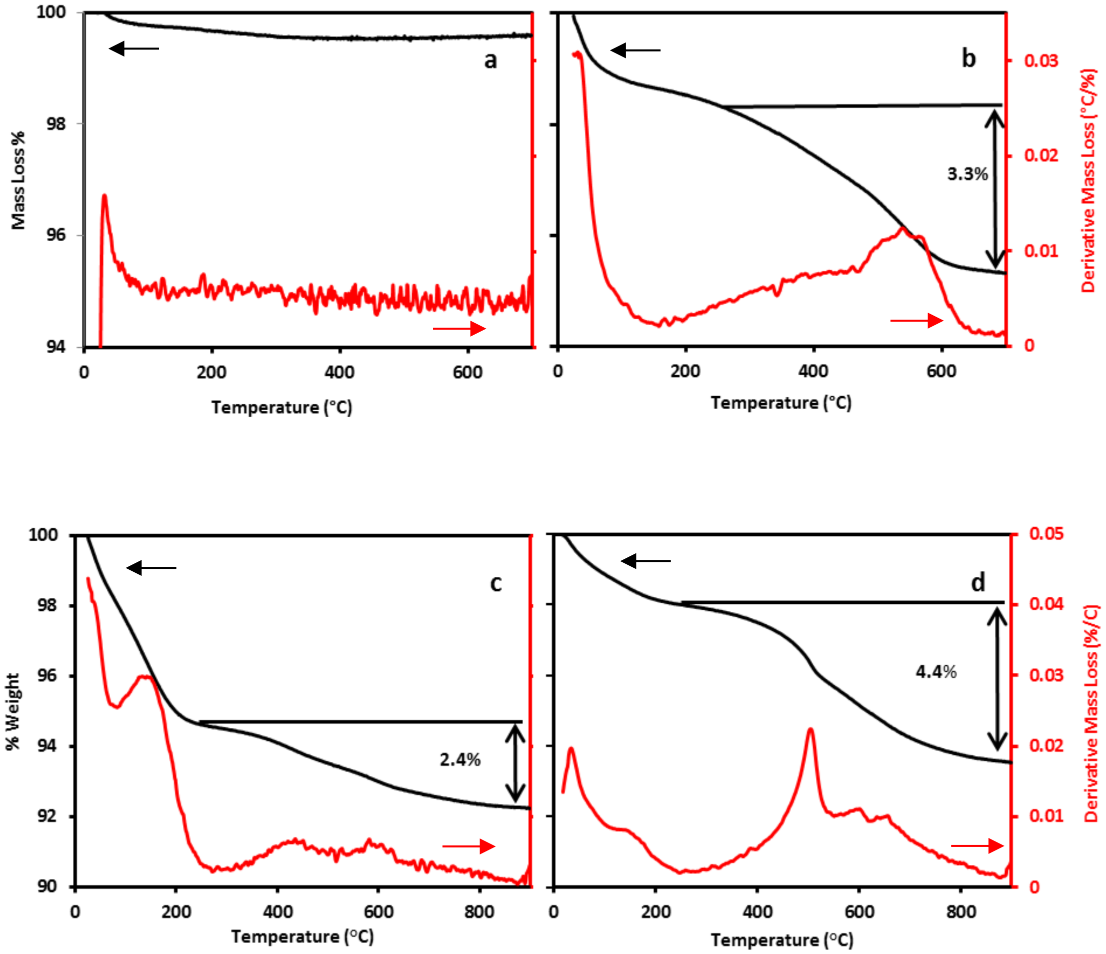

Figure 7.1. TGA curves of untreated silica (a) without and (b) with PTSA (0.27 mg/m^2), and untreated DE (c) without (d) with PTSA (0.92 mg/m^2). Difference between the mass loss of silica with and without PTSA and DE with and without PTSA gave the initial PTSA adsorbed amount.

The TGA thermograms were used to determine the amount of adsorbed silane on the surfaces. C16-TMS treated silica and DE samples showed decomposition steps from 250 °C -700 °C and 250 °C -900 °C, respectively. These peaks, shown in the derivative mode were very broad TGA peaks in Figure 7.2. The PTSA with untreated silica and DE showed a narrower peak in the same temperature range. The overlapping decomposition ranges of PTSA and adsorbed silane can be clearly seen in Figure 7.2. Due to the overlap of the decomposition temperatures of these samples, we were unable to quantify the adsorbed hydrocarbon amounts of C16-TMS directly on the surfaces of silica and DE.

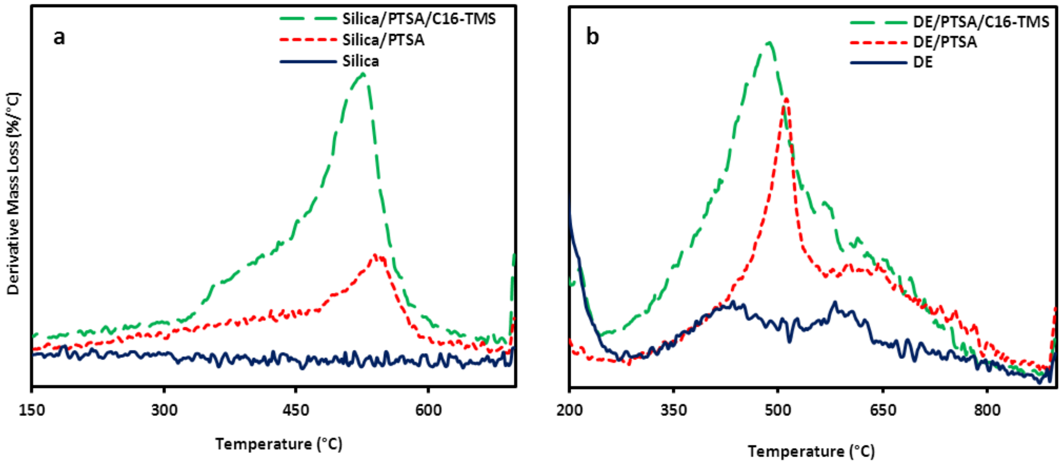

Figure 7.2. Derivative mass loss TGA curves of (a) untreated silica (continuous line), untreated silica with 0.27 mg/m^2 PTSA (dashed line), and 0.4 mg/m^2 C16-TMS hydrocarbon chain adsorbed amount silica with 0.27 mg/m^2 PTSA (dotted line). (b) untreated DE (continuous line), untreated DE with 0.92 mg/m^2 PTSA (dashed line), and 1.6 mg/m^2 C16-TMS hydrocarbon chain adsorbed amount DE with 0.92 mg/m^2 PTSA (dotted line).

Most of the sulfonate stretching bands are located in the 1000 cm^{-1} – 1200 cm^{-1} region.[12] An example is the S=O asymmetric stretch which occurs around 1031 cm^{-1}.[13] In our systems, the broad Si-O stretching band overshadowed the S=O stretching peaks, thus they could not be seen in the FTIR spectra. Aromatic CH$_2$ bending frequencies (Figure 7.3(b)) and some strong bands related to the PTSA (Figure 7.3(c)) were located around 670 - 900 cm^{-1}and 1330 - 1420 cm^{-1}.[14-16] These peaks could be clearly seen in

Figure 7.3 with silica and PTSA, as well as on the C16-TMS treated silica. None of the peaks were seen in the spectra of silica alone. The FTIR results confirmed the adsorption of PTSA on the surface of silica. The broad band at 3400 cm^{-1} was attributed to the silanol O-H stretch. In addition, bands at 1630, 1080, and 800 cm^{-1} correspond to –OH bending, Si-O-Si stretching, and Si-O-Si bending respectively. C16-TMS treated silica showed symmetric and asymmetric CH_2 peaks around 2850 and 2922 cm^{-1}. FTIT result for DE is given in the **Supporting Information S7.1**. The spectra of DE are similar in the FTIR but not as clear, probably due to the much smaller surface area and larger particle size of DE compared to the primary size of the silica particles.

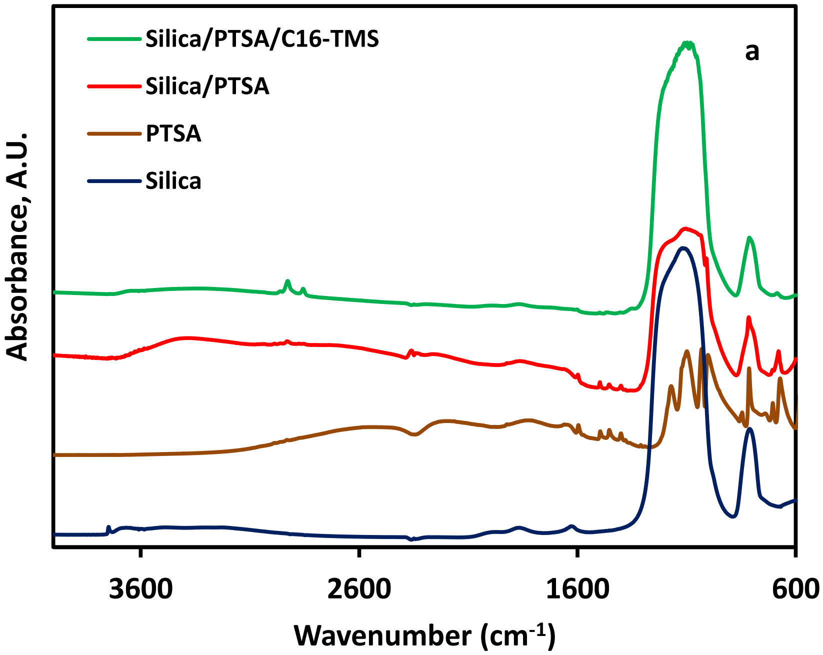

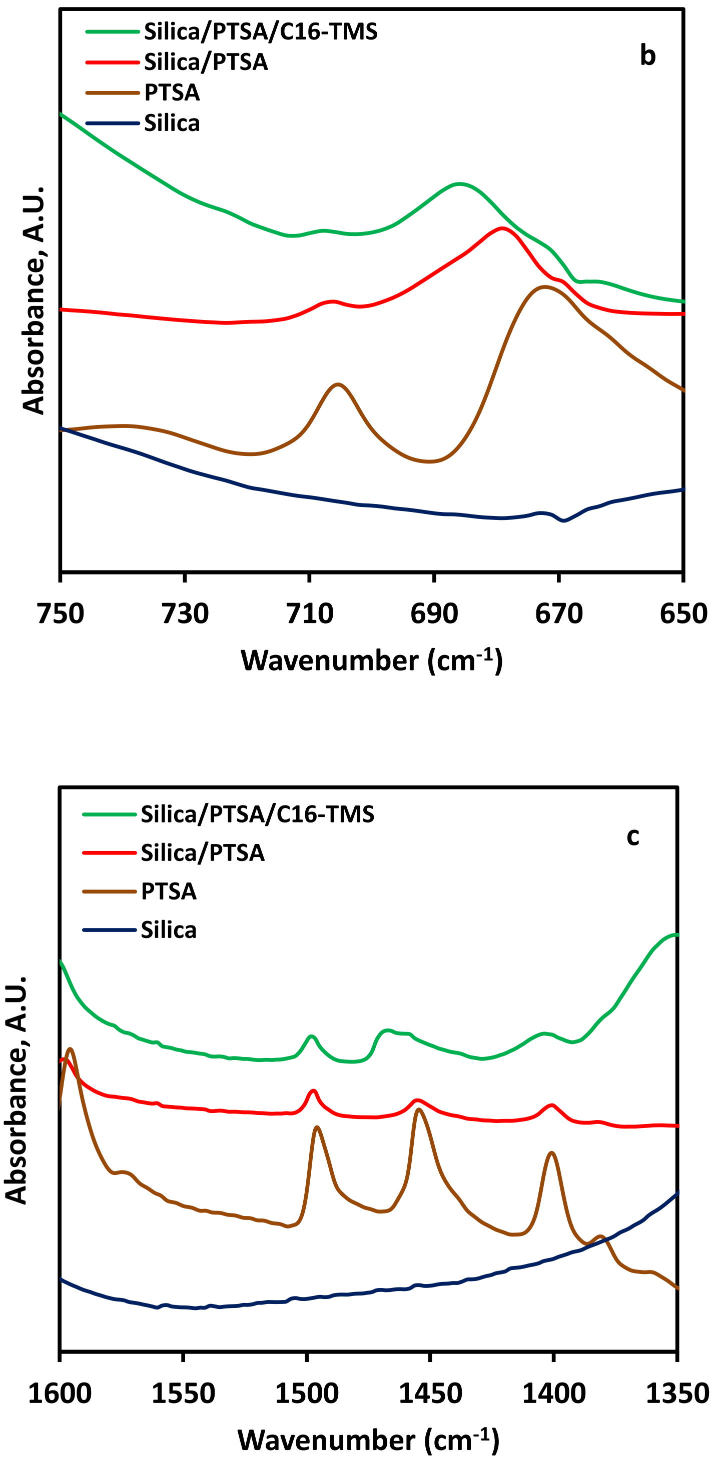

Figure 7.3. FTIR spectra of a) silica, silica with 1.5 mg/m^2 PTSA, 0.2 mg/m^2 C16-TMS adsorbed hydrocarbon amount on silica with 0.27 mg/m^2 PTSA and neat PTSA, b) aromatic C-H bending region: 750 - 600 cm^{-1}, and c) sulfonate group related strong peaks

in 1600 - 1350 cm^{-1} frequencies. The spectra are in the order shown in the legends and the intensities were adjusted for comparison of the peak shapes/positions.

The amount of PTSA bound was measured on the surface of silica and DE as a function of the total amount of PTSA added from solution in toluene. The bound PTSA was estimated from the original mass of the sample from the TGA analysis and the mass loss between 250-700 °C (vida infra). The mass of the silica was the remaining mass at the highest temperature. Figures 7.4 and 7.5 show the adsorption isotherm-like curves from the TGA data for PTSA adsorbed onto silica and DE. The curve of silica with PTSA was roughly the shape of a Langmuir isotherm.

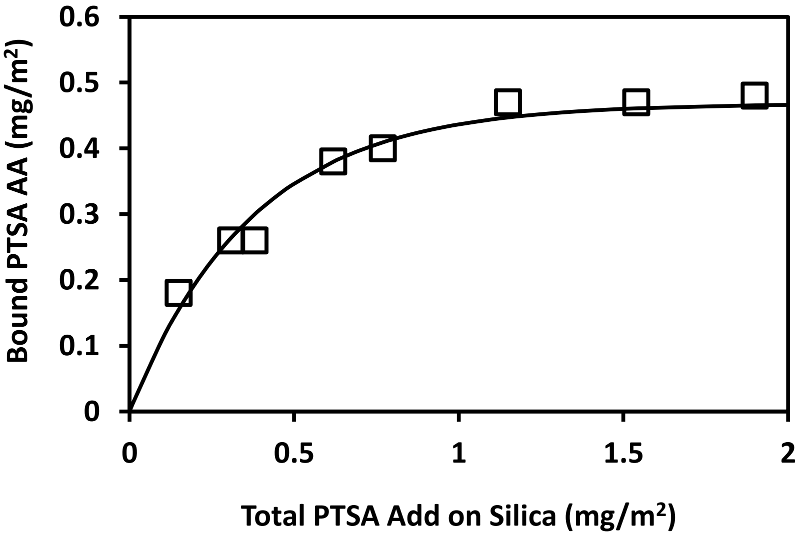

Figure 7.4. Bound PTSA adsorbed amount on silica from toluene as a function of total amount added per surface area.

The adsorbed amounts increased with amounts of PTSA added, reached a maximum value, and remained constant with increased PTSA added. The plateau region value revealed that the maximum adsorbed bound amount was approximately 0.47 mg/m^2 for adsorption of PTSA on silica. In contrast, PTSA adsorption on DE showed a linear relationship with the total added amounts. For the amounts we studied, we did not see the formation of a plateau region as seen with the silica.

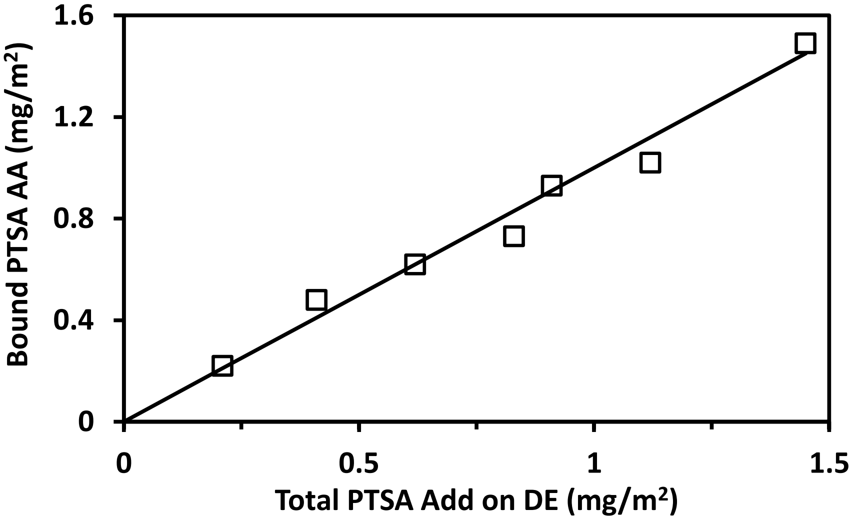

Figure 7.5. Bound PTSA adsorbed amount on DE from toluene as a function of total amount added per surface area.

Since the C16-TMS is not particularly volatile, the amounts of C16-TMS added to each of the surfaces from the initial solutions allowed us to estimate the *adsorbed hydrocarbon amounts* ($AA_{\text{HC-C16}}$) using Equation 7.1,

$$AA_{HC-C16} = \frac{[\frac{m_{C16-TMS}}{MW_{C16-TMS}}]\times MW_{HC-C16}}{S\times m} \tag{7.1}$$

where $AA_{\text{HC-C16}}$ is adsorbed hydrocarbon amount (mg/m^2) from the initial composition, $MW_{\text{C16-TMS}}$ is the molecular mass of C16-TMS silane (g/mol), $MW_{\text{HC-C16}}$ is the molecular mass of the hydrocarbon chain portion of C16-TMS silane (g/mol), *S* is the specific surface area of silica (130 m^2/g) or DE (24 m^2/g), *m* is mass of silica or DE (g), and $m_{\text{C16-}}$

$_{\mathrm{TMS}}$ is the amount of C16-TMS silane (g). Note that the adsorbed amounts are converted to mg/m^2.

For our experiments, both the C16-TMS and PTSA adsorb, but not all of the PTSA is directly bound. In the thermograms, non-adsorbed PTSA and water leave the sample at temperatures below 250 °C what remains is bound C16-TMS, bound PTSA and silica. Therefore, it is possible to estimate the total amounts of adsorbed, AA_{total} (C16TMS + PTSA) as the mass of total adsorbate per surface area of silica or

$$AA_{Total} = \frac{m_{Ad-C16-TMS} + m_{Ad-PTSA}}{m_{silica} \times S} \qquad (7.2)$$

or

$$AA_{Total} = \frac{f_{250-700}}{1-f_{20-700} \times S} \qquad (7.3)$$

where AA_{Total} is the adsorbed amount of C16-TMS plus PTSA (mg/m^2), $m_{\mathrm{Ad\text{-}C16\text{-}TMS}}$ is mass of adsorbed C16-TMS, $m_{\mathrm{Ad\text{-}PTSA}}$ is the mass of PTSA adsorbed, $f_{250\text{-}700}$ fraction of adsorbed C16-TMS and PTSA which came off/decomposed in the 250-700 °C region, $f_{20\text{-}700}$ fraction of total mass loss from 20-700 °C for silica, and S is specific surface area of silica (130 m^2/g). The values for DE can also be determined from Equation 7.3 with m_{silica} replaced by m_{DE} and S for DE being 24 m^2/g. So, the total amounts of C16-TMS and PTSA bound is given by the total mass losses ($f_{20\text{-}900}$) and bound mass losses ($f_{250\text{-}900}$) for the C16-TMS and PTSA remaining.

The total adsorbed amounts of bound C16-TMS and PTSA were larger than the amounts expected based on the C16-TMS amounts added alone. These differences were attributed to the amount of adsorbed PTSA because the samples were not washed after treatment. Both the C16-TMS silane coupling agent and PTSA are nonvolatile and have high boiling points (the boiling point of C16-TMS is 155 °C and PTSA is 140 °C). Therefore, the difference between the total adsorbed amount (AA_{Total}) and estimated ($AA_{\mathrm{HC\text{-}C16}}$) adsorbed hydrocarbon amount should be due to the adsorbed PTSA for any given sample as equation 7.4,

$$AA_{PTSA} = AA_{Total} - AA_{HC-C16} \tag{7.4}$$

With increasing the $AA_{\mathrm{HC\text{-}C16}}$ on the surface, the AA_{PTSA} decreased. If the surface area is fixed and added C16-TMS and PTSA take up constant (but not equal) surface areas, a linear relationship would be expected:

$$AA_{PTSA}^{0} = r \times AA_{HC-C16} + AA_{PTSA} \tag{7.5}$$

or, rearranging

$$AA_{PTSA} = AA_{PTSA}^{0} - r \times AA_{HC-C16} \tag{7.5a}$$

where AA^{0}_{PTSA} is the full surface coverage bound amount of PTSA (mg/m^2), AA_{PTSA} and $AA_{\mathrm{HC\text{-}C16}}$ the adsorbed amounts of bound PTSA and C16-TMS, and *r* is ratio of the surface size of the C16-TMS to PTSA, normalized on a mass basis (g PTSA/g C16-TMS). From equation 7.5a, we expect AA_{PTSA} to be a linear function of $AA_{\mathrm{HC\text{-}C16}}$, with an intercept of AA^{o}_{PTSA} and a slope of -*r*. The correlation between AA_{PTSA} and $AA_{\mathrm{HC\text{-}C16}}$, for the two different surfaces is shown in Figure 6. With the help of this correlation, we were able to quantify the adsorbed hydrocarbon amount of C16-TMS on the silica and DE surface. The basis for this estimation is the assumption that we have an independent estimate of the $AA_{\mathrm{HC\text{-}C16}}$ which we take as that amount added to the treating solution per surface area of substrate.

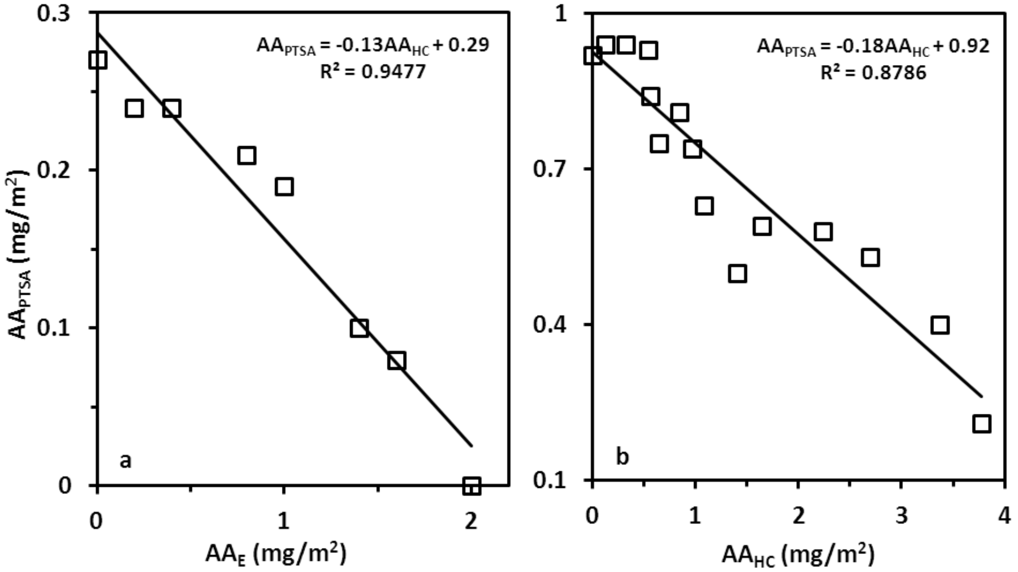

Figure 7.6. The adsorbed amount of PTSA (AA_{PTSA}) as a function of the hydrocarbon amount of C16-TMS **(**$AA_{HC\text{-}C16}$, estimated from the original solution composition) for a) silica b) DE surface.

Using the linear regressions from the Figure 6 graphs, we were able to estimate the calculated bound AA'_{PTSA} at any $AA_{HC\text{-}C16}$ initial composition. In addition, these values were used to calculate the adsorbed hydrocarbon amounts of C16-TMS ($AA_{C16\text{-}TMS}$). The intercept of each line indicated the AA^0_{PTSA} on the surface of silica and DE, as shown in Figure 6. Moreover, the intercepts were close amounts of PTSA bound for the samples with only PTSA added. The corrected value of $AA_{C16\text{-}TMS}$ can then be calculated from the value from the linear regression or

$$AA_{C16-TMS} = AA_{Total} - AA'_{PTSA} \tag{7.6}$$

The results for the corrected values of $AA_{C16\text{-}TMS}$, which was our original goal, are summarized in Table 7.1 and 7.2 for silica and DE, respectively.

Table 7.1. Adsorbed hydrocarbon amounts of C16-TMS on silica ($AA'_{\text{C16-TMS}}$) after correction.

$AA_{\text{HC-C16}}$ (mg/m^2)	AA_{Total} (mg/m^2)	AA_{PTSA} (mg/m^2)	AA'_{PTSA} (mg/m^2)* = -0.13AA_{HC} +0.29	$AA_{\text{C16-TMS}}$ (mg/m^2)
0	0.27	0.27	0.29	
0.2	0.44	0.24	0.26	0.18
0.4	0.64	0.24	0.24	0.40
0.8	1.01	0.21	0.18	0.83
1.00	1.19	0.19	0.16	1.03
1.40	1.5	0.1	0.10	1.40
1.60	1.68	0.08	0.08	1.60
2.00	2.00	0	0.03	1.97

* Corrected value of AA_{PTSA} from the linear regression.

Table 7.2. Adsorbed hydrocarbon amount of C16-TMS on DE ($AA'_{\text{C16-TMS}}$) after correction.

$AA_{\text{HC-C16}}$ (mg/m^2)	AA_{Total} (mg/m^2)	AA_{PTSA} (mg/m^2)	AA'_{PTSA} (mg/m^2)* = -0.18AA_{HC} +0.92	$AA_{\text{C16-TMS}}$ (mg/m^2)
0	0.92	0.92	0.92	
0.13	1.07	0.94	0.90	0.17
0.32	1.26	0.94	0.87	0.39
0.54	1.47	0.93	0.83	0.64
0.56	1.4	0.84	0.83	0.57

0.65	1.4	0.75	0.81	0.59
0.84	1.65	0.81	0.78	0.87
0.97	1.71	0.74	0.75	0.96
1.08	1.71	0.63	0.73	0.98
1.4	1.9	0.5	0.68	1.22
1.64	2.23	0.59	0.64	1.59
2.24	2.82	0.58	0.53	2.29
2.69	3.22	0.53	0.45	2.77
3.37	3.77	0.4	0.33	3.44
3.77	3.98	0.21	0.26	3.74
4.31	4.29	-0.02	0.16	4.13

* Corrected value of AA_{PTSA} from the linear regression.

To get a better idea of how close the $\text{AA}_{\text{C16-TMSr}}$ with $AA_{\text{HC-C16}}$, Figure 7.7 is plotted with the initial and adsorbed C16-TMS adsorbed amount values. The dashed line indicated that if the reaction was perfect, the $AA_{\text{HC-C16}}$ should be equal to the $AA_{\text{C16-TMS}}$. Figure 7.7 clearly indicated that with correction $AA_{\text{C16-TMS}}$ became almost equal to the $AA_{\text{HC-C16}}$.

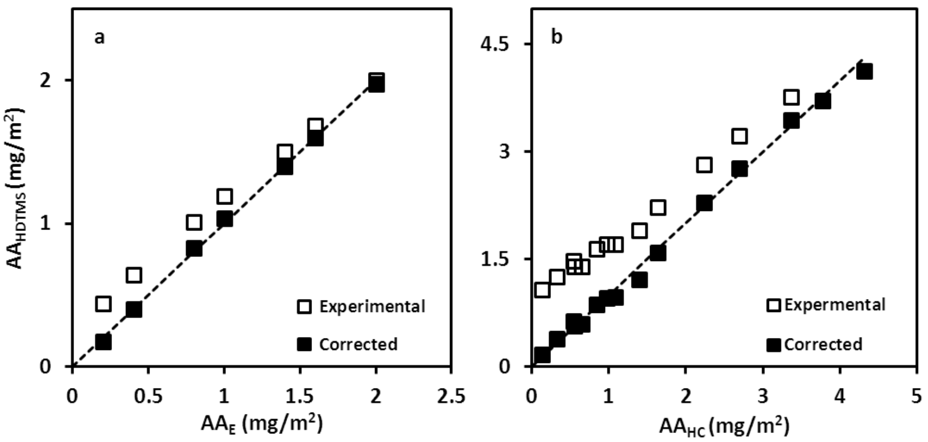

Figure 7.7. Comparison of C16-TMS adsorbed hydrocarbon amounts with $AA_{\text{HC-C16}}$, experimentally and after correction from the model on a) silica and b) DE.

7.5. DISCUSSION

The TGA mass loss can be used as a technique for quantitative and sometimes qualitative identification of organic matter on a surface. Bare silica did not show any mass loss throughout the temperature range, but silica with PTSA showed one main decomposition step in the TGA as shown in Figure 7.1(b). This main mass loss was related to the decomposition of organic material of PTSA. Bare DE and DE with PTSA showed two mass loss steps in Figure 7.1(c) and (d). The first mass loss was centered around 160 °C, and was mainly due to the loss of physically adsorbed water.[11,17] The second mass loss was attributed to the broad temperature range, which was around 2.4% and 4.4% on bare DE and DE with PTSA, respectively. The 2.4% mass loss attributed to the dehydroxylation of DE silanol groups was due to the condensation[18,19] and mass loss was consistent with the results of others.[20] The 4.4% mass loss was associated with the dehydroxylation of DE silanol groups and the decomposition of PTSA hydrocarbons. Accordingly, this 2% extra mass loss should be related to the PTSA. Mass loss due to the

PTSA correlated with the amount of PTSA used during the reaction (around 2%). This confirms that the mass loss is likely due to PTSA. Upon adsorbing the C16-TMS onto surface of silica and DE, the TGA showed a broad mass loss from 250 – 700 °C and 250 -900 °C. Based on the literature, the decomposition of adsorbed organic silanes takes place between 250 and 600 °C. This degradation step can be assigned to the decomposition of the hydrocarbon chains of C16-TMS.[17] Comparing the derivative curves of C16-TMS treated silica and DE with PTSA adsorbed silica and DE showed overlapping mass loss steps. Therefore, we were unable to directly quantify the amount of C16-TMS on the surface.

FTIR peaks confirmed that the adsorption of PTSA takes place in the sample of silica and DE. As Figure 7.3(b) and (c) showed, we were able to see aromatic C-H bending and some strong peaks related to the PTSA with silica and DE with PTSA and C16-TMS treated silica and DE. These stretching and bending frequencies were due to the PTSA, because C16-TMS does not have any aromatic and sulfonate moieties.

The adsorption isotherm like curves probes the surface coverage with PTSA. The PTSA adsorbed amounts on the surface depended on the nature of the surface and interactions between PTSA and the surface. Silica and DE are hydrophilic surfaces due the presence of silanol groups. In addition, PTSA is composed of hydrophilic sulfonate groups. These PTSA sulfonate groups are able to form hydrogen bonds with the silanol groups of silica and DE. The amount of adsorbed PTSA per unit surface area increased with the total add amount of the PTSA as shown in Figures 7.4 and 7.5. Similar to the other systems,[21] the adsorbed amounts of PTSA were expected to increase with increased total added PTSA amounts, reached a maximum value as shown in Figure 4 for silica and

PTSA system. According to literature, area per benzene molecule is around 40 Å.[22] Based on this number PTSA molecules that can occupy a 1 nm^2 surface of silica will be around 2.5. The curves of adsorption isotherm of PTSA and silica showed a maximum adsorption 0.47 mg/m^2. When the surface is covered with around 2 $molecules/nm^2$. These numbers indicate that PTSA formed a monolayer on the surface of silica. However, with the PTSA and DE system, we were unable see a plateau region and the adsorbed PTSA amount continuously increased with increasing total adsorbed amounts of PTSA. Further studies are needed to identify the factors affecting the interaction of PTSA with DE.

According to Figure 7.6, AA_{PTSA} decreased with the increase of the $AA_{\mathrm{HC\text{-}C16}}$ of C16-TMS. With an increase in the $AA_{\mathrm{HC\text{-}C16}}$, the amounts of AA_{PTSA} started to decrease, indicating that fewer PTSA molecules bind onto the surface. While the solution mixture was without C16-TMS, most of the PTSA sulfonate groups were able to form hydrogen bonds between the silanol groups of silica and DE. With the addition of C16-TMS and PTSA together onto the surfaces, the C16-TMS molecules formed covalent bonds while the PTSA molecules formed hydrogen bonds with silanol groups. Further addition of C16-TMS molecules with a constant amount of PTSA showed that the C16-TMS molecules have more affinity for the silanol groups than the PTSA. This leads to the formation of fewer bound PTSA molecules on the surface. Therefore, with increased adsorbed hydrocarbon amounts of C16-TMS, the number of bound PTSA molecules decreased. With this approach, we were able to determine the adsorbed C16-TMS amounts of each sample with high precision as shown in Figure 7.7. After the correction, $\mathrm{AA_{C16\text{-}TMS}}$ became almost equal to the $\mathrm{AA_{HC\text{-}C16}}$.

We also note that the values of the *r* (slope) parameter for both the silica and DE systems are similar (0.13 and 0.18, respectively). This implies that the addition of the same mass of silane coupling agent, takes up about 15% of the surface area of a PTSA molecule (on a per mass basis). The small differences between the two systems may be due to the different morphologies of the two substrates. In any case, the small values of *r* seem to be indicative of the behavior of added coupling agents. The formation of oligomers from the coupling agents in solution and on the surface means that not all of the silanes will be directly bound to the surface. Nevertheless the do seem to displace a small amount of PTSA per gram of silane added.

7.6. CONCLUSIONS

Silica and DE were modified by C16-TMS in the presence of PTSA as a catalyst. Due to the hydrophilic nature of silanol groups, PTSA molecules were adsorbed on the surfaces of silica and DE through hydrogen bonding. This made it difficult to calculate the C16-TMS adsorbed hydrocarbon amounts on the surfaces. With the help of total and estimated adsorbed hydrocarbon amounts of the C16-TMS, the PTSA adsorbed amounts on the surfaces were calculated. With that, we were able measure a linear relationship between the adsorbed PTSA and estimated hydrocarbon amounts of C16-TMS. This linear regression helps on the determination of close to accurate PTSA adsorbed amounts. Using the PTSA adsorbed amounts, C16-TMS adsorbed amounts were calculated. Calculated C16-TMS values were similar to the estimated adsorbed hydrocarbon amount of C16-TMS. Therefore, this linear calculation method became an alternative method for calculating the adsorbed hydrocarbon amounts of alkyltrimethoxysilanes when the PTSA was used as a catalyst, was not washed off and adsorbed on the surface.

7.7. ACKNOWLEDGEMENTS

The authors acknowledge the financial support of the Dry Surface Coating Guthrie, OK and the Oklahoma State University.

7.8. REFERENCES

(1) Amati, D.; Kovats, E. S. *Langmuir* **1988**, *4*, 329.

(2) Fadeev, A. Y.; McCarthy, T. J. *J. Am. Chem. Soc.* **1999**, *121*, 12184.

(3) Law, Y. Y.; Feke, D. L.; Manas-Zloczower, I. *Rubber Chem. Technol.* **2014**, *87*, 443.

(4) Park, J.-W.; Park, Y. J.; Jun, C.-H. *Chem. Commun.* **2011**, *47*, 4860.

(5) Kulkarni, M. V.; Viswanath, A. K. *Eur. Polym. J.* **2004**, *40*, 379.

(6) D'ONOFRIO, F.; Scettri, A. *Synthesis* **1985**, 1159.

(7) Anuradha, V.; Srinivas, P. V.; Aparna, P.; Rao, J. M. *Tetrahedron Lett.* **2006**, *47*, 4933.

(8) García, N.; Benito, E.; Guzmán, J.; Tiemblo, P. *J. Am. Chem. Soc.* **2007**, *129*, 5052.

(9) Levy, D.; Zayat, M. *The Sol-Gel Handbook: Synthesis, Characterization and Applications, 3-Volume Set*; John Wiley & Sons, 2015.

(10) Ambrožič, G.; Djerdj, I.; Škapin, S. D.; Žigon, M.; Orel, Z. C. *CrystEngComm* **2010**, *12*, 1862.

(11) Yuan, P.; Liu, D.; Tan, D.-Y.; Liu, K.-K.; Yu, H.-G.; Zhong, Y.-H.; Yuan, A.-H.; Yu, W.-B.; He, H.-P. *Microporous Mesoporous Mater.* **2013**, *170*, 9.

(12) Yadav, G. D.; Murkute, A. D. *Adv. Synth. Catal.* **2004**, *346*, 389.

(13) Zhou, W.; Yoshino, M.; Kita, H.; Okamoto, K.-i. *Ind. Eng. Chem. Res.* **2001**, *40*, 4801.

(14) Margoshes, M.; Fassel, V. A. *Spectrochim. Acta* **1955**, *7*, 14.

(15) Socrates, G. *Infrared and Raman characteristic group frequencies: tables and charts*; John Wiley & Sons, 2004.

(16) Tipson, R. S. *J. Am. Chem. Soc.* **1952**, *74*, 1354.

(17) Parikh, A.; Schivley, M.; Koo, E.; Seshadri, K.; Aurentz, D.; Mueller, K.; Allara, D. *J. Am. Chem. Soc.* **1997**, *119*, 3135.

(18) Chaisena, A.; Rangsriwatananon, K. *Suranaree J. Sci Technol* **2004**, *11*, 289.

(19) Yuan, P.; Wu, D. Q.; He, H. P.; Lin, Z. Y. *Appl. Surf. Sci.* **2004**, *227*, 30.

(20) Yuan, P.; Liu, D.; Tan, D.-Y.; Liu, K.-K.; Yu, H.-G.; Zhong, Y.-H.; Yuan, A.-H.; Yu, W.-B.; He, H.-P. *Microporous and Mesoporous Materials* **2013**, *170*, 9.

(21) Blum, F. D.; Young, E. N.; Smith, G.; Sitton, O. C. *Langmuir* **2006**, *22*, 4741.

(22) Barrer, R.; MacLeod, D. *Trans. Faraday Soc.* **1955**, *51*, 1290.

7.9. SUPORTING INFORMATION

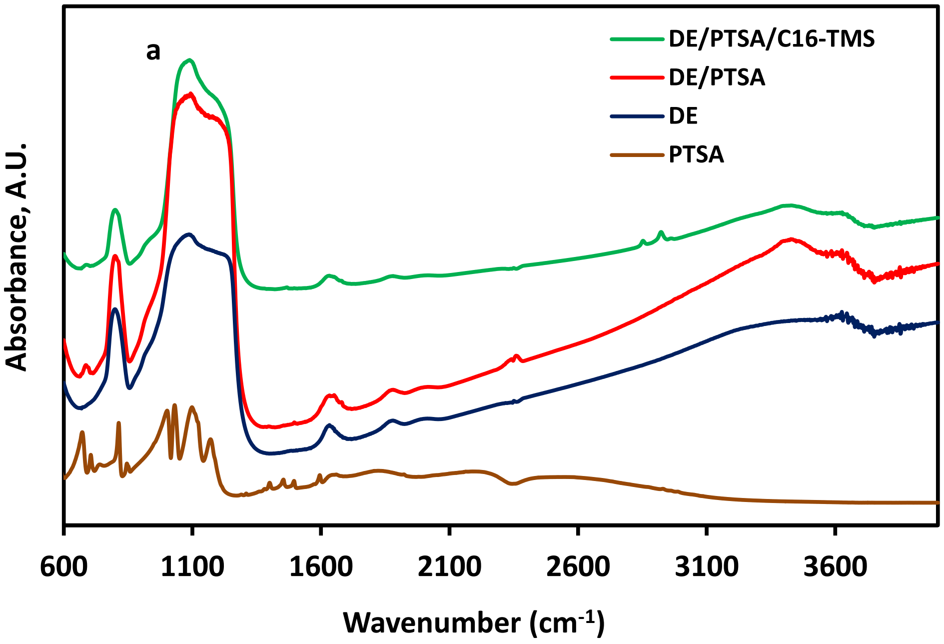

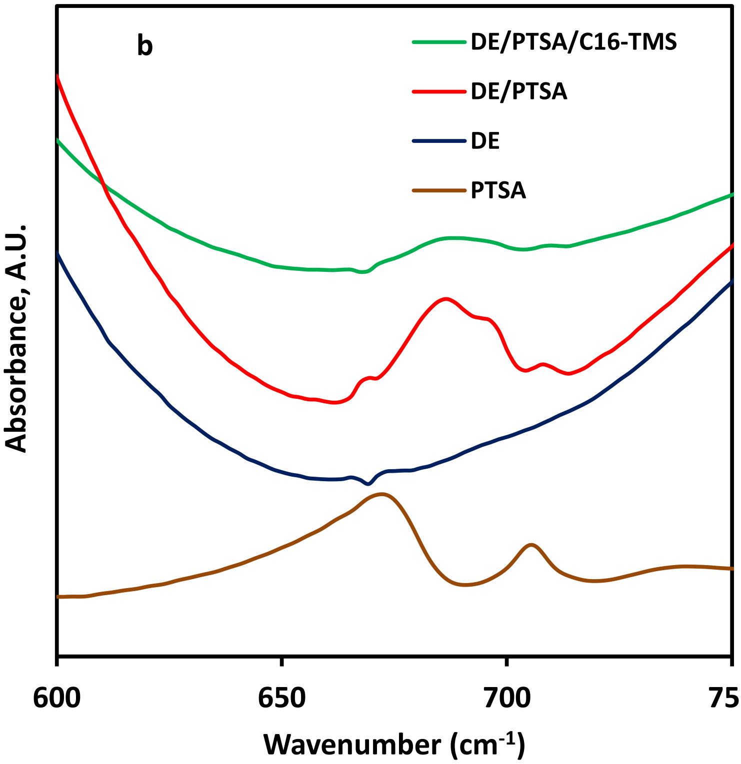

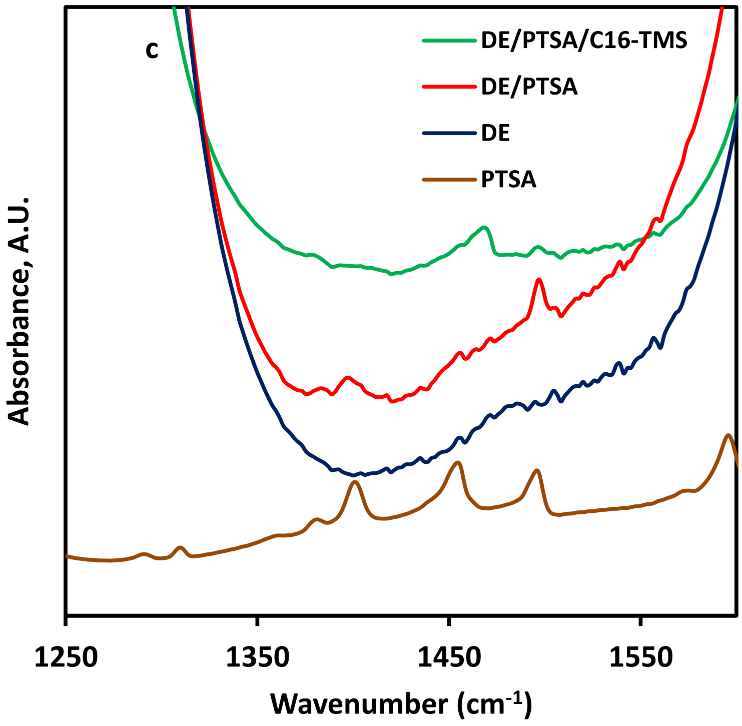

Figure S7.1. FTIR spectra of a) DE, DE with 1.5 mg/m^2 PTSA, and 0.54 mg/m^2 C16-TMS adsorbed hydrocarbon amount on silica with 0.92 mg/m^2 PTSA, b) aromatic C-H bending region: 750 - 600 cm^{-1}, and c) sulfonate group related strong peaks in 1600 - 1350 cm^{-1} frequencies.

APPENDICES

APPENDIX A

SEM IMAGES OF DIFFERENT CHAIN LENGTH ALKYLTRIMETHOXYSILANE

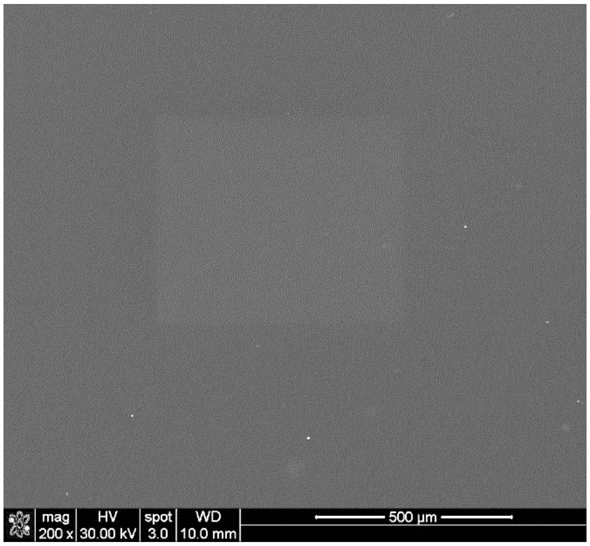

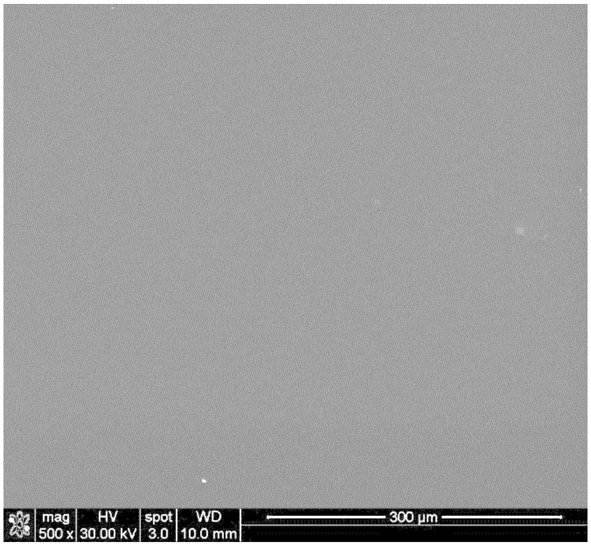

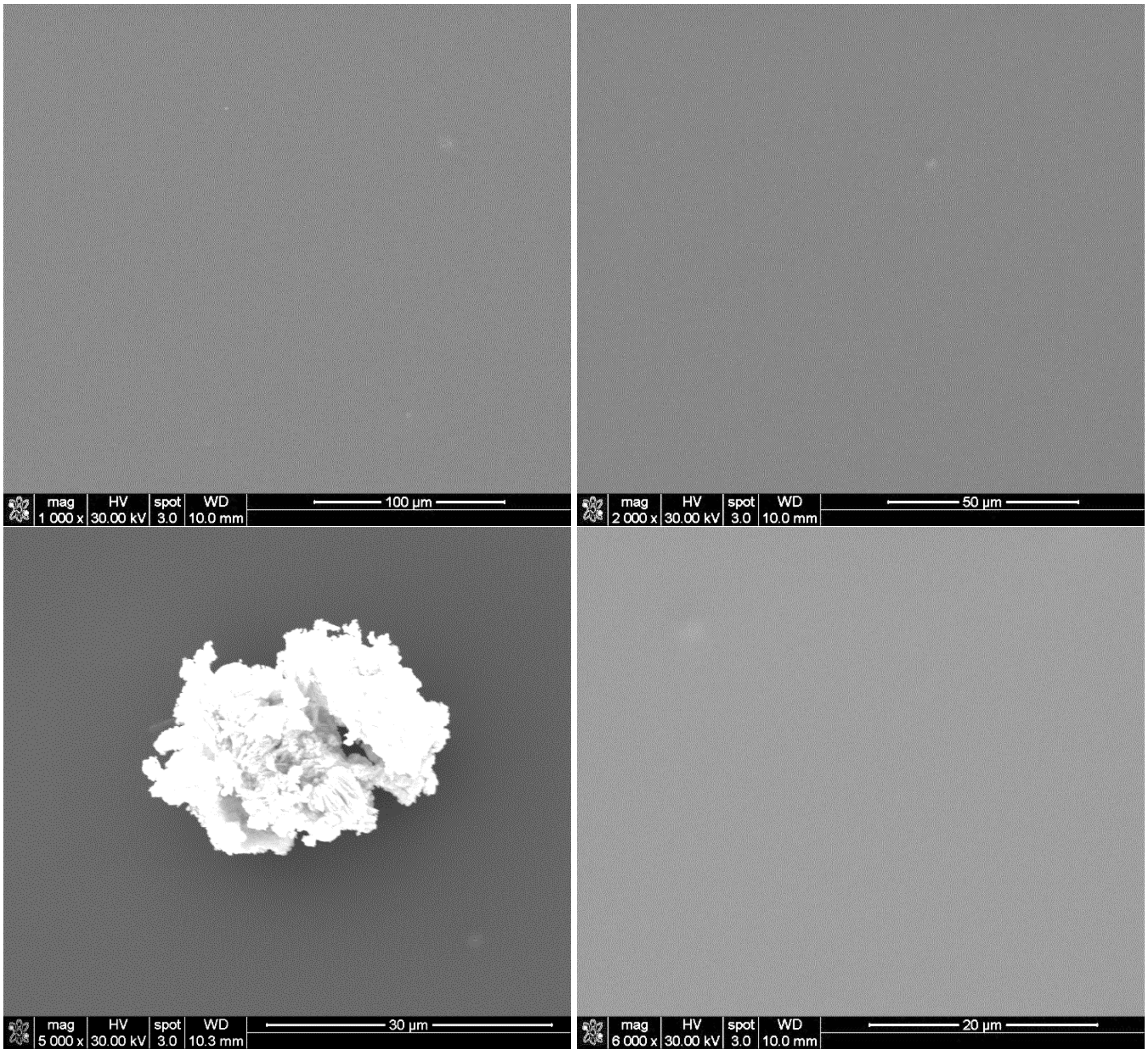

Figure A1. SEM images of polyurethane coatings without 3.4 mg/m^2 C12-TMS treated DE.

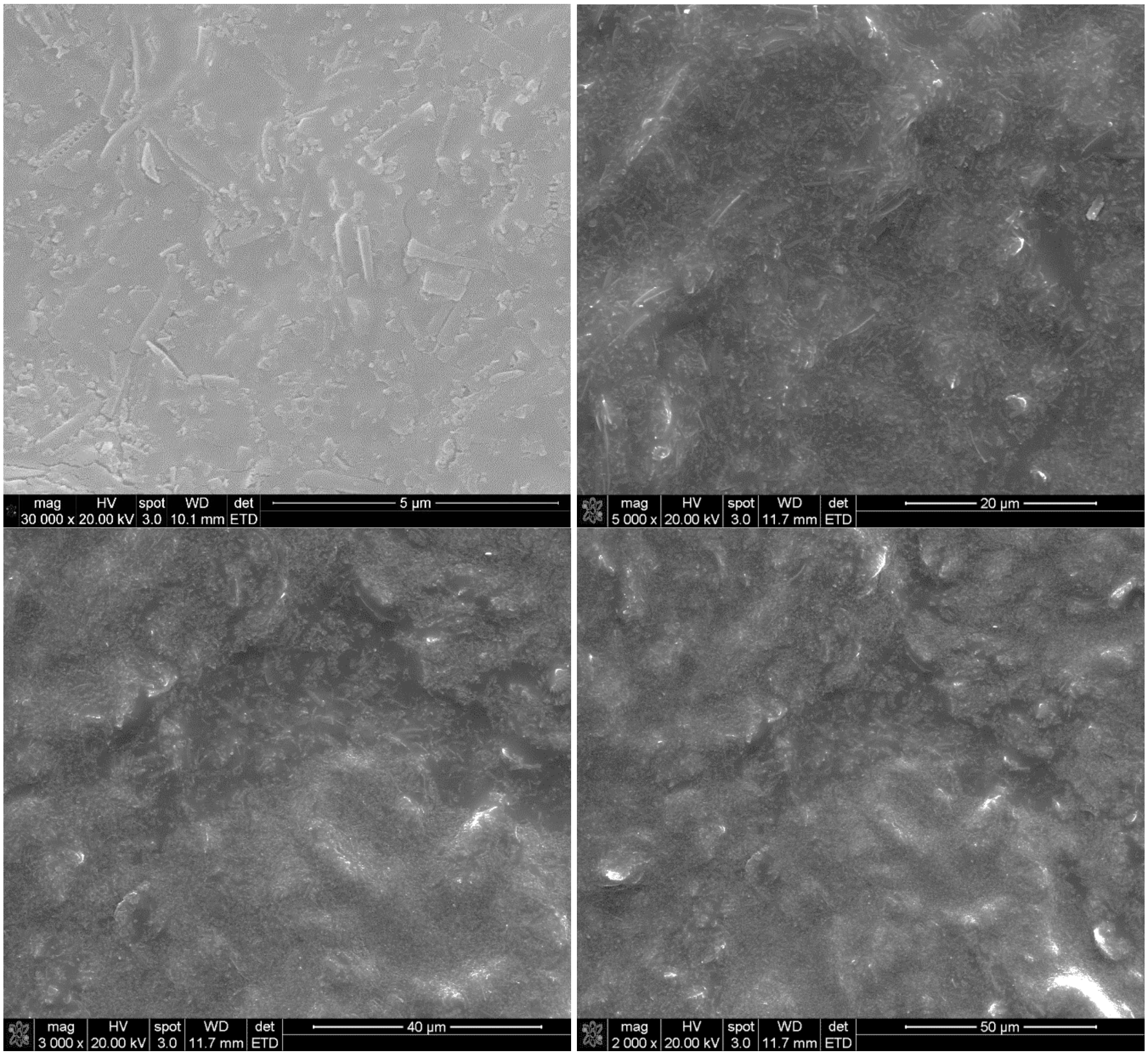

Figure A2. SEM images of polyurethane coatings with particle loadings of 3.4 mg/m^2 C12-TMS treated DE for 14.3%, -treated DE.

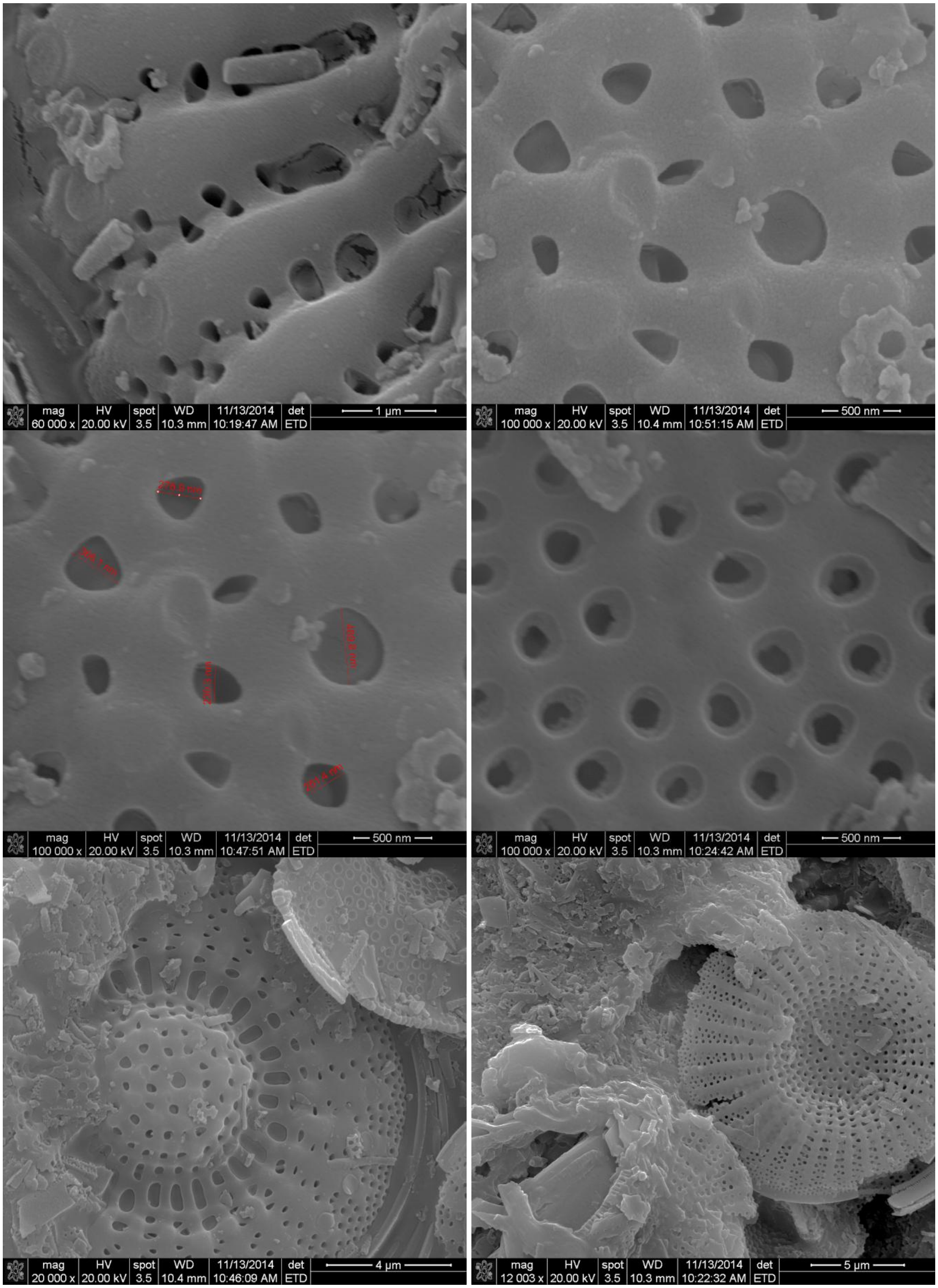
mag 60 000 x HV 20.00 kV spot 3.5 WD 10.3 mm 11/13/2014 10:19:47 AM det ETD 1 µm
mag 100 000 x HV 20.00 kV spot 3.5 WD 10.4 mm 11/13/2014 10:51:15 AM det ETD 500 nm
mag 100 000 x HV 20.00 kV spot 3.5 WD 10.3 mm 11/13/2014 10:47:51 AM det ETD 500 nm
mag 100 000 x HV 20.00 kV spot 3.5 WD 10.3 mm 11/13/2014 10:24:42 AM det ETD 500 nm
mag 20 000 x HV 20.00 kV spot 3.5 WD 10.4 mm 11/13/2014 10:46:09 AM det ETD 4 µm
mag 12 003 x HV 20.00 kV spot 3.5 WD 10.3 mm 11/13/2014 10:22:32 AM det ETD 5 µm

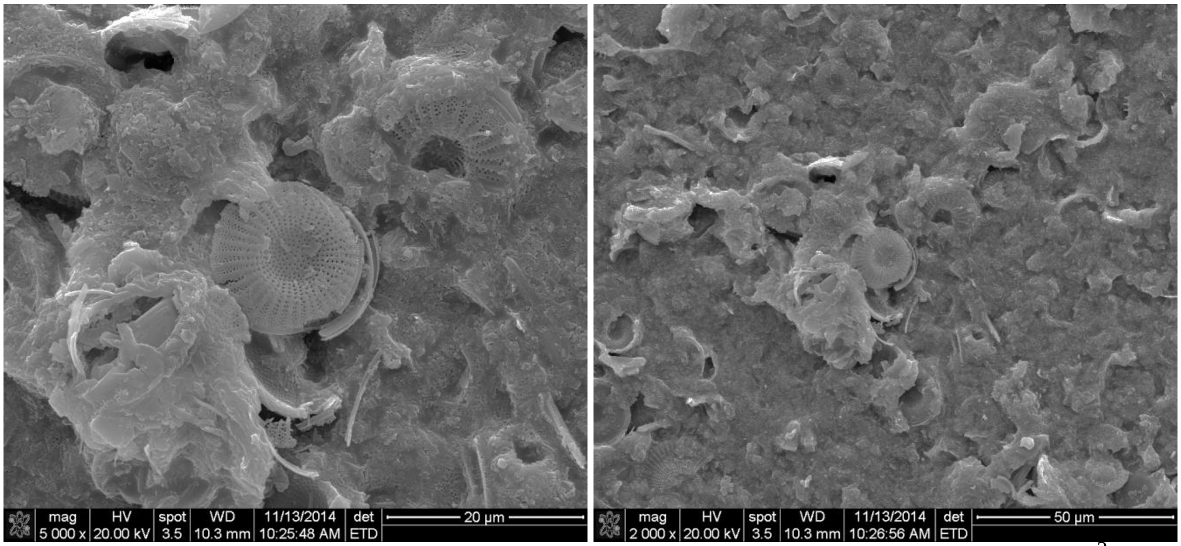

Figure A3. SEM images of polyurethane coatings with particle loadings of 3.4 mg/m^2

C12-TMS treated DE for 40%, -treated DE.

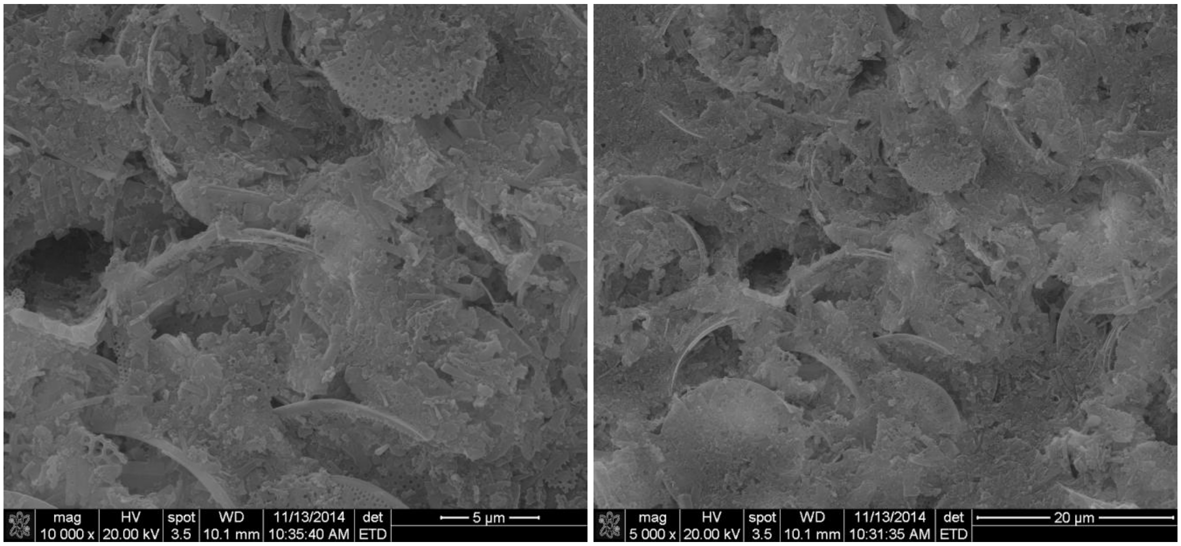

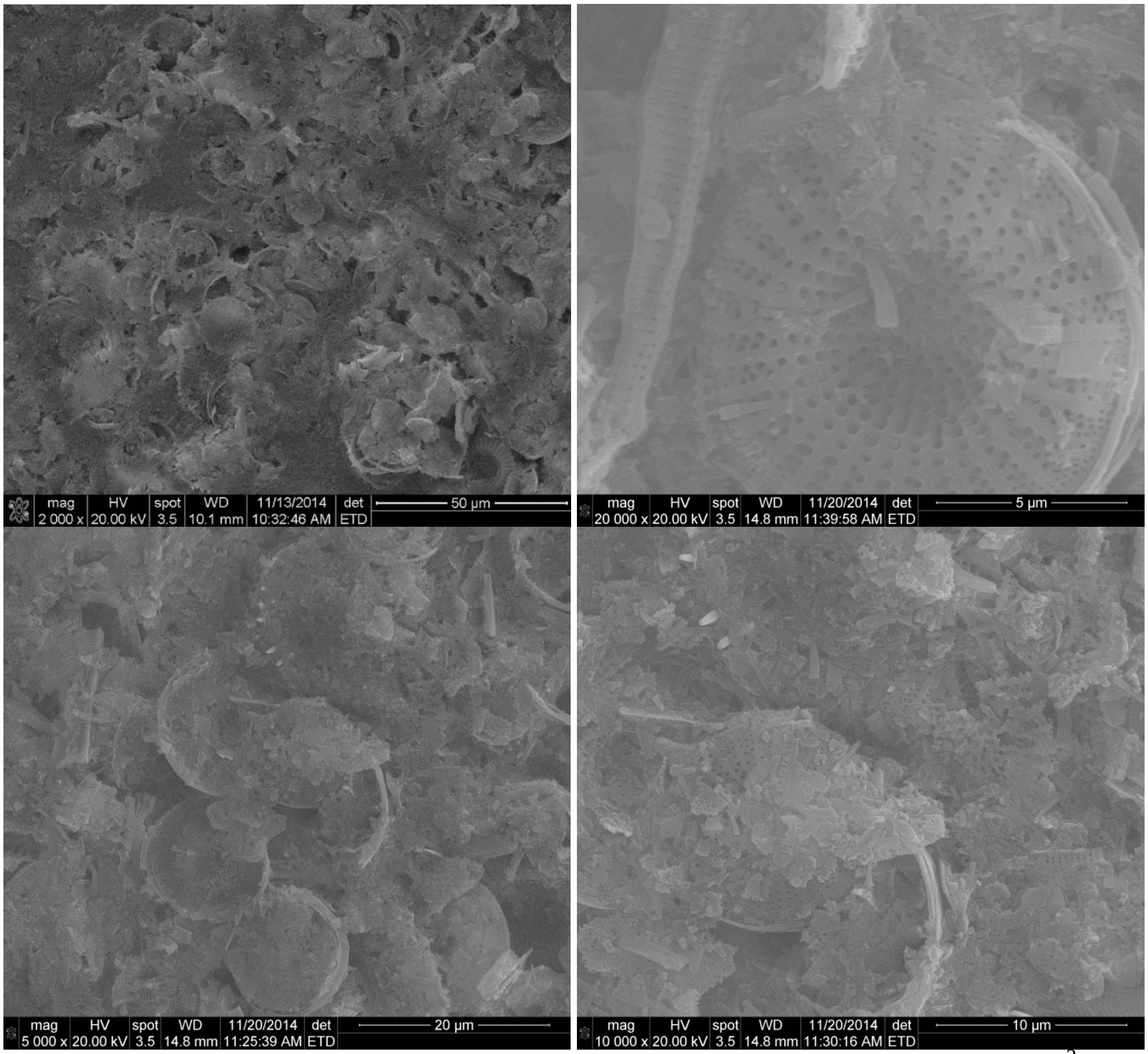

Figure A4. SEM images of polyurethane coatings with particle loadings of 3.4 mg/m^2

C12-TMS treated DE for 62.5%, -treated DE.

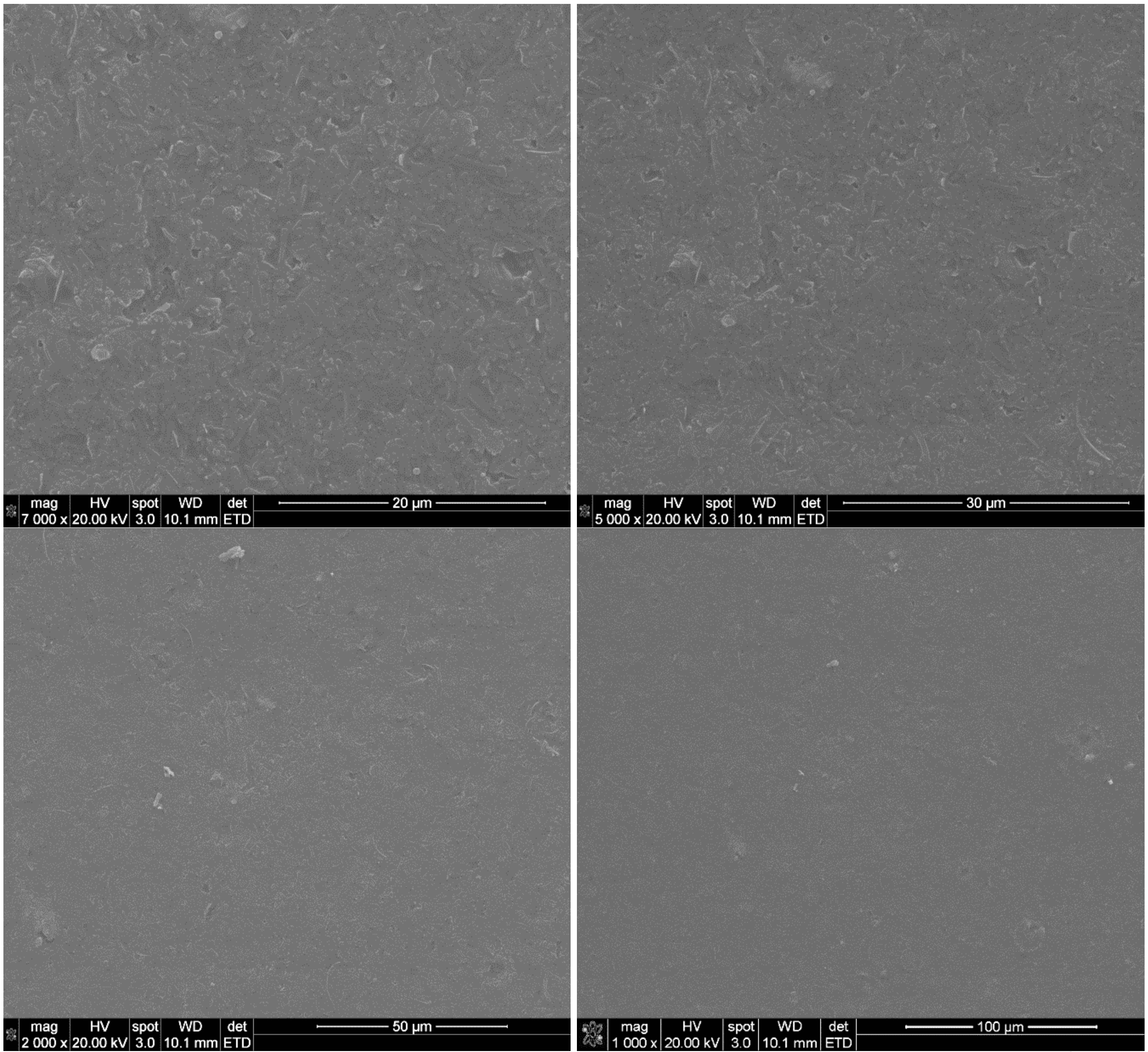

Figure A5. SEM images of polyurethane coatings with particle loadings of 2.2 mg/m^2

C3-TMS treated DE for 50%, -treated DE.

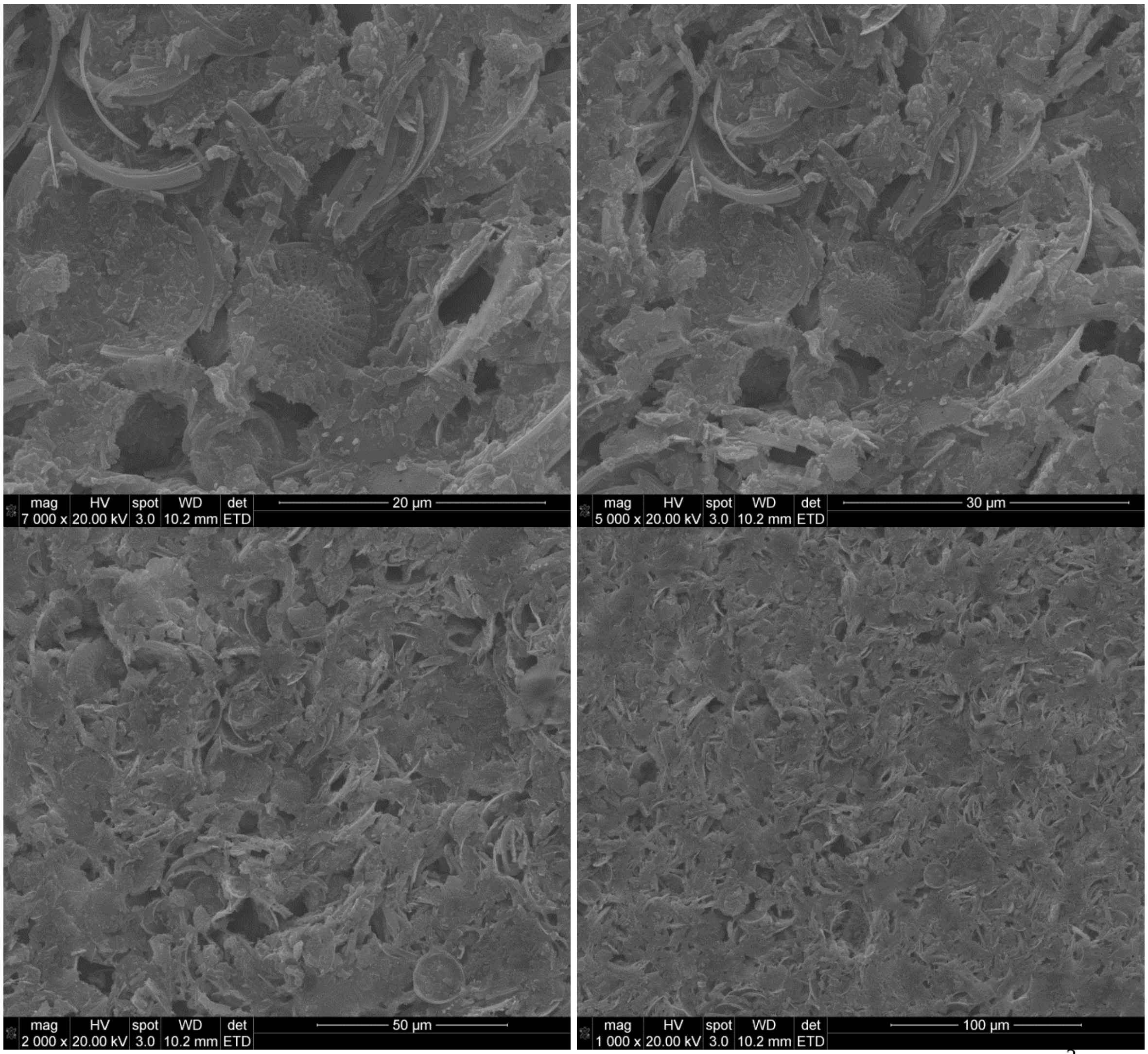

Figure A6. SEM images of polyurethane coatings with particle loadings of 2.2 mg/m^2 C8-TMS treated DE for 50%, -treated DE.

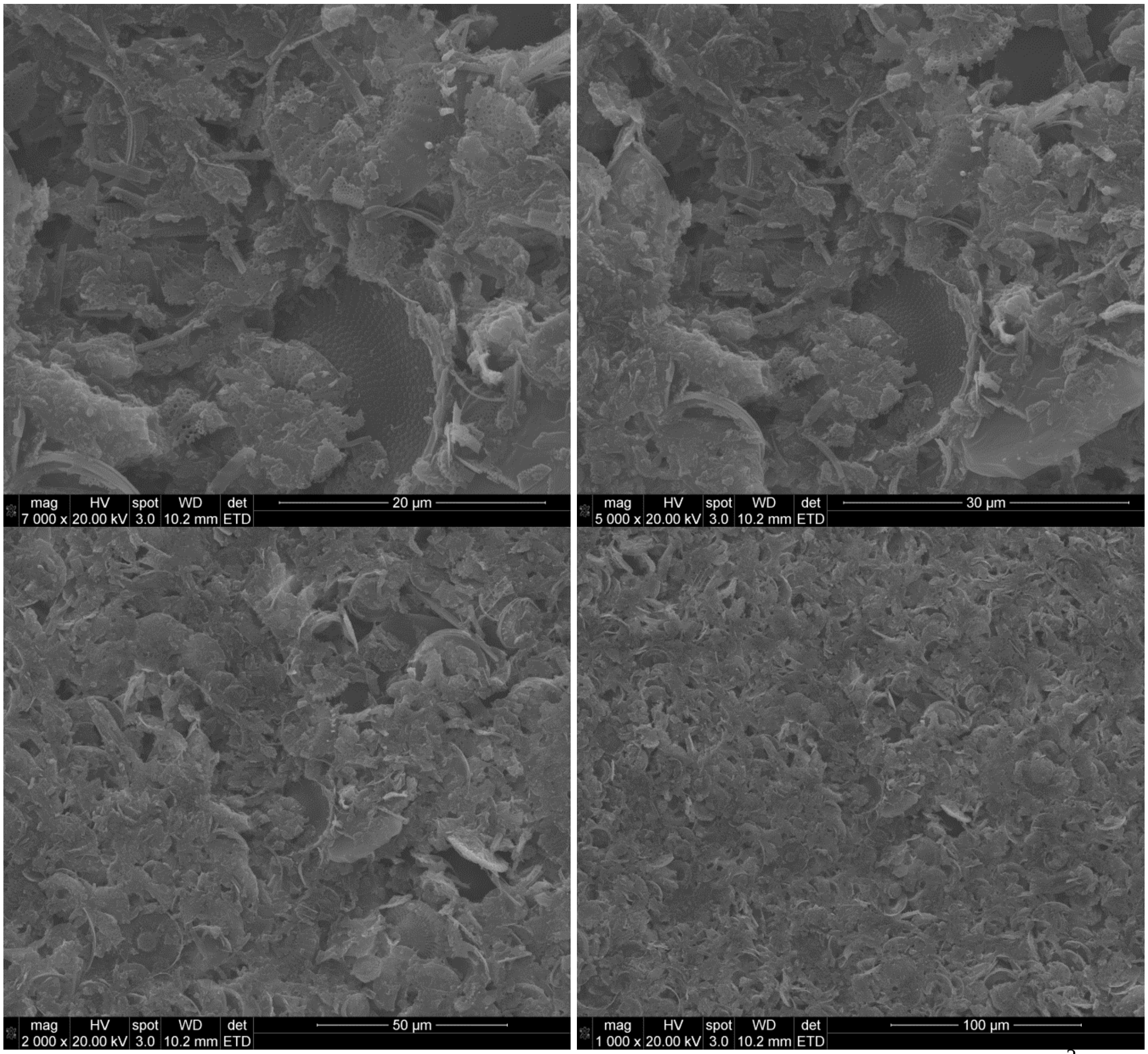

Figure A7. SEM images of polyurethane coatings with particle loadings of 2.2 mg/m^2

C12-TMS treated DE for 50%, -treated DE.

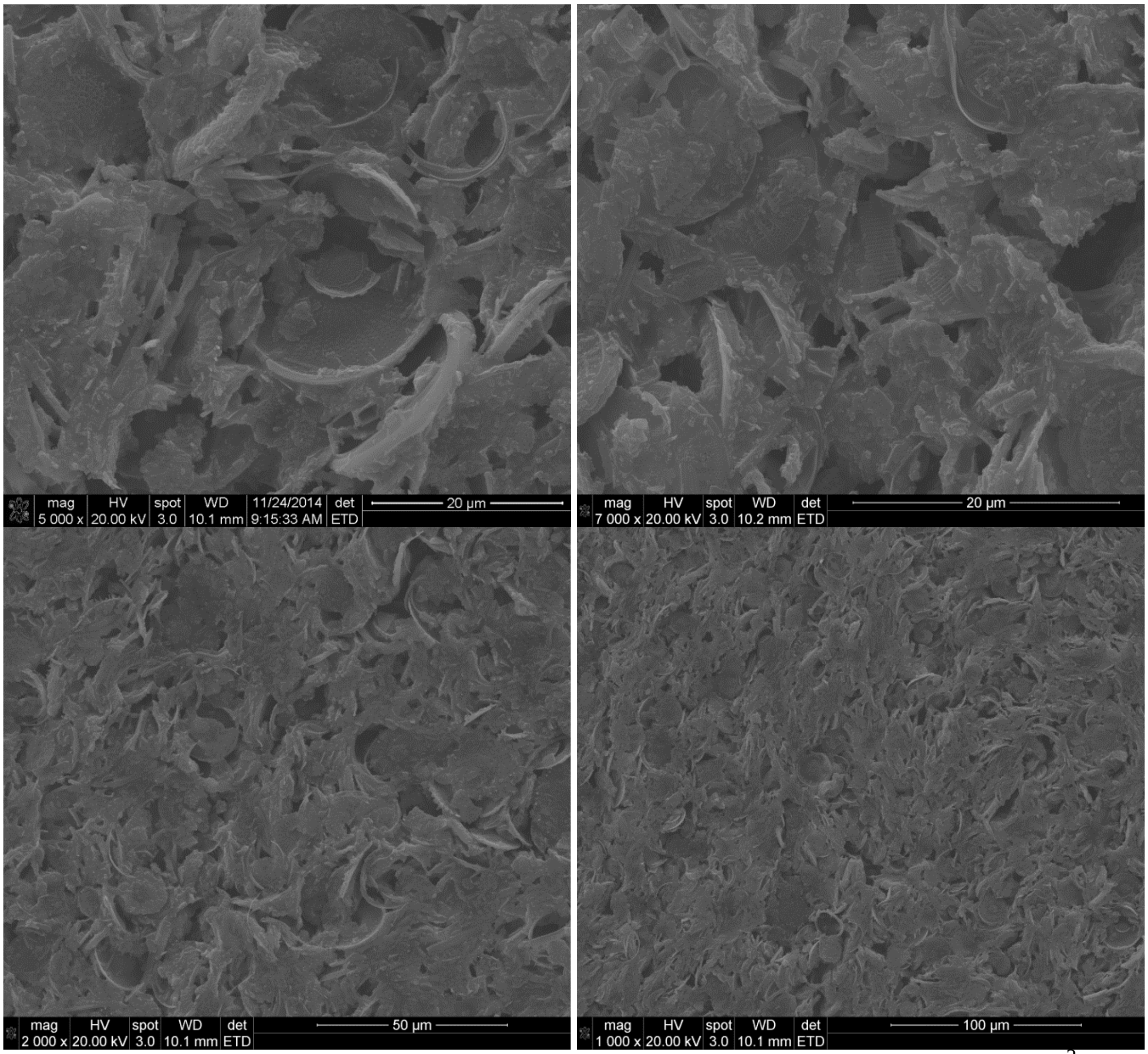

Figure A8. SEM images of polyurethane coatings with particle loadings of 2.2 mg/m^2 C16-TMS treated DE for 50%, -treated DE.

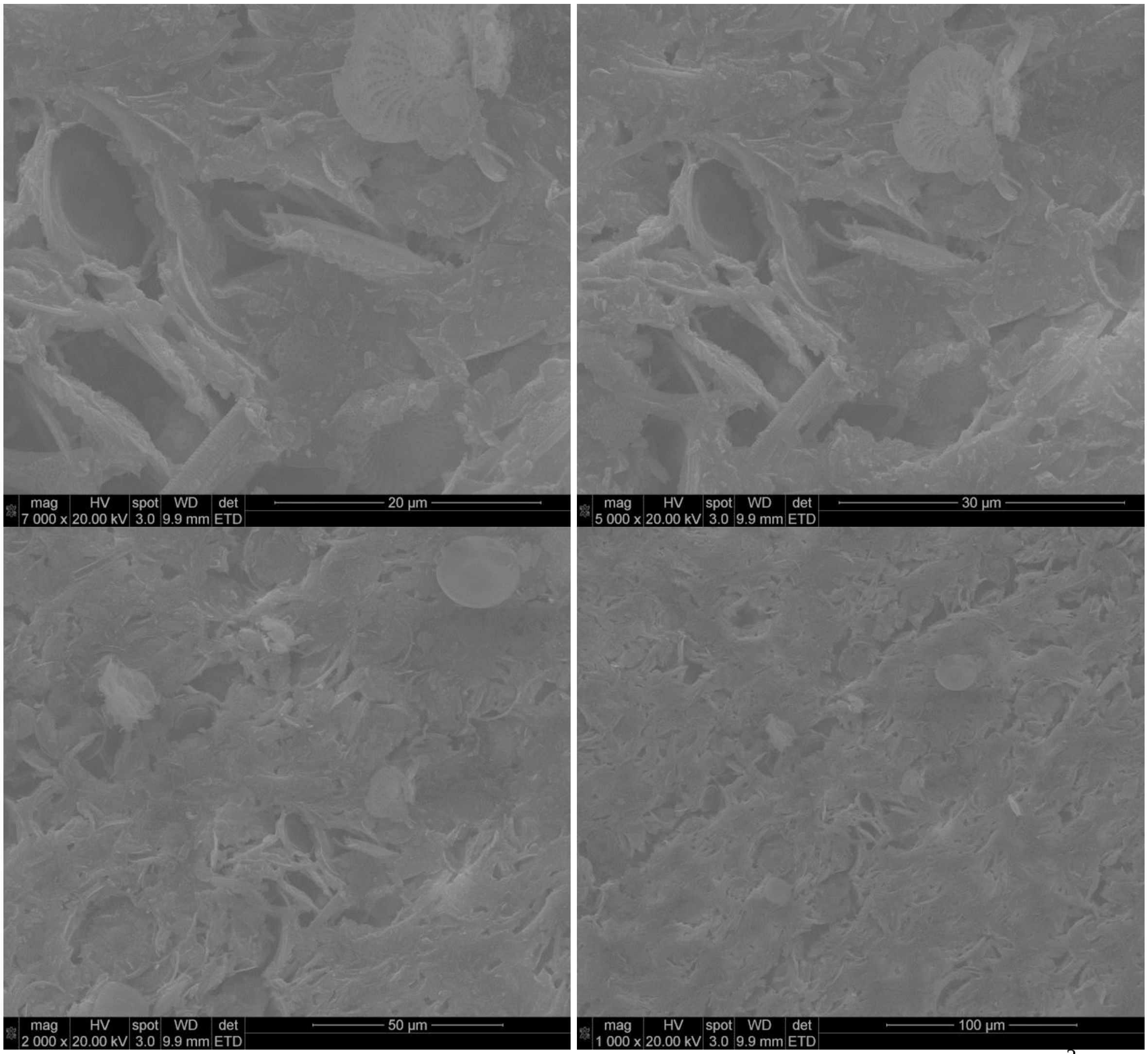

Figure A9. SEM images of polyurethane coatings with particle loadings of 2.2 mg/m^2

C18-TMS treated DE for 50%, -treated DE.

VITA

M. A. Helanka Jayani Perera

Candidate for the Degree of

Doctor of Philosophy

Thesis: SUPERHYROPHOBICITY AND STRUCTURES OF ADSORBED SILANE COUPLING AGENTS ON SILICA AND DIATOMACEOUS EARTH

Major Field: Polymer Chemistry

Biographical:

Education:

Completed the requirements for the Doctor of Philosophy in Polymer Chemistry at Oklahoma State University, Stillwater, Oklahoma in July, 2016.

Completed the requirements for the Bachelor of Science in Chemistry, University of Kelaniya, Sri Lanka, 2005.

Experience:

Teaching and research assistant, Department of Chemistry, Oklahoma State University, USA, 2011-2016.

Chemistry teacher, Rosary School, Sharjah, UAE, 2006-2009

Assistant lecturer, Department of Chemistry, University of Kelaniya, Sri Lanka, 2005

Professional Memberships:

American Chemical Society (Polymer division)
Golden Key International Honor Society